



MINISTÉRIO DA CIÊNCIA, TECNOLOGIA, INOVAÇÕES E COMUNICAÇÕES  
**INSTITUTO NACIONAL DE PESQUISAS ESPACIAIS**

sid.inpe.br/mtc-m21b/2017/07.03.18.29-TDI

**THUNDERSTORMS LIFE CYCLE OBSERVATION:  
SATELLITE MULTI-CHANNEL MODEL FOR  
WARNING SYSTEM**

Lina Esther Rivelli Zea

Master's Dissertation of the  
Graduate Course in Meteorology,  
guided by Dr. Luiz Augusto Toledo  
Machado, approved in August 03,  
2017.

URL of the original document:

<<http://urlib.net/8JMKD3MGP3W34P/3P7RM3E>>

INPE  
São José dos Campos  
2017

**PUBLISHED BY:**

Instituto Nacional de Pesquisas Espaciais - INPE

Gabinete do Diretor (GBDIR)

Serviço de Informação e Documentação (SESID)

Caixa Postal 515 - CEP 12.245-970

São José dos Campos - SP - Brasil

Tel.:(012) 3208-6923/6921

E-mail: pubtc@inpe.br

**COMMISSION OF BOARD OF PUBLISHING AND PRESERVATION  
OF INPE INTELLECTUAL PRODUCTION (DE/DIR-544):****Chairperson:**

Maria do Carmo de Andrade Nono - Conselho de Pós-Graduação (CPG)

**Members:**

Dr. Plínio Carlos Alvalá - Centro de Ciência do Sistema Terrestre (COCST)

Dr. André de Castro Milone - Coordenação-Geral de Ciências Espaciais e Atmosféricas (CGCEA)

Dra. Carina de Barros Melo - Coordenação de Laboratórios Associados (COCTE)

Dr. Evandro Marconi Rocco - Coordenação-Geral de Engenharia e Tecnologia Espacial (CGETE)

Dr. Hermann Johann Heinrich Kux - Coordenação-Geral de Observação da Terra (CGOBT)

Dr. Marley Cavalcante de Lima Moscati - Centro de Previsão de Tempo e Estudos Climáticos (CGCPT)

Silvia Castro Marcelino - Serviço de Informação e Documentação (SESID)

**DIGITAL LIBRARY:**

Dr. Gerald Jean Francis Banon

Clayton Martins Pereira - Serviço de Informação e Documentação (SESID)

**DOCUMENT REVIEW:**

Simone Angélica Del Duca Barbedo - Serviço de Informação e Documentação (SESID)

Yolanda Ribeiro da Silva Souza - Serviço de Informação e Documentação (SESID)

**ELECTRONIC EDITING:**

Marcelo de Castro Pazos - Serviço de Informação e Documentação (SESID)

André Luis Dias Fernandes - Serviço de Informação e Documentação (SESID)



MINISTÉRIO DA CIÊNCIA, TECNOLOGIA, INOVAÇÕES E COMUNICAÇÕES  
**INSTITUTO NACIONAL DE PESQUISAS ESPACIAIS**

sid.inpe.br/mtc-m21b/2017/07.03.18.29-TDI

**THUNDERSTORMS LIFE CYCLE OBSERVATION:  
SATELLITE MULTI-CHANNEL MODEL FOR  
WARNING SYSTEM**

Lina Esther Rivelli Zea

Master's Dissertation of the  
Graduate Course in Meteorology,  
guided by Dr. Luiz Augusto Toledo  
Machado, approved in August 03,  
2017.

URL of the original document:

<<http://urlib.net/8JMKD3MGP3W34P/3P7RM3E>>

INPE  
São José dos Campos  
2017

Cataloging in Publication Data

---

Rivelli Zea, Lina Esther.

R524t      Thunderstorms life cycle observation: satellite multi-channel  
model for warning system / Lina Esther Rivelli Zea. – São José  
dos Campos : INPE, 2017.

xxvi + 101 p. ; (sid.inpe.br/mtc-m21b/2017/07.03.18.29-TDI)

Dissertation (Master in Meteorology) – Instituto Nacional de  
Pesquisas Espaciais, São José dos Campos, 2017.

Guiding : Dr. Luiz Augusto Toledo Machado.

1. Nowcasting. 2. Thunderstorms. 3. Electrification. 4. Satellite  
multi-channel. 5. Subtropical region. I.Title.

CDU 551.594.21

---



Esta obra foi licenciada sob uma Licença [Creative Commons Atribuição-NãoComercial 3.0 Não Adaptada](https://creativecommons.org/licenses/by-nc/3.0/).

This work is licensed under a [Creative Commons Attribution-NonCommercial 3.0 Unported License](https://creativecommons.org/licenses/by-nc/3.0/).

Aluno (a): **Lina Esther Rivelli Zea**

Título: "THUNDERSTORMS LIFE CYCLE OBSERVATION: SATELLITE MULTI-CHANNEL MODEL FOR WARNING SYSTEM".

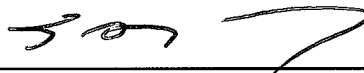
Aprovado (a) pela Banca Examinadora  
em cumprimento ao requisito exigido para  
obtenção do Título de **Mestre** em  
**Meteorologia**

Dr. José Antonio Aravéquia



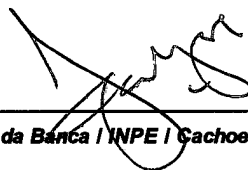
Presidente | INPE | Cachoeira Paulista - SP

Dr. Luiz Augusto Toledo Machado



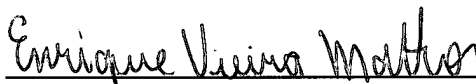
Orientador(a) | INPE | Cachoeira Paulista - SP

Dr. Juan Carlos Ceballos



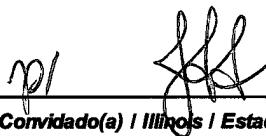
Membro da Banca | INPE | Cachoeira Paulista - SP

Dr. Enrique Viera Mattos



Convidado(a) | UNIFEI | Itajubá - MG

Dr. Stephen William Nesbitt



Convidado(a) | Illinois | Estados Unidos - USA

**Este trabalho foi aprovado por:**

maioria simples

unanimidade

**São José dos Campos, 03 de agosto de 2017**



< HUMILITY IS BORN OF KNOWING GOD AND KNOWING ONESELF. >

ST. JOSEMARIA ESCRIVA  
THE FORCE. NO. 184



TO MY FAMILY.



## ACKNOWLEDGEMENTS

I am grateful to all my colleagues and professors from the Center for Weather Forecast and Climate Studies (CPTEC-INPE) for their patience and thoughtful comments on communicating science that have opened my eyes to the nowcasting field.

Principally I acknowledge the orientation and thoughtful comments received from Dr. Luiz Machado; the help received from Dr. Enrique Mattos, Joao Huamán, Thiago Biscaro, Ramon Braga and Rute Ferreira.

Professors Julián Báez and Dirceu Herdies deserves recognition, as well. I appreciate the support they gave me so that I could start and complete this graduation course.

I also thank the Satellite Division and Environmental Systems Group (*DSA*) at the *CPTEC-INPE* for the high level of technical support.

Finally, I thank the World Meteorological Organization (*WMO*), the Paraguayan Weather Service (*DMH-Dinac*), the Graduation Course of Meteorology at the National Institute for Space Research (*PGMET-INPE*) and the Coordination for the Improvement of Higher Education Personnel (Capes), for the MSc. scholarship and financial support of this work.



## ABSTRACT

The principal objective of this research is to identify typical cloud-top signatures of incipient thunderstorms and its early electrification process in satellite multi-channel observations as means of building a conceptual model of thunderstorm detection based on brightness temperature and electrification life cycle association. The methods toward the principal objective analyzed the data set of CHUVA-Vale field campaign from 01 November 2011 to 31 March 2012, including multi-channel observations from the *SEVIRI* infrared fields, a radar-lightning co-located data set and a sample of 40 compact isolated thunderstorms. The sequence for each infrared field comprises the parallax correction in satellite observations; the co-location of satellite and radar-lightning data; the selection of an evaluation area for thunderstorm detection, and the construction of brightness temperature relative cumulative-frequency distributions along with respective thresholds analysis and validation. Consequently, 4 thunderstorm predictors used in tandem to detect the largest *differentiation* among the lightning time steps and significant cumulus *cloud* and electrification *intensification*, resulted throughout parameters in corresponding brightness temperature histograms whose thresholds are as follows: **IF1** or Predictor 1= Ch05-Ch06:  $(6.2 - 7.3) \mu\text{m}$ :  $Tbd \geq -12.0 K$ ; **IF2** or Predictor 2=  $10.8 \mu\text{m}$ :  $Tb \leq +223.0 K$ , **IF3** or Predictor 3=  $(6.2 - 10.8) \mu\text{m}$ :  $Tbd \geq -14.0 K$  and **IF4** or Predictor 4=  $(8.7 - 10.8) - (10.8 - 12.0) \mu\text{m}$ :  $Tbd \geq 0 K$ . Additionally, an independent 2-day validation test indicated that the conceptual model has a higher probability of lightning detection for the **interval** of *index sums* from 16 to 12 because of the higher *POD* and lower *FAR*. Also the results indicated that the conceptual model has a lower probability of lightning detection for the *interval* of *index sums* from 8 to 4 because of the lower *POD* and higher *FAR*. This representative behavior of the thunderstorm electrification life cycle in geostationary satellite multi-channel observations will allow a potential development of nowcasting tools at the boundary of subtropical regions using data from the Meteosat Second Generation Satellite, and with the perspective to use in the near future, the data from the Geostationary Operational Environmental Satellite-R and the imminent Meteosat Third Generation Satellite.

Keywords: Nowcasting. Thunderstorms. Electrification. Satellite multi-channel. Subtropical region.



## RESUMO

O objetivo principal desta pesquisa é identificar um conjunto de assinaturas típicas do topo das nuvens que permitam prever o processo de eletrificação quando as nuvens se transformam em tempestades. Através das combinações de canais dos imageadores de satélites geoestacionários este trabalho visa construir um modelo conceitual de detecção de início dos processos de eletrificação de tempestades utilizando a tendência dos histogramas de temperatura de brilho (ou diferença de canais). Para construção deste modelo conceitual foram utilizadas observações em diferentes canais infravermelhos co-localizados com observações de radar polarimétrico banda X e de medidas do LMA (Lightning Mapping Array) que consiste de fontes emitidas pelos relâmpagos em Very Higher Frequency. Foram selecionadas 40 tempestades compactas durante a campanha CHUVA-Vale para a elaboração do modelo conceitual e posteriormente os resultados foram testados em casos independentes. A sequência dos procedimentos metodológicos para campo de interesse compreende a correção da paralaxe nas observações de satélite; a co-localização com os dados de radar e descargas elétricas; a seleção de uma área de avaliação para detecção das tempestades e a construção de distribuições de frequência relativa-cumulativa de temperatura de brilho (ou diferenças) e a definição de limiares para a construção das frequências cumuladas. Quatro canais ou diferença de canais foram selecionados para detectar o processo de eletrificação da nuvem. Os seguintes preditores foram utilizados: **IF1** or Predictor 1 =  $(6.2 - 7.3) \mu m: Tbd \geq -12.0 K$ ; **IF2** or Predictor 2 =  $10.8 \mu m: Tb \leq +223.0 K$ , **IF3** or Predictor 3 =  $(6.2 - 10.8) \mu m: Tbd \geq -14.0 K$  and **IF4** or Predictor 4 =  $(8.7 - 10.8) - (10.8 - 12.0) \mu m: Tbd \geq 0 K$ . Esse conjunto de preditores foi utilizado em função das propriedades que esses canais têm para descrever os processos microfísicos das nuvens. Após a definição do modelo, um teste de validação independente de 2 dias permitiu definir as incertezas do modelo conceitual. O emprego dos campos selecionados quando empregados juntos melhoram significativamente a previsibilidade do processo de eletrificação da nuvem. Este comportamento representativo do ciclo de vida da eletrificação das tempestades através de combinações de canais de satélite geoestacionário permitirá o desenvolvimento de ferramentas de previsão a curtíssimo prazo nas regiões tropicais e subtropicais usando dados do Meteosat Second Generation e, em breve, do Geostationary Operational Environmental Satellite-R e do futuro Meteosat Third Generation Satellite.

Palavras-chave: Nowcasting. Tempestades. Eletrificação. Satélite. Multicanais.



## LIST OF FIGURES

	<u>Page</u>
<p>1.1 Lightning <i>time steps</i> of the thunderstorm electrification life cycle defined by Mattos et al. (2017) as (t1) - First reflectivity echo; (t2) - Intermediate time between first reflectivity radar echo and first intra-cloud flash, (t3) - First intra-cloud flash and (t4) - First cloud-to-ground flash. For this work, the same lightning <i>time steps</i> of the thunderstorm electrification life cycle will be indicated as <b>(t0)</b>, <b>(t1)</b>, <b>(t2)</b> and <b>(t3)</b>, respectively. Source: Mattos et al. (2017). . . . .</p>	2
<p>2.1 A schematic tripolar distribution showing the charging zones in a simple thunderstorm: (i) the main negative charging zone, (ii) the positive charging zone distributed above the main charging zone and (iii) the lower-smaller positive charge that is not always present in a single cell. Source: Adapted from Wallace and Hobbs (2006). . . . .</p>	6
<p>2.2 The last 2 lightning <i>time steps</i> during the evolution of a simple thunderstorm, from <b>(left)</b> the first lightning flash within the cloud itself or <i>1IC</i>, to <b>(right)</b> the first lightning flash between the cloud and the ground or <i>1CG</i>. In the cloud, the conical graupel and the small particles (ice crystal, raindrops). . . . .</p>	7
<p>2.3 Parallax in satellite meteorology: a) Displacement due to cloud height, after Weiss (1978); b) The image shows the lake (lilac surface) viewed obliquely from a distant satellite, so the surface is far from the sub-satellite point (<i>the sub-satellite point is on the Earth surface, directly beneath the satellite</i>). Source: (RADOVÁ; SEIDL, 2008), <a href="http://cimss.ssec.wisc.edu/goes/blog">http://cimss.ssec.wisc.edu/goes/blog</a> . . . . .</p>	18
<p>2.4 An example from April 2006 in the United States of America: a) Satellite image shows strong convection over northern of Wisconsin State, b) Satellite enhanced infrared image for the same time can be used for infer the height of the cloud, c) Radar image for the same time and area shows a line of convection displaced to the south of convection. Source: University of Wisconsin-Madison/Space and Engineering Center <a href="http://cimss.ssec.wisc.edu/goes/blog/archives/217">http://cimss.ssec.wisc.edu/goes/blog/archives/217</a> . . . . .</p>	19

2.5	Cold-ring shaped storm above Austria (21 June 2006, 23:55 UTC) in color enhanced image in the 10.8 $\mu m$ channel with radar data (CAPPI 15 km; 22 June 2006, 00:00 UTC) superimposed after the parallax correction. The location of the storm’s overshooting top without the parallax correction is marked by the black curve. The line A-B marks an examined cross-section. Source: Radová and Seidl (2008). . . . .	20
2.6	Measures radiances ( $mW m^2 sr^{-1} cm$ ) for fields of view partially filled with clouds. The line connects the centers of scattered radiance values in both spectral bands, and the curve represents the calculations of radiance for both spectral channels for semi-transparent clouds and surface. At the bottom, the intersection indicates the radiance correction of a semi-transparent cloud. Source: Nieman et al. (1993). . . . .	21
3.1	<b>(left)</b> The CHUVA’s experimental sites and the main precipitations regimes in Brazil. The focus of our study is the Vale do Paraíba campaign in southeastern Brazil; indicated with <i>red circles</i> . <b>(right)</b> The CHUVA’s reference measurement strategy during field campaigns along with the radar site and main site with other instruments. . . . .	23
3.2	Main site of the CHUVA-Vale field campaign. Location of the X-band radar ( <i>grey radar</i> ) and other S-band radars such as São Roque, FCTH and IACIT ( <i>black/white radars</i> ). The <i>yellow</i> circle represents the covering extent of X-band radar of 60 <i>km</i> . Location of the CHUVA instruments sites ( <i>yellow stick pins</i> ) and lightning sensors such as SPLMA ( <i>blue stick pins</i> ); LINET and EarthNetworks ( <i>cyan stick pins</i> ), and TL200 ( <i>red flags</i> ). The blue circle represents the area of 3-D lightning mapping of the SPLMA stations. . . . .	24
3.3	The CHUVA-Vale field campaign region. The XPOL radar ( <i>gray diamond</i> ) in São José Dos Campos; distance rings (20, 60, and 100 <i>Km</i> ) from the XPOL radar ( <i>dashed lines</i> ), lightning networks from Brasil-DAT ( <i>blue stars</i> ) and SPLMA ( <i>red filled circles</i> ) and 46 thunderstorms at the 1CG ( <i>t3</i> ) ( <i>asterisks</i> ). . . . .	28
3.4	Data ( <i>red rectangles</i> ); methods and tests ( <i>yellow and grey rectangles</i> ), and verification ( <i>green rectangle</i> ) for a conceptual model of thunderstorm detection. . . . .	31

3.5	The MSG-8 scanning domain and the southeastern region of Brazil located in the extreme corner of this domain. The image is observed in the infrared $10.8 \mu m$ channel on March 15, 2007 at 1200 UTC. . . . .	32
3.6	Illustration ( <i>not to scale</i> ) of the concept of the parallax correction, where <b>B</b> is the observed position and <b>A</b> is the cloud's true location. . . . .	33
3.7	Cloud-top height calculations for the parallax correction in <i>MSG</i> satellite imagery. For height calculations has been employed a functionality from <i>DSA-CPTEC/INPE</i> based in the $H_2O - IRW$ intercept method. For parallax correction has been employed a functionality from <i>EUMETSAT</i> . . . . .	34
3.8	Thunderstorm case study observed in $10.8 \mu m$ channel on March 10, 2012 at 1530 UTC. <b>(left)</b> Satellite image without the parallax correction and <b>(right)</b> satellite image with the parallax correction. Pixels without information (or <i>black</i> pixels in the corrected satellite image) are not taken into account. . . . .	35
3.9	Thunderstorm observed on March 10, 2012; within a $75 Km \times 75 Km$ extension. <b>(left)</b> Radar echo plots of the electrification life cycle evolution from the first radar echo up to the time of the cloud-to-ground flash corresponding to $1Echo (t_0) = 1448$ UTC; $Int (t_1) = 1500$ UTC; $1IC (t_2) = 1518$ UTC, and $1CG (t_3) = 1530$ UTC; <b>(right)</b> $10.8 \mu m$ channel plots of the thunderstorm evolution at the co-located lightning <i>time steps</i> : $1Echo (t_0) = 1445$ UTC, $Int (t_1) = 1500$ UTC, $1IC (t_2) = 1515$ UTC, and $1CG (t_3) = 1530$ UTC. . . . .	36
3.10	<i>Tb relative frequency</i> distributions of $10.8 \mu m$ channel for a thunderstorm electrification life cycle observed on March 10, 2012 within the evaluation areas of <b>(a)</b> $25 Km \times 25 Km$ , <b>(b)</b> $30 Km \times 30 Km$ and <b>(c)</b> $37.5 Km \times 37.5 Km$ , respectively, centered around the following lightning <i>time steps</i> : $1Echo (t_0) = 1445$ UTC; $Int (t_1) = 1500$ UTC; $1IC (t_2) = 1515$ UTC, and $1CG (t_3) = 1530$ UTC. These distributions have class interval width of $+4.0 K$ . . . . .	38
3.11	Absorption spectrum of electromagnetic radiation by the Earth's atmosphere across a wide wavelength range. Five of the most used IR channels from <i>Meteosat Satellites</i> are indicated with arrows: Channels 5 and 6 (water vapor image), channels 9 and 10 (infrared images), and channel 7 ( $8.7 \mu m$ ). . . . .	39
3.12	Schematic depiction of radiative coupling in water vapor channels as an indicator of moisture content at medium levels of the troposphere. F is the longwave emission upward by the troposphere at medium levels. . . .	40

3.13	Schematic figure of radiative coupling in infrared channel between the surface and a layer of clouds. $F_1$ and $F_2$ are the incident shortwave flux from the sun, $F_3$ and $F_5$ are the longwave emission by the surface and $F_4$ is the longwave emission by the layer of clouds. . . . .	42
3.14	<i>Histograms</i> of <b>(a)</b> (6.2 – 7.3) $\mu\text{m}$ channel difference and <b>(b)</b> 10.8 $\mu\text{m}$ channel for a thunderstorm observed on March 10, 2012 within an evaluation area of 30 $\text{km} \times 30 \text{ Km}$ centered around the following <i>time steps</i> : 1 <i>Echo</i> ( $t_0$ ) = 1445 UTC; 1 <i>Int</i> ( $t_1$ ) = 1500 UTC; 1 <i>IC</i> ( $t_2$ ) = 1515 UTC, and 1 <i>CG</i> ( $t_3$ ) = 1530 UTC. These <i>histograms</i> have class interval width of +4.0 $K$ . . . . .	44
3.15	The 10.8 $\mu\text{m}$ "less" distributions for <i>thresholds</i> from $Tb \leq +263.0 K$ plotted against each lightning <i>time step</i> considering a thunderstorm observed on March 10, 2012 within an evaluation area of 30 $\text{km} \times 30 \text{ km}$ centered around respective <i>time steps</i> : 1 <i>Echo</i> ( $t_0$ ) = 1445 UTC; 1 <i>Int</i> ( $t_1$ ) = 1500 UTC; 1 <i>IC</i> ( $t_2$ ) = 1515 UTC, and 1 <i>CG</i> ( $t_3$ ) = 1530 UTC. The <i>thresholds</i> of $Tb \leq +215.0 K$ have negligible slopes. . . . .	49
3.16	$Tb$ relative cumulative-frequency or "less" distribution with greater value of <i>maxima derivative</i> plotted against each <i>time step</i> considering a thunderstorm observed through the 10.8 $\mu\text{m}$ channel on March 10, 2012 within an area of 30 $\text{km} \times 30 \text{ Km}$ centered around respective <i>time steps</i> : 1 <i>Echo</i> ( $t_0$ )= 1445 UTC; 1 <i>Int</i> ( $t_1$ )= 1500 UTC; 1 <i>IC</i> ( $t_2$ )= 1515 UTC, and 1 <i>CG</i> ( $t_3$ )= 1530 UTC. The <i>threshold</i> with greater value of <i>maxima derivative</i> is $Tb= +231.0 K$ . . . . .	49
4.1	$Tbd$ <i>histograms</i> of (6.2 – 7.3) $\mu\text{m}$ interest field for a sample of 40 thunderstorms size within an evaluation area of 30 $\text{km} \times 30 \text{ km}$ centered around respective lightning <i>time steps</i> . The <i>histograms</i> interval width is +4.0 $K$ . . . . .	52
4.2	The (6.2 – 7.3) $\mu\text{m}$ relative cumulative-frequency or "more" distributions curves from <i>thresholds</i> established as $Tbd \geq -16.0 K$ considering 40 compact thunderstorms cases studies within an evaluation area of 30 $\text{km} \times 30 \text{ km}$ centered around respective lightning <i>time steps</i> . The threshold with greater value of <i>maxima derivative</i> is $Tbd= -12.0 K$ , indicated with a <i>black asterisk</i> . Also see table 4.2. . . . .	54
4.3	$Tb$ <i>histograms</i> of the 10.8 $\mu\text{m}$ interest field for a sample of 40 thunderstorms size within an evaluation area of 30 $\text{km} \times 30 \text{ km}$ centered around respective lightning <i>time steps</i> . The <i>histograms</i> interval width is +4.0 $K$ . . . . .	57

4.4	The $10.8 \mu m$ $Tb$ relative cumulative-frequency or "less" distributions from <i>thresholds</i> established as $Tb \leq +235.0 K$ . The $10.8 \mu m$ $Tb$ relative cumulative-frequency distribution or "less" curve with greater value of <i>maxima derivative</i> plotted against each lightning <i>time step</i> and corresponding to a <i>threshold</i> with value of $+223.0 K$ ; considering 40 thunderstorms within an area of $30 km \times 30 km$ centered around respective <i>time steps</i> . . . . .	59
4.5	$Tbd$ histograms of the $(6.2 - 10.8) \mu m$ interest field for a sample of 40 thunderstorms size within an evaluation area of $30 km \times 30 km$ centered around respective lightning <i>time steps</i> . The <i>histograms</i> interval width is $+4.0 K$ . . . . .	60
4.6	The $(6.2 - 10.8) \mu m$ $Tbd$ relative cumulative-frequency or "more" distributions curves from <i>thresholds</i> established as $Tbd \geq -14.0 K$ considering 40 thunderstorms cases studies within an evaluation area of $30 km \times 30 km$ centered around respective lightning <i>time steps</i> . The <i>thresholds</i> with greater value of <i>maxima derivative</i> is $Tbd = -14.0 K$ at the $1CG$ ( $t3$ ) <i>time step</i> , indicated with a <i>black asterisk</i> . Also see table 4.8. . . . .	63
4.7	$Tbd$ histograms of the <i>trispectral</i> interest field for a sample of 40 thunderstorms size within an evaluation area of $30 km \times 30 km$ centered around respective lightning <i>time steps</i> . The <i>histograms</i> interval width is $+4.0 K$ . . . . .	66
4.8	<i>Trispectral</i> $Tbd$ relative cumulative-frequency or "more" distributions curves from <i>thresholds</i> established as $Tbd \geq 0 K$ ; considering 40 thunderstorms cases studies within an evaluation area of $30 km \times 30 km$ centered around respective lightning <i>time steps</i> . The $Tbd$ <i>threshold</i> with greater value of <i>maxima derivative</i> is indicated with a <i>black asterisk</i> (see table 4.11). . . . .	68
4.9	<i>Thunderstorm predictors</i> using <i>SEVIRI</i> infrared ( <i>IR</i> ) fields for a nowcasting tool as follows: <b>Predictor 1 - Ch05-Ch06:</b> $(6.2 - 7.3) \mu m$ ; <b>Predictor 2 - Ch09:</b> $10.8 \mu m$ , <b>Predictor 3 - Ch05-Ch09:</b> $(6.2 - 10.8) \mu m$ and <b>Predictor 4 - Trispectral:</b> $(8.7 - 10.8) - (10.8 - 12.0) \mu m$ . The relation $(Tbd > Thr)$ is for a "less" distribution with greater value of <i>maxima derivative</i> ; on the contrary way is for $(Tbd < Thr)$ . The lightning <i>time step</i> location of the greater value of <i>maxima derivative</i> is indicated with <i>asterisk</i> . The <i>range</i> and <i>average</i> values allows a rapid analysis of corresponding <i>nowcasting</i> parameters. . . . .	72

6.1 Synthesis of the conceptual model of thunderstorm detection using all 4 predictors thresholds as  $Tbd = -12.0 K$  for **IF1= Ch05-Ch06**:  $(6.2 - 7.3) \mu m$ ;  $Tb = +223.0 K$  for **IF2= Ch09**:  $10.8 \mu m$ ;  $Tbd = -14.0 K$  for **IF3= Ch05-Ch09**:  $(6.2 - 10.8) \mu m$ , and  $Tbd = 0 K$  for **IF4= Trispectral**:  $(8.7 - 10.8) - (10.8 - 12.0) \mu m$ . . . . . 91

## LIST OF TABLES

	<u>Page</u>
2.1 Means and std dev values of <i>interest fields</i> for 123 growing cumulus prior of convective and lightning initiation events observed over Europe. These 123 events involved observing towering cumuli that evolved over three successive 15-min images into a large cumulus cloud or a cloud with a new anvil. The trispectral <i>interest field</i> is $(8.7 - 10.8) - (10.8 - 12.0) \mu m$ . . . . .	12
2.2 Critical values ( <i>indicate occurrence of ice clouds</i> ) by category . The trispectral <i>interest field</i> is $(8.7 - 10.8) - (10.8 - 12.0) \mu m$ . Multi-channel-differencing <i>time trends</i> evaluate various <i>IR</i> cloud properties in time. . . . .	14
3.1 Summary of SEVIRI spectral channels from MSG geostationary satellite . . .	26
3.2 Operating parameters of XPOL radar during the CHUVA-Vale Campaign . .	27
3.3 The $10.8 \mu m$ <i>Tb relative frequency</i> and "less" distributions for <i>thresholds</i> from $Tb \leq +235.0 K$ during <i>1Echo</i> and <i>1CG</i> of a thunderstorm observed on March 10, 2012 within an evaluation area of $30 km \times 30 Km$ centered around respective lightning <i>time steps</i> : <i>1Echo</i> = 1445 UTC and <i>1CG</i> = 1530 UTC. . .	47
3.4 The <i>Tb thresholds</i> of <i>maxima derivative</i> and correspondent lightning <i>time step</i> locations in the $10.8 \mu m$ "more" distributions curves considering a thunderstorm observed through the $10.8 \mu m$ channel on March 10, 2012 within an area of $30 km \times 30 Km$ centered around respective <i>time steps</i> : <i>1Echo</i> ( $t_0$ )= 1445 UTC; <i>Int</i> ( $t_1$ )= 1500 UTC; <i>1IC</i> ( $t_2$ )= 1515 UTC, and <i>1CG</i> ( $t_3$ )= 1530 UTC. The <i>threshold</i> with greater value of <i>maxima derivative</i> is $Tb = +231.0 K$ ( <i>asterisk</i> ).The <i>thresholds</i> of $Tb \leq +215.0 K$ have negligible slopes. . . . .	50
4.1 Mean, standard deviation, median and minimum values for the $(6.2 - 7.3) \mu m$ <i>Tbd histograms</i> of $+4.0 K$ interval width considering the sample of 40 thunderstorms size (see figure 4.1). These <i>Tbd</i> values are compared above with the values of Mecikalski et al. (2010) indicated in 3.3.4.1. . .	53
4.2 <i>Tbd thresholds</i> values of <i>maxima derivative</i> and correspondent lightning <i>time step</i> location in the $(6.2 - 7.3) \mu m$ "more" distributions (see figure 4.2). The <i>Tbd threshold</i> with greater value of <i>maxima derivative</i> is $-12.0 K$ ( <i>asterisk</i> ). . . . .	55

4.3	The (6.2–7.3) $\mu\text{m}$ <i>Tbd</i> relative frequency and "more" distributions from thresholds established as $Tbd \geq -16.0 K$ ; considering 40 thunderstorms cases studies within an evaluation area of $30 \text{ km} \times 30 \text{ km}$ centered around respective lightning <i>time steps</i> . The <i>Tbd</i> threshold with greater value of <i>maxima derivative</i> is indicated with an <i>asterisk</i> (see table 4.2). . . . .	56
4.4	Mean, standard deviation, median and minimum values for 10.8 $\mu\text{m}$ histograms of $Tb = +4.0 K$ interval width considering the sample of 40 thunderstorms size (see figure 4.3). These statistical values are compared above with the values of Mecikalski et al. (2010) indicated in 3.3.4.1. . . . .	58
4.5	The <i>Tb</i> thresholds of <i>maxima derivative</i> and correspondent lightning <i>time step</i> locations in the 10.8 $\mu\text{m}$ "more" distributions curves. The threshold with greater value of <i>maxima derivative</i> is $Tb = +223.0 K$ ( <i>asterisk</i> ). . . . .	60
4.6	The 10.8 $\mu\text{m}$ <i>Tb</i> relative frequency and "less" distributions for 1 <i>Echo</i> and 1 <i>CG</i> time steps, considering thresholds from $Tb \leq +235.0 K$ and 40 cases within an evaluation area of $30 \text{ km} \times 30 \text{ km}$ . The <i>Tb</i> threshold with greater value of <i>maxima derivative</i> is indicated with an <i>asterisk</i> (see table 4.5). . . . .	61
4.7	Mean, standard deviation, median and minimum values for the (6.2 – 10.8) $\mu\text{m}$ histograms of $Tbd = +4.0 K$ interval width considering the sample of 40 thunderstorms size (see figure 4.5). These statistical values are compared above with the values of Mecikalski et al. (2010) indicated in 3.3.4.1. . . . .	62
4.8	<i>Tbd</i> thresholds values of <i>maxima derivative</i> and correspondent lightning <i>time step</i> location in the (6.2 – 10.8) $\mu\text{m}$ "more" distributions (see figure 4.6). The <i>Tbd</i> threshold with greater value of <i>maxima derivative</i> is $-14.0 K$ ( <i>asterisk</i> ). . . . .	64
4.9	The (6.2 – 10.8) $\mu\text{m}$ <i>Tbd</i> relative frequency and "more" distributions from thresholds established as $Tbd \geq -14.0 K$ ; considering 40 thunderstorms cases studies within an evaluation area of $30 \text{ km} \times 30 \text{ km}$ centered around respective lightning <i>time steps</i> . The <i>Tbd</i> threshold with greater value of <i>maxima derivative</i> is indicated with an <i>asterisk</i> (see table 4.8). . . . .	65
4.10	Mean, standard deviation, median and minimum values for the trispectral histograms of $Tbd = +1.0 K$ interval width considering the sample of 40 thunderstorms size (see figure 4.7). These statistical values are compared above with the values of Mecikalski et al. (2010) indicated in 3.3.4.1. . . . .	67

4.11	<i>Tbd thresholds</i> values of <i>maxima derivative</i> and correspondent lightning <i>time step</i> location in the <i>trispectral "more"</i> distributions (see figure 4.8). The <i>Tbd threshold</i> with greater value of <i>maxima derivative</i> is 0 K ( <i>asterisk</i> ). . . . .	69
4.12	The <i>trispectral Tbd relative frequency</i> and " <i>more</i> " distributions from <i>thresholds</i> established as $Tbd \geq 0 K$ ; considering 40 thunderstorms cases studies within an evaluation area of 30 km × 30 km centered around respective lightning <i>time steps</i> . The <i>Tbd threshold</i> with greater value of <i>maxima derivative</i> is indicated with an <i>asterisk</i> (see table 4.11). . . . .	70
5.1	The (6.2 – 7.3) $\mu m$ channel difference's verification using lightning data from BrasilDAT network accumulated every 15 <i>min</i> and 15 <i>min</i> -satellite images during 1-day with significant lightning activity (January 17, 2012) at 41 evaluation areas of 30 km × 30 km within the CHUVA-Vale region. . . . .	77
5.2	The (6.2 – 7.3) $\mu m$ channel difference's verification using lightning data from BrasilDAT network accumulated every 15 <i>min</i> and 15 <i>min</i> -satellite images during 1-day with significant lightning activity (March 13, 2012) at 41 evaluation areas of 30 km × 30 km within the CHUVA-Vale region. . . . .	78
5.3	The 10.8 $\mu m$ channel's verification using lightning data from BrasilDAT network accumulated every 15 <i>min</i> and 15 <i>min</i> -satellite images during 1-day with significant lightning activity (January 17, 2012) at 41 evaluation areas of 30 km × 30 km within the CHUVA-Vale region. . . . .	79
5.4	The 10.8 $\mu m$ channel's verification using lightning data from BrasilDAT network accumulated every 15 <i>min</i> and 15 <i>min</i> -satellite images during 1-day with significant lightning activity (March 13, 2012) at 41 evaluation areas of 30 km × 30 km within the CHUVA-Vale region. . . . .	80
5.5	The (6.2 – 10.8) $\mu m$ channel difference's verification using lightning data from BrasilDAT network accumulated every 15 <i>min</i> and 15 <i>min</i> -satellite images during 1-day with significant lightning activity (January 17, 2012) at 41 evaluation areas of 30 km × 30 km within the CHUVA-Vale region. . . . .	81
5.6	The (6.2 – 10.8) $\mu m$ channel difference's verification using lightning data from BrasilDAT network accumulated every 15 <i>min</i> and 15 <i>min</i> -satellite images during 1-day with significant lightning activity (March 13, 2012) at 41 evaluation areas of 30 km × 30 km within the CHUVA-Vale region. . . . .	82
5.7	<i>Trispectral</i> channel difference's verification using lightning data from BrasilDAT network accumulated every 15 <i>min</i> and 15 <i>min</i> -satellite images during 1-day with significant lightning activity (January 17, 2012) at 41 evaluation areas of 30 km × 30 km within the CHUVA-Vale region. . . . .	83

5.8	<i>Trispectral</i> channel difference's verification using lightning data from BrasilDAT network accumulated every 15 <i>min</i> and 15 <i>min</i> -satellite images during 1-day with significant lightning activity (March 13, 2012) at 41 evaluation areas of 30 <i>km</i> × 30 <i>km</i> within the CHUVA-Vale region. . . . .	84
5.9	Contingency table for the <i>index sum</i> of 4 <i>interest fields</i> ; using the comparison between lightning data occurred and predicted by the conceptual model during 2-days with significant lightning activity at evaluation areas of 30 <i>km</i> × 30 <i>km</i> within the CHUVA-Vale region. The <i>index sum</i> is the total sum (from 16 to 4) of 4 <i>interest fields</i> <i>émph</i> indices (from 4 to 0). The <i>occurrences</i> are the number of evaluation areas that reach the corresponding <i>index sum</i> . . . . .	84
5.10	Contingency table for the <b>intervals</b> of <i>index sum</i> of 4 <i>interest fields</i> ; using the comparison between lightning data occurred and predicted by the conceptual model during 2-days with significant lightning activity at evaluation areas of 30 <i>km</i> × 30 <i>km</i> within the CHUVA-Vale region. The <i>index sum</i> is the total sum (from 16 to 4) of 4 <i>interest fields</i> <i>indices</i> (from 4 to 0). The <b>interval</b> <i>index sum</i> are 3 intervals with <i>index sum</i> from 16 to 12; 12 to 8 and 8 to 4, respectively. The <i>occurrences</i> are the number of evaluation areas that reach the corresponding <b>interval</b> <i>index sum</i> . . . . .	85

# CONTENTS

	<u>Page</u>
<b>1 Introduction</b> . . . . .	<b>1</b>
1.1 Problem statement . . . . .	3
1.2 Research goals . . . . .	4
<b>2 Literature Synthesis</b> . . . . .	<b>5</b>
2.1 Thunderstorm electrification . . . . .	5
2.2 Nowcasting and very short-range forecasts of thunderstorms . . . . .	7
2.2.1 Techniques for nowcasting and very short-range nowcasts . . . . .	8
2.2.1.1 Multi-channel satellite applications . . . . .	9
2.2.2 Problem of parallax in satellite meteorology . . . . .	18
2.2.2.1 Cloud height calculation . . . . .	20
<b>3 Data and Methods</b> . . . . .	<b>23</b>
3.1 The CHUVA project and the CHUVA-Vale field campaign . . . . .	23
3.2 Data . . . . .	25
3.2.1 Meteorological Satellite (Meteosat) Data . . . . .	25
3.2.2 Radar data . . . . .	26
3.2.3 Lightning Data . . . . .	28
3.2.4 Thunderstorms cases studies . . . . .	29
3.2.5 Co-located radar-lightning data set . . . . .	30
3.3 Methods . . . . .	30
3.3.1 Parallax correction . . . . .	32
3.3.2 Co-location of radar-lightning and satellite data . . . . .	35
3.3.3 Selection of an evaluation area for thunderstorm detection . . . . .	37
3.3.4 Inspection of IR <i>interest fields</i> for thunderstorm detection . . . . .	38
3.3.4.1 Ch05-Ch06: $(6.2 - 7.3) \mu m$ . . . . .	39
3.3.4.2 Ch09: $10.8 \mu m$ . . . . .	41
3.3.4.3 Ch05-Ch09: $(6.2 - 10.8) \mu m$ . . . . .	41
3.3.4.4 Trispectral: $[(8.7 - 10.8) - (10.8 - 12.0)] \mu m$ . . . . .	42
3.3.5 Construction of the <i>Tb (Tbd) histograms</i> of IR interest fields . . . . .	43
3.3.6 <i>Thresholds</i> settings for analysis of the <i>Tb (Tbd) histograms</i> . . . . .	44
3.3.7 Construction of the <i>Tb (Tbd) relative cumulative-frequency curves</i> . . . . .	45
3.3.8 Analysis of the <i>Tb (Tbd) relative cumulative-frequency curves</i> . . . . .	46

<b>4</b>	<b>Results</b>	<b>51</b>
4.1	Thunderstorm detection using each <i>IR interest field</i> imagery	51
4.1.1	(6.2 – 7.3) $\mu\text{m}$ : <i>Tbd histograms</i> and statistical values	51
4.1.2	(6.2 – 7.3) $\mu\text{m}$ : <i>Tbd thresholds</i> and <i>histograms</i> populations	53
4.1.3	10.8 $\mu\text{m}$ : <i>Tb histograms</i> and statistical values	55
4.1.4	10.8 $\mu\text{m}$ : <i>Tb thresholds</i> and <i>histograms</i> populations	58
4.1.5	(6.2 – 10.8) $\mu\text{m}$ : <i>Tbd histograms</i> and statistical values	59
4.1.6	(6.2 – 10.8) $\mu\text{m}$ : <i>Tbd thresholds</i> and <i>histograms</i> populations	63
4.1.7	<i>Trispectral</i> : <i>Tbd histograms</i> and statistical values	66
4.1.8	<i>Trispectral</i> : <i>Tbd thresholds</i> and <i>histograms</i> populations	67
4.2	Thunderstorm detection using 4 <i>IR interest fields</i> imagery	71
<b>5</b>	<b>Verification of the conceptual model of thunderstorm detection</b>	<b>73</b>
<b>6</b>	<b>Conclusions</b>	<b>87</b>
	<b>REFERENCES</b>	<b>93</b>

## 1 Introduction

Thunderstorms could be associated with many potential sources of danger such as turbulence, hail and heavy rain, downbursts and gust fronts, lightning, tornadoes and mesocyclones (STULL, 2015). The National Severe Storms Laboratory of the United States estimates 16 million thunderstorms each year worldwide, and at any given moment, 2000 thunderstorms in progress; also classifies a *severe* thunderstorm when containing one or more of these elements: (i) hail of size 2.5 cm or greater; (ii) gusting winds of 92.6 km/h or greater, or (iii) tornado (<http://www.nssl.noaa.gov/education/svrwx101/thunderstorms/>).

Under the right conditions, thunderstorms and convective precipitation causes flash flooding, killing more people each year than other weather events; besides the hazards related to thunderstorms cost the aviation industry many tens of millions of dollar annually. About thunderstorms associated with lightning in Brazil, is estimated that approximately 60-75 million lightning flashes occur every year and in part, these lightning strikes have been responsible for the death of an average of 132 people every year in the country (CARDOSO et al., 2014). Various sectors of the economy are using weather forecast information for planning activities and decision-making such as industry, construction, energy, transport, aviation, etc. In South America; where a large number of mesoscale convective systems (MCSs) have been studied extensively, there is a requirement to accurately predict the thunderstorm initial electrification phase and evolution because of the rapidly changing phenomena that often adversely impact population and industry (ZIPSER et al., 2006; SALIO et al., 2007; DURKEE; MOTE, 2010). For example in Brazil, the National Integrated Network for lightning detection (RINDAT), the Brazilian Lightning Detection Network (BrasilDAT) and the Sferics Timing and Ranging Network (STARNET) provide information for the Center for Weather Forecast and Climate Studies (CPTEC) and the National Center for Monitoring and Alerting Natural Disasters (CEMADEN) to support their activities related with risk management.

In thunderstorms studies is important to contemplate the single cell evolution that according to the Thunderstorm Project (U.S. Weather Bureau) can be divided into three stages as follows: *Cumulus* ( $t_0$ ) - characterized by updraft throughout the cell, *Mature* ( $t_1$ ) - characterized by presence of both updrafts and downdrafts at least in the lower half of the cell and *Dissipating* ( $t_2$ ) - characterized by weak downdrafts prevailing throughout the cell. However, to gain a better understanding of the convective and the electrification processes, our study have considered the

single cell evolution defined by [Mattos et al. \(2017\)](#) in lightning *time steps* as follows: *1Echo* ( $t_0$ ) - the first radar echo with any value of reflectivity above the reflectivity noise level at any height; *Int* ( $t_1$ ) - intermediate stage between first reflectivity echo and first intra-cloud lightning flash, *1IC* ( $t_2$ ) - the first intra-cloud lightning flash and *1CG* ( $t_3$ ) - the first cloud-to-ground lightning flash.

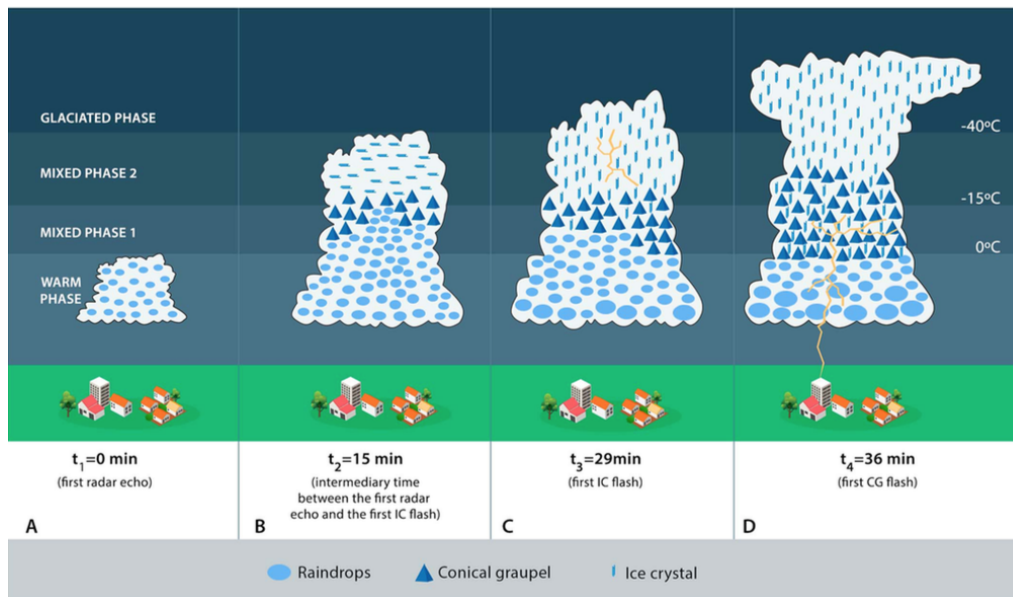


Figure 1.1 - Lightning *time steps* of the thunderstorm electrification life cycle defined by [Mattos et al. \(2017\)](#) as ( $t_1$ ) - First reflectivity echo; ( $t_2$ ) - Intermediate time between first reflectivity radar echo and first intra-cloud flash, ( $t_3$ ) - First intra-cloud flash and ( $t_4$ ) - First cloud-to-ground flash. For this work, the same lightning *time steps* of the thunderstorm electrification life cycle will be indicated as ( $t_0$ ), ( $t_1$ ), ( $t_2$ ) and ( $t_3$ ), respectively. Source: [Mattos et al. \(2017\)](#).

For many years, the geostationary satellite data have been used to acquire knowledge on convective processes and large-scale assessments of convective, lightning-producing storms systems. In fact, the analysis of satellite multi-channel data has demonstrated its ability to depict cloud-top properties and the combination of the *infrared interest fields* (individual channels, channel differences and time trends) has been largely used to describe deep convective clouds ([SCHMETZ et al., 1997](#); [MACHADO et al., 2009](#); [MATTHEE; MECIKALSKI, 2013](#); [WAGNER; MACHADO, 2013](#)).

Furthermore, thinking about the recently launched Geostationary Operational Environmental Satellite-R (*GOES-R*), as well as, thinking about the imminent Meteosat Third Generation (*MTG*), the interest in using these platforms for better describing

the thunderstorms early electrification process and evolution will remain high.

Additionally, the dual-polarization radar measurements provide a unique ability to improve thunderstorms remote sensing via the identification of hydrometeor type, phase, shape, and concentration. However, previous works linking observations from geostationary satellite, ground-based radar and/or lightning detection networks are still limited (WOLF, 2006; MOSIER et al., 2011; ROEDER; MCNAMARA, 2011; WOODARD et al., 2012; MECIKALSKI et al., 2013; KARAGIANNIDIS et al., 2016).

To contribute to the understanding on thunderstorms life cycle and its early electrification process, the utilization of satellite multi-channel data is an increasing demand for the next generation of weather warning systems; that will also be integrating radar and/or lightning information, numerical modeling predictions and/or data assimilation for high-resolution meteorological analyses in nowcasting tools. Hence, this demand leads to the problem statement of the present study.

### 1.1 Problem statement

Nowcasts or weather forecasting in the 0-6 hours time interval has had a low skill because of the limitations of the techniques based on extrapolation of existing thunderstorms conditions, so new tools are been developed to improve thunderstorms detection and forecast. The literature survey shows a few researchers analyzing the thunderstorms detection and forecast using satellite multi-channel data.

The motivation of the present study is to increase understanding on how cumulus clouds evolve to thunderstorms using multi-channel observations from the *SEVIRI* infrared (*IR*) fields, a radar-lightning co-located data set and a large sample of compact isolated thunderstorms. In order to fulfill this, the following questions must be addressed:

- Are there typical satellite cloud-top signatures before the lightning-initiation process? Do these signatures observe how cumulus clouds evolve to thunderstorms and how the first intra-cloud lightning and cloud-to-ground lightning flashes are produced during incipient thunderstorms?
- Is there a representative behavior of incipient thunderstorms and its early electrification process to build a conceptual model for warning system using multi-channel data from the *SEVIRI* infrared fields?

These answers allow a potential development of nowcasting tools to forecast the

evolution of the thunderstorm electrification life cycle at the boundary of tropical and subtropical regions using observations from the Meteosat Second Generation (*MSG*) Satellite, and in the short-term, using observations from the recently launched Geostationary Operational Environmental Satellite-R (*GOES-R*).

## 1.2 Research goals

This study has as purpose to assess the ability of the satellite multi-channel observations integrating a radar-lightning co-located data set as means of detection of the thunderstorm electrification life cycle. The research goals are itemized below:

- Evaluation of multi-channel data from the *SEVIRI IR* fields for detection of the electrification life cycle of isolated and compact thunderstorms.
- Build a conceptual model of thunderstorm detection based on brightness temperature and electrification life cycle association, and corresponding thresholds analysis for each *IR* interest field.

Therefore, this document contains the following: *Literature synthesis* in chapter 2; *Data and Methods* in chapter 3; *Results* in chapter 4, *Verification* of the conceptual model of thunderstorm detection in chapter 5 and *Conclusions* in chapter 6.

## 2 Literature Synthesis

The literature synthesis covers a review of ideas concerning *thunderstorms* in section 2.1; the *nowcasting* and *very short-range* forecasts of thunderstorms in section 2.2; some *techniques* for nowcasting and very short-range nowcasts in subsection 2.2.1 and the *parallax* application in subsection 2.2.2; which is important for thunderstorms analyses when comparing satellite and radar data.

### 2.1 Thunderstorm electrification

Thunderstorms can be classified as single cells or simple thunderstorms described by the 3 stages: cumulus, mature and dissipating; as multicellular thunderstorms or group of single cells each at varying stages in their lifecycle, and as super-cell thunderstorm that is an intense and relatively large thunderstorm that produces severe weather and can last for several hours, but its occurrence is rare in the tropics ([https://www.meted.ucar.edu/tropical/synoptic/local\\_storms/navmenu.php?tab=1&page=1.0.0&type=flash](https://www.meted.ucar.edu/tropical/synoptic/local_storms/navmenu.php?tab=1&page=1.0.0&type=flash)).

To analyze the simple thunderstorms processes, these have been considered in the form of isolated small precipitating cells described by the 4 lightning *time steps*: *1Echo* ( $t_0$ ) - the first radar echo with any value of reflectivity above the reflectivity noise level at any height; *Int* ( $t_1$ ) - intermediate stage between first reflectivity echo and first intra-cloud lightning flash, *1IC* ( $t_2$ ) - the first intra-cloud lightning flash and *1CG* ( $t_3$ ) - the first cloud-to-ground lightning flash (MATTOS et al., 2017).

A review in the Thunderstorm Project (U.S. Weather Bureau) indicated that the following elements can be considered as principal characteristics in reflecting the character and intensity of the thunderstorm processes: (i) Vertical motions, considered to be the lifeblood of the thunderstorm; (ii) Horizontal motions, recognized as necessary compensations resulting from the vertical motion; (iii) Horizontal and vertical temperature gradients, recognized as the determining factors for convective motions; (iv) Electrical fields, apparently indicative of thunderstorm intensity; (v) Rainfall distribution/intensity, indicative of the nature/intensity of the thunderstorm; (vi) Temperature changes at the ground, indicative of intensity and of the nature of the thermodynamic processes; (vii) Pressure changes at the ground, indicative of vertical accelerations; (viii) Surface wind fluctuations, indicative of thunderstorm intensity and (ix) Turbulence as the basic measure of thunderstorm intensity.

Also based on the review made in Wallace and Hobbs (2006) for the distribution of charges in a single cell, it can be stated that repeated measurements showed the main negative charging zone located between the  $-10^{\circ}\text{C}$  and  $-20^{\circ}\text{C}$  temperature levels, the zone of positive-charge concentration located above the negative-charge center, and the small centers of positive charge located in the lower part of a cell but not always present (See figure 2.1).

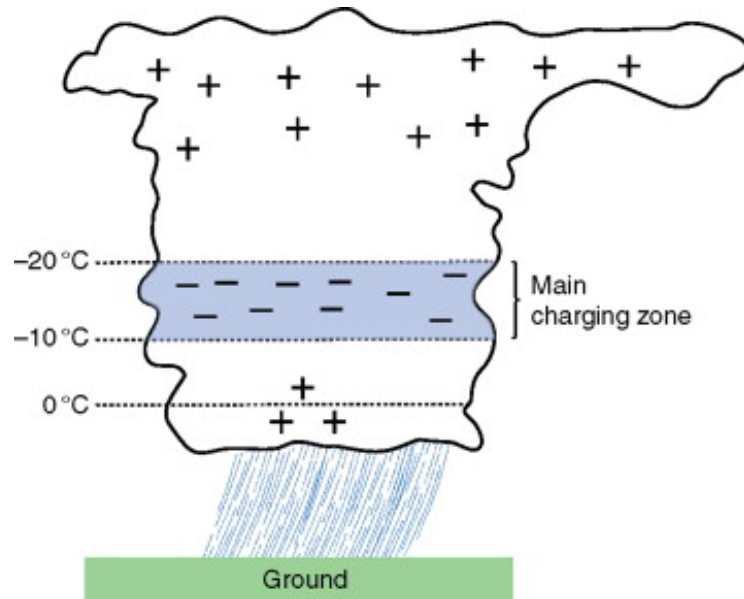


Figure 2.1 - A schematic tripolar distribution showing the charging zones in a simple thunderstorm: (i) the main negative charging zone, (ii) the positive charging zone distributed above the main charging zone and (iii) the lower-smaller positive charge that is not always present in a single cell.  
Source: Adapted from Wallace and Hobbs (2006).

With the charge distribution in a cell and the intensity of the electric field exceeding that which the air can sustain, the consequence is a dielectric breakdown taking the form of an intra-cloud lightning flash (within the cloud itself or between clouds, or from the cloud to the air), or taking the form of a cloud-to-ground lightning flash (between the cloud and the ground) (WALLACE; HOBBS, 2006). See figure 2.2 for the last 2 lightning *time steps*, our study contemplates the thunderstorm evolution from the first intra-cloud flash (1IC) to the first cloud-to-ground flash (1CG).

Considering this charge distribution as a result of repeated measurements, many theories relate strong electrification followed by heavy precipitation within the cell in the form of graupel or hailstones detected by radar. Also many theories assume that as the graupel falls through a cell it is charged negatively due to collisions with

small cloud particles (ice crystal, raindrops), giving rise to the negative charge in the main charging zone. The positive charge is transmitted to the small cloud particles (as they rebound from the graupel), which are then carried by updrafts to the upper regions of the cell (WALLACE; HOBBS, 2006). See figure 2.2.

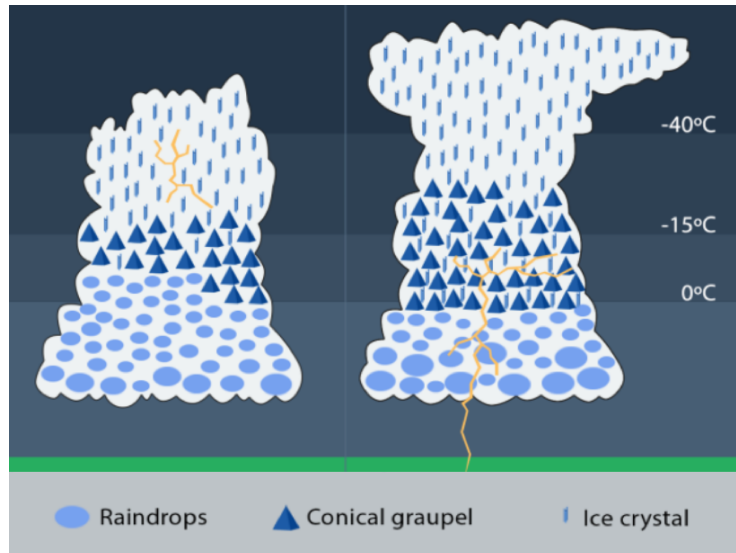


Figure 2.2 - The last 2 lightning *time steps* during the evolution of a simple thunderstorm, from **(left)** the first lighting flash within the cloud itself or *1IC*, to **(right)** the first lighting flash between the cloud and the ground or *1CG*. In the cloud, the conical graupel and the small particles (ice crystal, raindrops).

Source: Adpated from Mattos et al. (2017).

## 2.2 Nowcasting and very short-range forecasts of thunderstorms

The importance of forecasting thunderstorms and lightning activity is unquestionable because these are known threats to human life, to property and a variety of activities connected with industry, transportation, agriculture, etc. Thus, Numerical Weather Prediction (NWP) models are employed to produce short and medium range forecasts, but to have nowcasting and very short-range forecasts of thunderstorms, other tools should be developed (KARAGIANNIDIS et al., 2016), such as the present study's conceptual model of thunderstorm detection.

According to the *World Meteorological Organization (WMO)*: Nowcasting comprises a detailed description of the current weather along forecasts obtained by extrapolation of radar echoes, satellite imagery of clouds and/or lightning location for a period of 0 to 6 hours, while a very short-range weather forecasting is for a period of 0 to 12 hours. In this time range it is possible to forecast small features such

as individual storms with reasonable accuracy, using the latest radar, satellite and observational data to make analysis of small-scale features present in small area of study such as a city and obtain an accurate forecast for the following few hours.

Even though in the past, the accuracy of the data extrapolation has been characterized for a low skill in the 0-6 hours time interval (BROWNING; COLLIER, 1989; WILSON, 2003; WILSON et al., 1998; MASS et al., 2011; PIERCE et al., 2012), this premise leads the way to a continuous development of research, experiments and tools in warning the public of high-impact weather including thunderstorms, which causes lightning strikes, destructive winds and floods. Therefore, the *WMO* states that the strength of these tools lies in the fact that can provide location-specific forecasts of thunderstorms initiation growth, movement and dissipation, which allows for specific preparation for a certain weather event by people in a specific location.

As some examples of the continuous development of very short-range nowcasts and nowcasting of thunderstorms: since 1985 in North America, the National Center for Atmospheric Research under the sponsorship of the Federal Aviation Agency had conducted field experiments to develop techniques for very short-range nowcasts of thunderstorms initially based on Doppler radar observations. Also, from 2009 to 2015 in South America, the CHUVA project under the sponsorship of the Foundation for Research Support of the State of São Paulo, had conducted six field experiments over Brazil with results like the development of nowcasting techniques for thunderstorms and an improved understanding of the cloud electrification processes in the tropics and subtropics based on radar, satellite and observational measurement strategies to be described in chapter 3 (WILSON; MUELLER, 1993; MACHADO et al., 2014).

### 2.2.1 Techniques for nowcasting and very short-range nowcasts

In nowcasting and very short-range nowcasts of thunderstorms, the radar's time-space usage and contribution increases with decreasing scales. The polarization transmitted and received by the radar can be employed to improve our awareness of meteorological targets. Rinehart (1997), asserts about the capability of polarization techniques to determine the sphericity of raindrops, the orientation of ice crystals in the atmosphere, the presence and characteristics of hail, to detect the presence of graupel, and to improve rainfall measurements.

Although the use of polarimetric data is a relatively unexplored topic in the present study, some of the dual-polarization radar measurable benefits are as follows: (i) can upgrade the accuracy of the estimates of amounts of precipitation; (ii)

can tell the difference between very heavy rain and hail, which will improve flash flood watches and warnings; *(iii)* can discriminate precipitating events into high 3D spatial-temporal resolution; and *(iv)* can reduce the effects of non-weather scatterers on radar data displays (WOODARD et al., 2012; MEDINA; MACHADO, 2017) <http://www.nssl.noaa.gov/education/svrwx101/thunderstorms/>.

Other non-traditional data usage explored in the present study are the geostationary satellite’s infrared imagery and lightning data that allow the detection of thunderstorms with increasing scales. Once the lightning producing storm system initiates, monitoring its features within the electrification lifecycle is crucial to minimize the related damage via increasing warning lead times, so the plausibility of estimation of convective and electrification processes using radar, lightning and satellite data has drawn the attention of the scientific community (MATTHEE; MECIKALSKI, 2013; NETO et al., 2016; KARAGIANNIDIS et al., 2016).

Using non-traditional data for thunderstorm detection has also some limitations like the poor relationship between current cloud motions viewed by satellite and future radar echo location, or the poor correlation between clouds and radar-detected precipitation, among other problems indicated by Mecikalski and Bedka (2006), that is why multi-channel satellite applications are in continual development as shown in the present study and follows below.

### 2.2.1.1 Multi-channel satellite applications

The satellite-based analysis of growing cumulus clouds began with the Applications Technology Satellites (*ATS*)*I – V* from the mid-1960s to early 1970s and proceeds with the imaging capabilities of meteorological satellites like the Geostationary Operational Environmental Satellite-R *GOES-16* launched in 2016 and the Meteosat Third Generation (*MTG*) Satellite to be launched in 2020. Essentially, the monitoring of thunderstorms using different infrared (*IR*) bands and combinations between them; here referred as *multi-channel* analysis, has demonstrated ability to depict and increase understanding of the physical properties of convective cloud-tops including temperature, pressure, height, particle effective radius, glaciation and other features like cold-U/V shape, etc. (SCHMETZ et al., 1997; MECIKALSKI; BEDKA, 2006; ROSENFELD et al., 2008; MATTHEE; MECIKALSKI, 2013).

One problem is that traditional meteorological satellites instruments only observe the uppermost cloud tops of the thunderstorms, revealing no information about the internal structure. However, taking advantage of the high temporal sampling of the

SEVIRI instrument on the MSG (Meteosat Second Generation) and a subset of four bands combinations or *interest fields* calculated from five *IR* channels (6.2, 7.3, 8.7, 10.8 and 12.0  $\mu m$ ), important measurements of the cloud processes can be provided for our study (SETVÁK et al., 2008; NETO et al., 2016).

Some relevant multi-channel satellite applications for the deep convective cloud processes characterization are outlined as follows: first, the combination of water vapor (*WV*) and *IR* channels showed to be important when deep convective clouds are viewed because of the differences between *WV* and *IR* absorption characteristics. In fact, using global analyses of satellite observations, Ackerman (1996) and Schmetz et al. (1997) described that the equivalent brightness temperature in the *WV* channel can be larger than the *IR* channel, so the existence of negative brightness temperatures differences between *IR* and *WV* channels can be observed over high-level clouds, or clouds containing active deep convection; also the existence of positive differences between *WV* and *IR* brightness temperature are only possible when deep convective clouds penetrate in the tropopause due to the *WV* channel's strong absorption (MACHADO et al., 2009).

Second, Setvák and Doswell (1991) reported observations of deep convection storms based on 10.3 and 11.3  $\mu m$  channels. Moreover, in accordance with Machado et al. (1992), Machado et al. (1998) and others, the infrared images between 10.5 and 12.5  $\mu m$  channels; primarily sensitive to radiation from earth's surface and clouds alongside a relatively small atmospheric absorption, had been used to understand the behavior of the clouds containing active deep convection. Since these deep convective clouds penetrate in the tropopause, the conditions corresponding an altitude of about 6–9 *Km* and the brightness temperatures values between 245 and 265 *K* at latitudes equatorward of  $> 45^\circ$ , identify the high-level clouds of interest. Additionally, Vila et al. (2008) developed an algorithm based on the brightness temperature threshold of 235 *K* for tracking the physical attributes of mesoscale convective systems using the 10.8  $\mu m$  channel images covering the southeastern of South America. These considerations restrict our inspection of *interest fields* in 3.3.4.2.

Third, Strabala and Ackerman (1994) presented a trispectral combination of observations at 8, 11 and 12  $\mu m$  bands to understand clouds properties; where the absorption coefficient for ice increases more between 8 and 11  $\mu m$  than between 11 and 12  $\mu m$ , while for water the reverse is true. Later, including combinations of *WV* and *IR* channels and this trispectral technique, Mecikalski et al. (2010) analyzed the properties of growing cumulus prior of convective initiation in Europe, using *MSG*

*IR* combinations to infer three physical attributes as the in-cloud updraft (an inferred physical processes), cloud depth (the height of the updraft) and the cloud-top glaciation (and inferred microphysical processes).

Table 2.1 presents 21 channel combinations with corresponding mean and critical values for a large sample size observed in Europe, involving events of manually observing towering cumuli that evolved over 3 successive 15min images into a large cumulus cloud (cumulus congestus and cumulonimbus) or a cloud that clearly possessed a new anvil (MECIKALSKI et al., 2010). Here, the combinations of *time trends* (15min or 30min) evaluate various *IR* cloud properties in time, but it will not be examined in our study because it may not occur simultaneously with the *time steps* considered for our large sample detailed later.

Although our study have analyzed growing cumulus prior of convective and lightning initiation using satellite data, the corresponding mean values of convective processes will differ from table 2.1 due to the thunderstorm lifecycle’s dissimilarity, but the main statistical signals may be well represented in the general analysis.

### **Integrating satellite and radar and/or lightning, and/or algorithms**

Some relevant applications linking observations from geostationary satellite and ground-based radar and/or lightning, and/or algorithms for the characterization of convective processes can be outlined as follows: first, a research series from 2006 to 2016 starting with Mecikalski and Bedka (2006) and Mecikalski et al. (2008), pursued the goal of validating, optimizing and obtaining a more quantitative understanding of convective initiation algorithm, hereinafter MB06, in a extension of studies that capitalized on information provided for 0-1 *h* forecasting through the real-time monitoring of cloud-top properties for moving cumulus clouds. These techniques isolate cumulus convection in *GOES* imagery using the visible (*VIS*) and *IR* fields, and data set of the WSR-88D radar network.

Subsequently, Rosenfeld et al. (2008) provided a conceptual model for detection of the intensity of convective storms by using retrieved micro-structure from geostationary satellites, based on the retrieved vertical profiles of cloud-particle effective radius and thermodynamic phase. Also, a correlation between the temperature of cumulus cloud’s top and the particle effective radius had been demonstrated as function of aerosols contents and updraft strength, developing diagrams of cloud-top temperature versus particle effective radius as a function of the altitude.

Table 2.1 - Means and std dev values of *interest fields* for 123 growing cumulus prior of convective and lightning initiation events observed over Europe. These 123 events involved observing towering cumuli that evolved over three successive 15-min images into a large cumulus cloud or a cloud with a new anvil. The trispectral *interest field* is  $(8.7 - 10.8) - (10.8 - 12.0) \mu m$ .

Category/Rank	Interest fields	Mean ( $K$ )	Std dev ( $K$ )
Cloud depth			
1	$6.2 - 10.8 \mu m$	-14.6	11.27
2	$6.2 - 7.3 \mu m$	-6.6	5.94
3	$10.8 - \mu m T_B$	242.5	16.79
4	$7.3 - 13.4 \mu m$	5.4	4.42
5	$6.2 - 9.7 \mu m$	-8.4	3.40
6	$8.7 - 12.0 \mu m$	0.3	1.92
Cloud-top glaciation			
1	15min trispectral	0.7	2.02
2	trispectral	-0.7	1.94
3	15min $(8.7 - 10.8) \mu m$	0.5	1.47
4	$8.7 - 10.8 \mu m$	-0.1	1.55
5	15min $(12.0 - 10.8) \mu m$	0.2	1.05
6	15min $(3.9 - 10.8) \mu m$	0.3	0.24
7	$12.0 - 10.8 \mu m$	-0.5	1.15
Updraft strength			
1	30min $(6.2 - 7.3) \mu m$	7.2	4.92
2	15min $10.8 - \mu m T_B$	-12.1	9.44
3	30min $10.8 - \mu m T_B$	-20.4	13.54
4	15min $(6.2 - 7.3) \mu m$	4.3	3.58
5	30min $(9.7 - 13.4) \mu m$	4.9	4.31
6	30min $(6.2 - 10.8) \mu m$	14.5	8.78
7	15min $(6.2 - 12.0) \mu m$	8.0	6.32
8	15min $(7.3 - 9.7) \mu m$	-3.3	4.02

Source: Adapted from Mecikalski et al. (2010).

Later, Mecikalski et al. (2016) pursued the goal of evaluating a combined method from (MECIKALSKI; BEDKA, 2006), (ROSENFELD et al., 2008) and others for predicting the initiation and near-term intensity of convective storms, forming a model to predict in advance the initiation of locally intense or severe convective storms over the European territory. Although these previous studies can be used to predict convective processes, the corresponding physical attributes are related to the MB06 critical values and micro-structure information from satellites not included in our study; which is focusing in convective processes but also in electrification processes of thunderstorms over South American territory.

Again, Senf et al. (2015) identified that the rapid cooling of cloud-tops can be seen in the thermal radiation of the growing clouds which covers Germany and parts of Europe, and considering this cloud-top cooling as a measure of vertical growth, it had been incorporated into satellite-based convection initiation algorithms providing an important time of advance before storm initiation. That research had focused on the growth phase of the thunderstorm with regard to cloud-top properties/cooling rates and their changes like *IR* brightness temperature, however, our study have also been concentrated on electrification processes of thunderstorms over South America.

Second, Williams et al. (1998), Williams et al. (1999), Gatlin and Goodman (2010), Chronis et al. (2015) supported the concept that the most obvious and systematic characteristic of thunderstorms is the abrupt increase in flash rate in advance of the severe weather manifestation at ground. Consequently, Machado et al. (2009) developed a scheme that estimates the probability of occurrence of cloud-to-ground discharge over all the continental region of South America, using *WV* and *IR* *GOES* imagery with cloud-to-ground discharge data from the *RINDAT* Brazilian network for determining *WV-IR* critical values (greater than  $-15\text{ K}$ ) of large potential for cloud-to-ground discharge activity to be included in our inspection of *interest fields*.

Third, Mattos and Machado (2011) examined the properties of MSCs in Brazil using data from *GOES* infrared, *NOAA-18* and *TRMM* microwave channels with cloud-to-ground discharge data from the *BrasilDAT* Brazilian network to demonstrate the potential use of thermodynamic, dynamic and microphysical characteristics for analyzing thunderstorm severity and nowcasting electrical activity. The lifecycle of a thunderstorm had been considered as initiation ( $t_0$ ) - the first time the system was detected; intermediary ( $t_1$ ) - the intermediate stage between initiation and maturation; maturation ( $t_2$ ) - maximum size; intermediary ( $t_3$ ) - the intermediate stage

between maturation and dissipation and dissipation ( $t4$ ). However, our study have considered the lifecycle of a thunderstorm in lightning *time steps* defined by [Mattos et al. \(2016\)](#) as *1Echo* ( $t0$ ) - the first echo with any value of reflectivity above the reflectivity noise level; *Int* ( $t1$ ) - intermediate stage between first reflectivity echo and first intra-cloud lightning flash, *1IC* ( $t2$ ) - the first intra-cloud lightning flash and *1CG* ( $t3$ ) - the first cloud-to-ground lightning flash.

Fourth, [Matthee and Mecikalski \(2013\)](#) studied the relation between thermal storm properties and electrical activity in equatorial Africa using measurements from a S-band dual-polarimetric radar, a Very Low Frequency (VLF) lightning network and the *MSG* satellite. There, 8 of 10 *IR interest fields* describing three physical attributes as the updraft strength, cloud depth and glaciation, conferred dissimilarity between non-lightning and lightning-producing convective clouds. Moreover, a list classified by physical attribute and corresponding critical values for convective clouds are summarized in table 2.2.

Table 2.2 - Critical values (*indicate occurrence of ice clouds*) by category . The trispectral *interest field* is  $(8.7 - 10.8) - (10.8 - 12.0) \mu m$ . Multi-channel-differencing *time trends* evaluate various *IR* cloud properties in time.

<b>Interest fields</b>	<b>Category</b>	<b>Critical Value</b>
6.2 – 10.8 $\mu m$	Cloud depth	Differences toward $0^\circ$
6.2 – 7.3 $\mu m$	Cloud depth	From $-30^\circ$ to $-10^\circ$
8.7 – 10.8 $\mu m$	Cloud-top glaciation	$> 0^\circ$
15min (8.7 – 10.8) $\mu m$	Cloud-top glaciation	$> 0^\circ$
trispectral	Cloud-top glaciation	Becoming $> 0^\circ$
15min trispectral	Cloud-top glaciation	Positive trends
15min (6.2 – 7.3) $\mu m$	Updraft strength	Positive trends
30min (6.2 – 7.3) $\mu m$	Updraft strength	Positive trends
15min 10.8 – $\mu m T_B$	Updraft strength	$< -4^\circ$
30min 10.8 – $\mu m T_B$	Updraft strength	$< 15min 10.8 \mu m$

Source: Adapted from [Matthee and Mecikalski \(2013\)](#).

Fifth, [Mecikalski et al. \(2013\)](#) identified relationships between cloud-top *IR* observations together with radar network observations using accepted relationships on how developing lightning events appear in each dataset separately. For this, 3 main datasets were employed including observations from the Lightning Mapping Array (LMA) network and 4D Lighting Surveillance System, WST-88D Z within the National Mosaic and Multisensor QPE radar dataset and *GOES-12 IR* fields.

In light of the cloud-top *IR* fields and focusing on physical processes while comparing lightning-producing storms, the results of [Mecikalski et al. \(2013\)](#) provided significant information of cloud-top cooling rates in the  $10.8 - \mu m$  channel and in its time trends toward understanding the processes related to lightning initiation occurring within cases studies over the U.S. As the [Mecikalski et al. \(2013\)](#)'s data with temporal resolution of 15 or 30 min do not necessarily coincide with the lightning *time steps* of our thunderstorms, the time trends for the *IR* fields have not been employed in our study.

For our study, the images were obtained in the *MSG* satellite projection and re-projected to a rectangular projection covering the CHUVA-Vale surveillance region, with temporal resolution of 15 min and spatial resolution of 4 *km*. Following this, two main datasets were employed, comprising the observations from the *MSG IR* fields, and the co-located radar-lightning dataset of [Mattos et al. \(2016\)](#); including observations from the the Brazilian Lightning Detection Network (BrasilDAT) and the Lightning Mapping Array (LMA), and the XPOL radar with temporal resolution of 6 *min*. Also, it has been assumed that the difference between the temporal resolutions of the satellite and the radar will not significantly affect the understanding of the processes related to lightning initiation occurring within our *compact thunderstorms* selected as cases studies.

Sixth, [Karagiannidis et al. \(2016\)](#) presented a lightning activity nowcasting tool for the Greek territory, employing only *WV* and *IR MSG IR* imagery with cloud-to-ground discharge data from a real-time Very Low Frequency (VLF) lightning detection system; based on a synthesis of the existing methodologies on nowcasting convective initiation (CI) and lightning initiation (LI). Preceding this, our study will be preferentially include the relationship developed by [Machado et al. \(2009\)](#) between cloud-to-ground discharge and cumulus clouds over South America.

Conclusively, [Mattos et al. \(2016\)](#) and [Williams et al. \(2016\)](#) found isolated thunders-torms on radar as they appear, and whose lightning activity was well documented with special detection systems. Then, within a minimum scale (radar echo  $> 20$  *dBZ*) for lightning initiation ( $> 3$  *Km* in radius), they defined the electrification lifecycle in lightning *time steps* and presented the cloud microphysics relationship as function of the three-dimensional total lightning density for a large sample size (46 cases) of incipient thunderstorms; specifically using a X-band dual polarimetric radar and multiple lightning detection networks during a field campaign in the subtropical region of southeast Brazil.

In addition, these authors' findings for the incipient thunderstorms showed noticeable contrast with the mesoscale convective systems in previous studies because of the behavior of cloud-to-ground flashes, that is, the peak current of initial cloud-to-ground flashes are substantially smaller, only half as large as return stroke peak currents in general (WILLIAMS et al., 2016). Subsequently, our study have joined together their radar and lightning co-located data set along with the observations from *MSG* satellite, focusing on the convective and electrification processes of incipient thunderstorms as means to develop a detection tool for subtropical regions.

Finally, although it is not directly related with the present study, is worth mentioning the recent work of Stolz et al. (2017) integrating satellite, radar and lightning data, and also algorithms in which statistical relationships for tropical convective features has been investigated within various geographic areas as means to make comparisons between the aerosol (CCN) and thermodynamic (NCAPE and WCD) contributions to variations of these convective features.

### **Integrating numerical weather prediction to nowcasting tools**

Although our study does not contemplate the integration of numerical weather prediction (NWP) models to develop a nowcasting tool, a brief review of these applications follows below considering the demand for high-resolution analyses as means of having a better representation of the dominating mesoscale convective systems (MCSs) in the subtropical central and southern regions of South America (ZIPSER et al., 2006; MULLER et al., 2016).

Due to the socioeconomic relevance of the La Plata basin, this region between 14 and 27 ° S has been the subject of diverse weather forecasting and hydro-climate studies based in numerical model simulations during the last years (BERBERY; COLLINI, 2000; SELUCHI; CHOU, 2001; SÁNCHEZ et al., 2015; MULLER et al., 2016).

Also in the South American region between 20 and 40 °, the methodology presented by Neto et al. (2016) was based in a *MSG* multi-channel approach together with tropopause temperature information provided by a numerical model in order to stratify cloud shield and highlight regions of different convective characteristics and demonstrating that this cloud shield stratification technique showed better ability to evaluate strong convection when compared with simpler satellite-based analysis.

Therefore, the following emphasis not only in South America but worldwide, needs to be placed on extending the nowcasting algorithms by integrating satellite, radar and/or lightning, and numerical weather prediction models to provide forecasts with increased lead-time to high-impact events such as MCSs. The success of these numerical weather prediction models will depend on more than the quality of estimating or retrieving the state of the atmosphere in some domain given corresponding observations, nevertheless, a clear progress has been achieved in NWP with the assimilation of nontraditional data sources such as observations from satellites, radars and/or lightning (WEYGANDT; SHAPIRO A.AND DROEGEMEIER, 2002; SNYDER; ZHANG, 2003; MECIKALSKI et al., 2016).

Besides, Jones et al. (2013) stated that observations from satellites provide information on cloud properties on similar horizontal and temporal scales as radar data, but with greater sensitivity to the non- or pre-convective clouds that may be present. Even though many uncertainties remain as to the best cloud properties and assimilation techniques to use when attempting to correctly characterize clouds within high-resolution NWP model, by assimilating *GOES* imager cloud property retrievals into a convective-scale model (ARW-WRF version 3.3.1) using an ensemble Kalman filter (EnKF) approach, this research found an improved characterization of clouds and convection leading to an increase model skill.

In the words of Jones et al. (2014), assimilating both satellite and radar observations generally produced the most accurate cloud and thermodynamic analyses, indicating that both are providing unique information to the model, and consequently, producing accurate forecasts of high-impact weather events. For example, assimilating satellite  $6.2 \mu m$  brightness temperature, simulated radar reflectivity and radial velocity observations for a cold-season case, reduced errors for humidity and cloud hydrometeor variables observed at all atmospheric levels with Doppler radial velocity information also resulting in a reduction in wind velocity errors.

Further improvements in futures studies indicated by Jones et al. (2014) are related to the results based on a limited sample of ordinary single cell convection, then, an expansion of the data set including a larger sample size of different meteorological and convective situations should give more robust results and reduce any possible bias error associate with a small sample set.

## 2.2.2 Problem of parallax in satellite meteorology

The parallax error occurs as result of the viewing angle geometry and the projection of the image data onto a  $2D$  plane for display as an image. Figure 2.3(a) shows the top of a cloud displaced to a point away from the sub-satellite point. This error increases further from the sub-satellite point but can be corrected knowing the height of the cloud, the satellite position, and the coordinates of the cloud. For example, figure 2.3(b) shows a surface lake viewed obliquely from a distant satellite, so this surface feature is far from the sub-satellite point. If a tall cloud develops between the surface lake and the observing satellite, the satellite still interpret the information as coming from the surface, but the tall cloud is displaced towards the sub-satellite point. Another consequence of the viewing angle geometry, is that the temperature of the cloud will reflect the temperature of the side of the cloud that the satellite is viewing; the colder cloud top will be in a different pixel (KIDDER; HAAR, 1995).

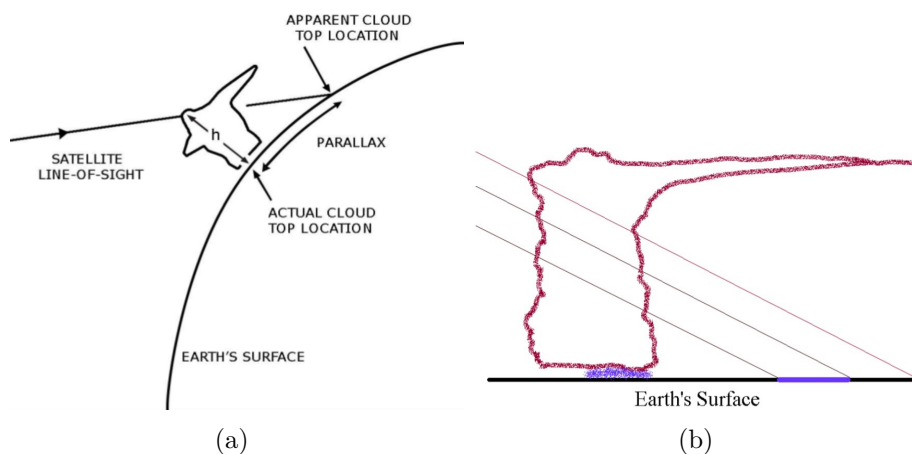


Figure 2.3 - Parallax in satellite meteorology: a) Displacement due to cloud height, after Weiss (1978); b) The image shows the lake (lilac surface) viewed obliquely from a distant satellite, so the surface is far from the sub-satellite point (*the sub-satellite point is on the Earth surface, directly beneath the satellite*). Source: (RADOVÁ; SEIDL, 2008), <http://cimss.ssec.wisc.edu/goes/blog>

Another example from the *CIMSS Satellite Blog* during April 2006: Figure 2.4(a) shows strong convection over northern Wisconsin (USA). In figure 2.4(b), the enhanced infrared image can be used to infer the height of the cloud. Also, the radar image for the same time in figure 2.4(c), indicates a line of convection displaced to the south of convection. On this example without a correction of the parallax error, there is a very cold cloud top on satellite and the cloud top is far from the

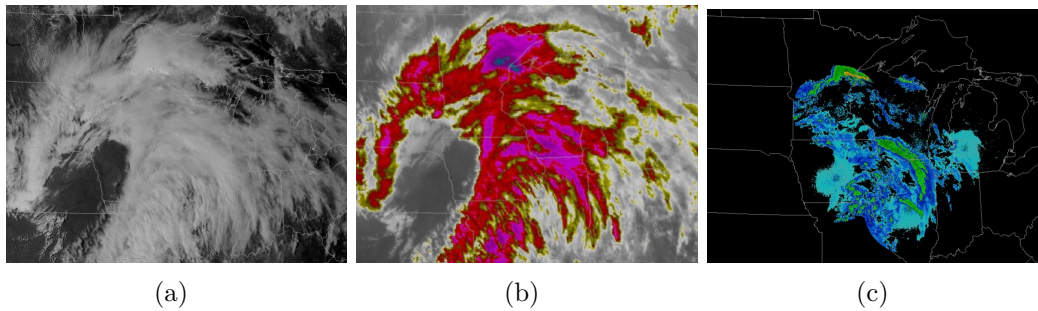


Figure 2.4 - An example from April 2006 in the United States of America: a) Satellite image shows strong convection over northern of Wisconsin State, b) Satellite enhanced infrared image for the same time can be used for infer the height of the cloud, c) Radar image for the same time and area shows a line of convection displaced to the south of convection.

Source: University of Wisconsin-Madison/Space and Engineering Center  
<http://cimss.ssec.wisc.edu/goes/blog/archives/217>

sub-satellite point, hence, it is very likely that the position of the cloud feature over the surface is closer to the sub-satellite point than is indicated in the image (<http://cimss.ssec.wisc.edu/goes/blog/archives/217>).

Moreover, Lábó et al. (2007) showed that parallax error can be efficiently corrected using the  $10.8 \mu m$  channel data and *SEVIRI* cloud-top heights obtained from the *SAFNWC/MSG* software as its base, and presenting cases studies with well preserved cloudiness when satellite images are corrected throughout these methods.

In addition, Radová and Seidl (2008) presents a case study of parallax correction comparing radar and satellite data on a cold-ring shaped storm in 2006 above Australia using observations from the *MSG* satellite and Hydro-meteorological Prague Institute radar. This work presents two possible ways of correction enumerated as follows: (i) each cloud pixel in satellite imagery shifted by a corresponding parallax value; for which is the cloud-top heights must be known, and the chosen possibility (ii) based on a transformation of data that are to be compared with satellite imagery (or radar data) into the geostationary projection.

Thus, figure 2.5 shows a cold-ring storm in color-enhanced image in the  $10.8 \mu m$  channel with radar data superimposed after the parallax correction. The location of the storm's overshooting top without the parallax correction is marked by the black curve to demonstrate that parallax correction is essential for proper interpretation of features occurring in satellite imagery depicting high clouds and particularly when comparing satellite and radar data. Also using the graphic scale in this figure, is

possible to quantify the approximate displacement between the overshooting top with and without the parallax correction as less than 25 *Km*.

Conclusively, a free-access functionality for parallax correction developed by *EU-METSAT*, the state members and the European Severe Storms Laboratory (*ESSL*) within the *Convection Working Group Blog*, involves parallax error calculation on each pixel employing as main input data: the height of the satellite, latitude and longitude of the sub-satellite point, and height, latitude and longitude of the cloud. This tool has been implemented in 3.3.1 after the cloud height calculations.

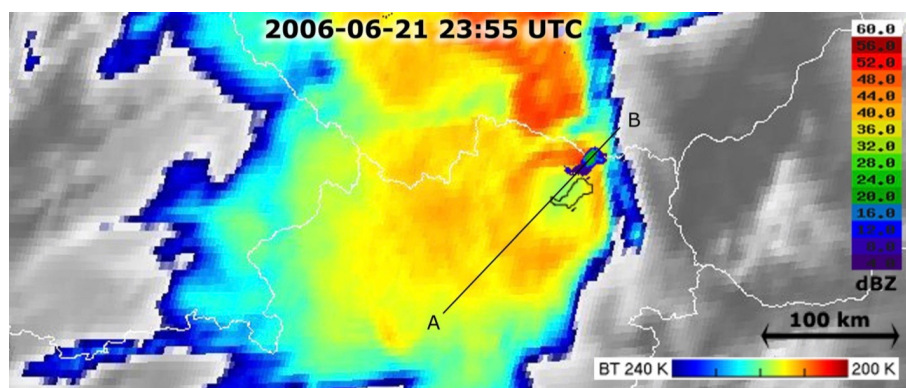


Figure 2.5 - Cold-ring shaped storm above Austria (21 June 2006, 23:55 UTC) in color enhanced image in the  $10.8 \mu m$  channel with radar data (CAPPI 15 km; 22 June 2006, 00:00 UTC) superimposed after the parallax correction. The location of the storm's overshooting top without the parallax correction is marked by the black curve. The line A-B marks an examined cross-section. Source: Radová and Seidl (2008).

### 2.2.2.1 Cloud height calculation

As stated by Nieman et al. (1993), two possibilities can be considered for the estimation of cloud height. First, the infrared window (*IRW*) method for opaque clouds, estimates the height of the clouds by comparing the brightness temperature of the cloud-tops with air temperature soundings. Second, the  $H_2O - IRW$  intercept method for semi-transparent clouds, put forward a correction of the cloud-top brightness temperature before using the *IRW* method.

The  $H_2O - IRW$  intercept method developed by Szejwach (1982), makes the fundamental assumption of a linear relationship between radiances in two spectral bands observing a single cloud layer: considers the radiances in the  $H_2O$  ( $6.7 \mu m$ ) and *IRW* ( $11.2 \mu m$ ) spectral bands at clear-sky (surface) and opaque clouds (cloud), to

generate a line connecting the centers of scattered radiance values in both spectral bands. The intersection of this line with the radiative curve (computed using a radiative transfer model), indicates the radiance correction of a semi-transparent cloud, that is, the cloud-top brightness temperature is extracted from the cloud radiance intersection (see figure 2.6).

Within the *EUMETSAT* frame, the *SAFNWC* software package (V1.0 or V1.2) has been developed to derive products useful for nowcasting purposed from *MSG* imagery and also contemplates the cloud-top heights product (*SAFNWC/MSG CTH*) for respectively opaque and semi-transparent clouds. The calculations of semi-transparent cloud-top heights can be done using the  $H_2O - IRW$  intercept method; a software option based on a radiance histogram analysis, and showing an underestimation of 1 *Km* approximately as compared with other software option like the radiance rationing method (DALOZE; HAEFFELIN, 2005; DERRIEN et al., 2005).

The first software option may be used in our study, but a functionality based on the  $H_2O - IRW$  intercept method provided by the Satellite Division & Environmental Systems Group (DSA-CPTEC/INPE) has preferentially been implemented in 3.3.1 considering its appropriate accuracy of calculations and effective level of support.

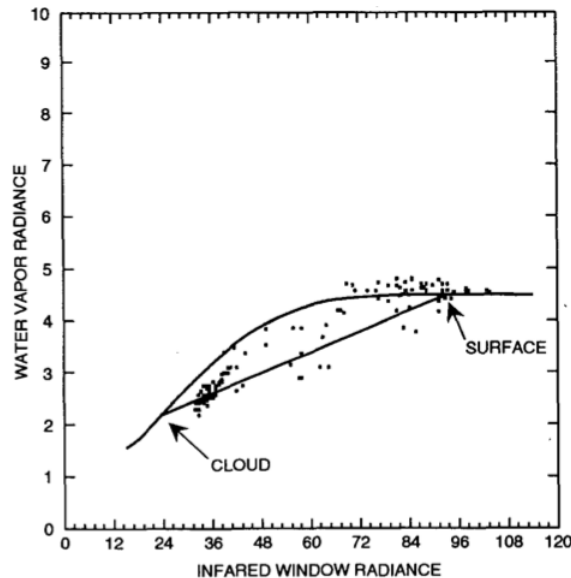


Figure 2.6 - Measures radiances ( $mW m^2 sr^{-1} cm$ ) for fields of view partially filled with clouds. The line connects the centers of scattered radiance values in both spectral bands, and the curve represents the calculations of radiance for both spectral channels for semi-transparent clouds and surface. At the bottom, the intersection indicates the radiance correction of a semi-transparent cloud. Source: Nieman et al. (1993).



### 3 Data and Methods

The present chapter introduces the CHUVA project and CHUVA-Vale field campaign in section 3.1, describes the data set for this work in section 3.2, and examines the methods to build a conceptual model for thunderstorm detection based on brightness temperature histograms and thresholds analysis in section 3.3.

#### 3.1 The CHUVA project and the CHUVA-Vale field campaign

The CHUVA project —Cloud Processes of tHe Main Precipitation Systems in Brazil: A ContribUtion to Cloud ResolVing Modeling and to the GlobAl Precipitation Measurement (GPM)— has conducted six field campaigns in Brazil between 2010 and 2014. The objective of these campaigns was to understand the cloud processes of the various precipitation regimes of Brazil and collect detailed information in support of the GPM program (MACHADO et al., 2014; ALBRECHT et al., 2014).

Figure 3.1 illustrates on its left side, the CHUVA field campaigns and main precipitation regimes over Brazil; and on its right side, the reference measurement strategy adopted during these field campaigns. See the Vale do Paraíba campaign indicated in *red circles*. Additional description regarding all field campaigns can be found in CHUVA project website (<http://chuvaproject.cptec.inpe.br>).

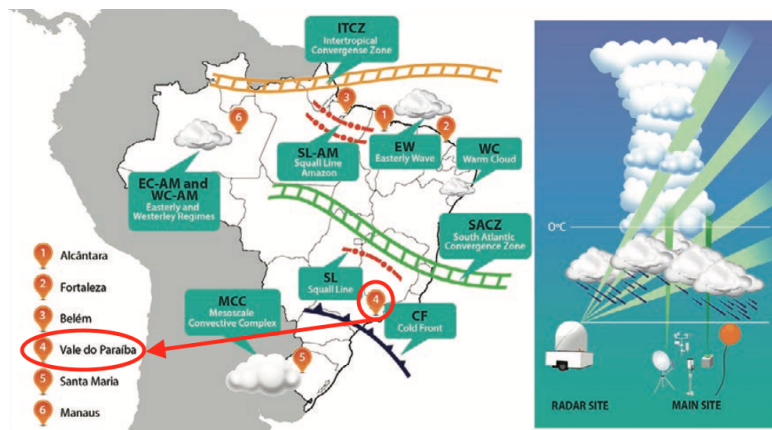


Figure 3.1 - **(left)** The CHUVA’s experimental sites and the main precipitations regimes in Brazil. The focus of our study is the Vale do Paraíba campaign in southeastern Brazil; indicated with *red circles*. **(right)** The CHUVA’s reference measurement strategy during field campaigns along with the radar site and main site with other instruments.

Source: Machado et al. (2014).

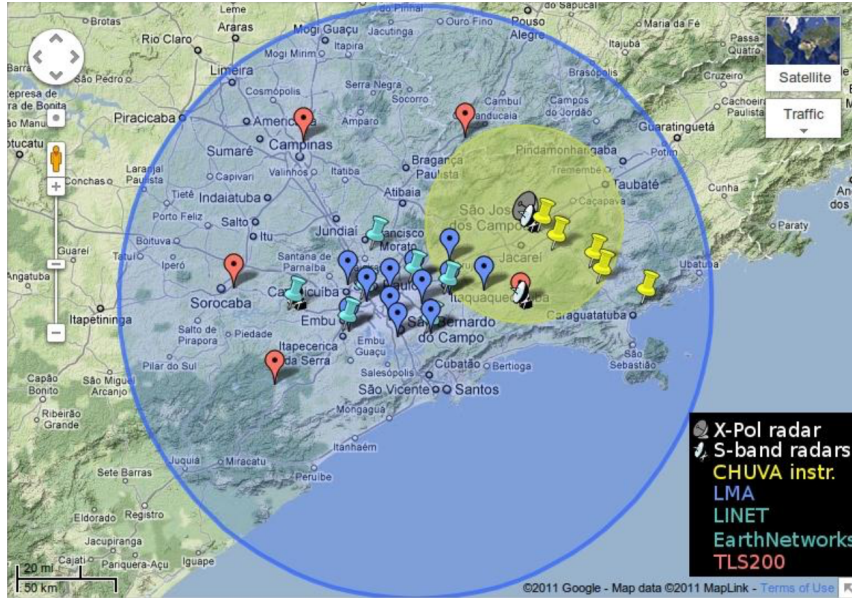


Figure 3.2 - Main site of the CHUVA-Vale field campaign. Location of the X-band radar (*grey radar*) and other S-band radars such as São Roque, FCTH and IACIT (*black/white radars*). The *yellow circle* represents the covering extent of X-band radar of 60 km. Location of the CHUVA instruments sites (*yellow stick pins*) and lightning sensors such as SPLMA (*blue stick pins*); LINET and EarthNetworks (*cyan stick pins*), and TL200 (*red flags*). The blue circle represents the area of 3-D lightning mapping of the SPLMA stations.

Source: (ALBRECHT, 2011; BLAKESLEE et al., 2013).

Our study is focused in the fourth experiment of this project: the CHUVA-Vale field campaign that took place at the Vale do Paraíba; centered around the city of São José dos Campos in southeastern Brazil during the rainy season from 01 November 2011 to 31 March 2012. The Vale do Paraíba region is located in a valley with approximately 2.4 million of urban population (<http://www.ibge.gov.br>), between the Mantiqueira and the Serra do Mar Mountains, and approximately 100 Km from the Atlantic Ocean.

The CHUVA-Vale experiment's motivation was the understanding of cloud processes that evolve when clouds transform into thunderstorms and its primary objective was to study storm electrification (MACHADO et al., 2014).

Figure 3.2 presents the Vale do Paraíba region and the location of ground instruments for studying storm electrification such as X-band radar; other S-band radars (São Roque, FCTH and IACIT). The *yellow circle* represents the covering extent of X-band radar of 60 km, while the *yellow stick pins* are CHUVA instruments sites. The location of lightning sensors such as SPLMA; LINET and EarthNetworks, and

TL200 are indicated by the *blue, cyan and red stick pins*, respectively. The blue circle represents the area of 3-D lightning mapping of the SPLMA stations at a maximum distance of 150 *Km*. These data set are available in CHUVA project website (<http://chuvaproject.cptec.inpe.br>).

The Vale do Paraíba campaign was a collaborative effort between CHUVA Project, GOES-R/MTG satellite development programs, private companies committed to lightning detection and local centers responsible for risk reduction (MACHADO, 2012; ALBRECHT et al., 2014). Also as presented by Machado et al. (2014), several intense thunderstorms and some severe weather events were reported during this campaign, including a downburst and cases of hailstorms.

## 3.2 Data

For this work, the data of CHUVA-Vale field campaign from 01 November 2011 to 31 March 2012, is itemized as follows: (i) Satellite data (3.2.1); (ii) Radar data (3.2.2); (iii) Lightning data (3.2.3); (iv) Thunderstorm cases studies (3.2.4) and (v) Co-located radar-lightning data set (3.2.5).

### 3.2.1 Meteorological Satellite (Meteosat) Data

Meteorological satellite data can be used to describe the physical attributes occurring inside incipient developing of thunderstorms throughout various channels combinations or *interest fields*. Along with the Meteosat geostationary satellite images (infrared channels) covering the CHUVA-Vale field campaign region, these physical attributes and in-cloud processes have been considered as the following: in-cloud updraft (an inferred physical processes), cloud depth (the height of the updraft), and cloud-top glaciation (and inferred microphysical processes) (ROSENFELD et al., 2008; MECIKALSKI et al., 2010).

In order to avoid solar zenith angles correction and enable the analysis of channels combinations during night-time, also considering that clouds are better observed through infrared (*IR*) and water vapor (*WV*) images in tandem (KIDDER; HAAR, 1995), the interest fields calculated from SEVIRI *IR* channels have been selected for this study. Consequently, the main information are calibrated level 1.5 *IR* data from the SEVIRI instrument on the Meteosat Second Generation (MSG) operated by *EUMETSAT* in its nominal position over equator at 0° longitude (level 1.5 *IR* data includes calibrated radiances, which have been rectified to a fixed grid after geolocation; <https://www.eumetsat.int/website/home/Data/>

Table 3.1 - Summary of SEVIRI spectral channels from MSG geostationary satellite

No.	Channel	Central wavelength ( $\mu m$ )	Main gaseous absorber/Window
1	VIS 0.6 $\mu m$	0.635	Window
2	VIS 0.8 $\mu m$	0.81	Window
3	NIR 1.6 $\mu m$	1.64	Window
4	IR 3.9 $\mu m$	3.90	Window
5	<b>WV 6.2 <math>\mu m</math></b>	6.25	Water vapor
6	<b>WV 7.3 <math>\mu m</math></b>	7.35	Water vapor
7	<b>IR 8.7 <math>\mu m</math></b>	8.70	Window
8	<b>IR 9.7 <math>\mu m</math></b>	9.66	Ozone
9	<b>IR 10.8 <math>\mu m</math></b>	10.80	Window
10	<b>IR 12.0 <math>\mu m</math></b>	12.00	Window
11	<b>IR 13.4 <math>\mu m</math></b>	13.40	Carbon dioxide
12	HRV	Broad band (0.4-1.1)	Window/water vapor

Source: Adapted from (SCHMETZ et al., 2002)

[Products/Calibration/MSGCalibration/index.html](#)). These geostationary satellite data are available at 15-*min* cycle with spatial sampling distance of 3 *Km* at subsatellite point in 11 channels; are transmitted as high rate transmissions in 12 spectral SEVIRI channels summarized in table 3.1, where 8 are *IR* channels having wavelengths of 3.9, 6.2, 7.3, 8.7, 9.7, 10.8, 12.0 and 13.4  $\mu m$  (SCHMETZ et al., 2002). The pixel resolution over the CHUVA-Vale field campaign region is 4 *Km* because of the view angle. Other details about meteorological satellite data covering the field campaign region can be found in (MACHADO et al., 2014).

### 3.2.2 Radar data

Further information covering CHUVA-Vale field campaign region are the radar data integrated in volumes describing the concentration, size, phase and type of hydrometeors throughout observable standard polarimetric variables. Besides, the vertical distribution of these polarimetric variables as function of the lightning density has risen validated relationships between the early development of cumulus clouds and the first lightning production of cumulus clouds (MATTOS et al., 2016).

For this work, the radar data has taken part in the identification of cases studies as *compact thunderstorms* and in the differentiation of corresponding *lightning time steps* during each electrification life cycle as means to build a conceptual model for thunderstorm detection.

Then, considering radar data for the identification and *time step* differentiation during each electrification life cycle, the methods in Williams et al. (2016) and Mattos et al. (2016) have detected the initial development of isolated thunderstorms, or the first reflectivity echo  $1Echo (t_0)$ , by considering movies of the archived data to find initial radar echoes that evolved to thunderstorm stage as isolated convective cells. In a post-thunderstorm analysis, the first intra-cloud and cloud-to-ground lightning flashes, or  $1IC (t_2)$  and  $1CG (t_3)$ , were accumulated within each radar volume scan assigned to the appropriate thunderstorm cell considering area boundaries as constrain. Meanwhile, the intermediary *time step* or  $Int (t_1)$ , has been demarcated between  $1Echo (t_0)$  and  $1IC (t_2)$ . Other details about the *compact thunderstorms* and respective *time steps* can be found between subsections 3.2.3 and 3.2.5.

Additionally, table 3.2 summarizes characteristics of the CHUVA-Vale polarimetric X-band or XPOL radar, installed at Parque Tecnológico da Universidade do Vale do Paraíba (UNIVAP) in São José dos Campos city. The scanning strategy of  $89^\circ$  elevation with  $0.5 \mu m$  pulse length and a repetition every 6 *min*; comprised a combination of one volumetric scan (4 *min* for standard polarimetric variables observable and 13 PPI), two range height indicator (RHI) scans and one vertical scan for correction of  $Z_{DR}$  offset. More details of the radar data, its pre-processing and corresponding corrections can be found in (SCHNEEBELI et al., 2012; SAKURAGI; BISCARO, 2012; MACHADO et al., 2014; MATTOS et al., 2016).

Table 3.2 - Operating parameters of XPOL radar during the CHUVA-Vale Campaign

<b>Radar parameter</b>	<b>Characteristics</b>
Manufacturer	Selex Gematronik (Germany), Model Meteor 50DX
Transmitter	Magnetron delivering 35 <i>kW</i> per channel
Operating frequency	9.375 <i>GHz</i>
Polarization	Simultaneous horizontal and vertical transmission
Pulses	PRF 1200 and 1500 <i>Hz</i> (stagger = 5/4, all elevations)
Radial resolution	PPI 150 <i>m</i> in range and $1.0^\circ$ azimuth
Antenna	1.8 <i>m</i> diameter, $1.3^\circ$ beamwidth and 43 <i>dB</i> gain
Elevations	13 (from $1.0^\circ$ to $25.0^\circ$ )
Location Coordinates	$45.952^\circ$ W, $23.206^\circ$ S, 650 <i>msl</i>

Source: (SCHNEEBELI et al., 2012; SAKURAGI; BISCARO, 2012; MATTOS et al., 2016)

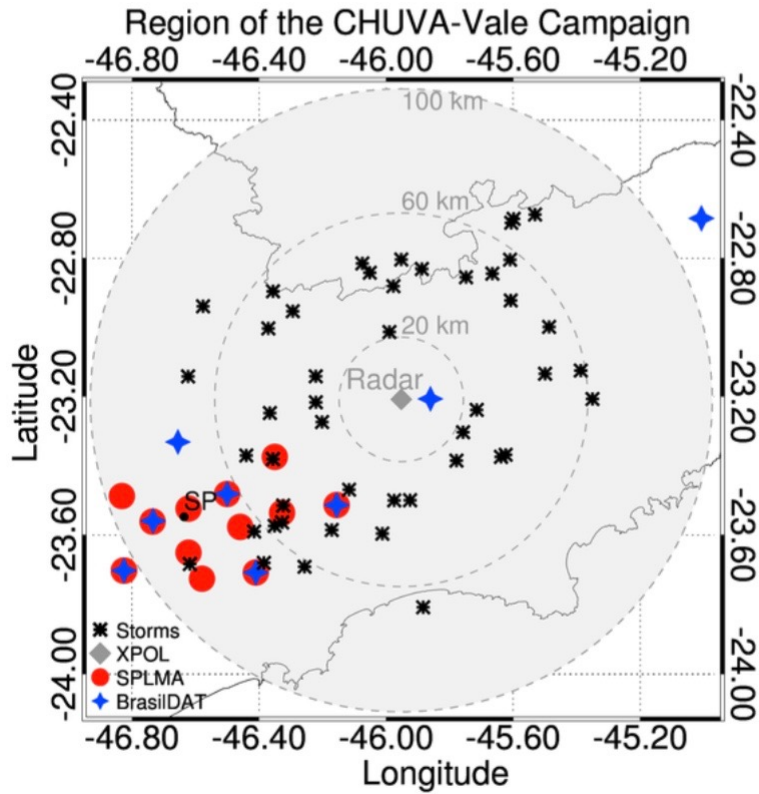


Figure 3.3 - The CHUVA-Vale field campaign region. The XPOL radar (*gray diamond*) in São José Dos Campos; distance rings (20, 60, and 100 Km) from the XPOL radar (*dashed lines*), lightning networks from BrasilDAT (*blue stars*) and SPLMA (*red filled circles*) and 46 thunderstorms at the 1CG (*t3*) (*asterisks*).

Source: (MATTOS et al., 2017).

### 3.2.3 Lightning Data

The lightning data component for the CHUVA-Vale campaign had the collaboration of partners from Brazil, U.S. and Europe. As reported in Machado et al. (2014) and Albrecht et al. (2014), the participating lightning location systems were Sferics Timing and Ranging Network (STARNET), Rede Integrada Nacional de Detecção de Descargas Atmosféricas (RINDAT), World Wide Lightning Location Network (WWLLN), Arrival Time Difference Network (ATDnet), Vaisala Global Lightning Data set 360 (GLD360) and Total Lightning Sensor (TLS200), Sistema Brasileiro de Detecção de Descargas Atmosféricas (BrasilDAT), Lightning Network (LINET), and Lightning Mapping Array (LMA). Besides, the independent lightning data set from BrasilDAT has taken part in the differentiation of *lightning time steps* for each electrification life cycle selected by Mattos et al. (2017).

The BrasilDAT system provides support for engineering, meteorological and safety activities in Brazil. For the study and corresponding validation, a total of 56 ELF-HF sensors, or Extremely Low Frequency-High Frequency sensors (1  $Hz$  - 12  $MHz$ ), covering the southeastern, south, central and part of northeastern Brazilian regions, and additional sensors deployed close to the field campaign region; were available to provide return strokes observations, including information on location, time of occurrence and polarity of the first intra-cloud and cloud-to-ground lightning flashes in developing thunderstorms (MATTOS et al., 2017).

Second, previous works have presented that LMA systems locate lightning radiation sources in three spatial dimensions time. These systems measure the arrival time of impulsive very high frequency (VHF) radiation emitted by lightning flash at several stations, and use the arrival times to locate the sources of the radiation (RISON et al., 1999). From CHUVA's perspective, the SPLMA contribution was to provide total lightning, lightning channel mapping and detailed information on the locations of cloud charge regions for the thunderstorms investigated. Thus, LMA data helped to address scientific questions as the understanding the cloud microphysics and electrification processes evolution during the cloud life cycle. For the campaign, the SPLMA network composed of 12 VHF portable stations, have provided accurate 3-D lightning mapping out to 150  $Km$  from its center; including information on time, latitude, longitude, and height for the VHF sources (BLAKESLEE et al., 2013; BAILEY et al., 2014).

The figure 3.3 presents 8 *blue stars* as sensors from the BrasilDAT network operating in VLF frequency; 12 *red circles* as the portable stations operating in VHF channels for the SPLMA network of approximately 60  $Km$  diameter with sensor spacing between 40 and 50  $Km$ , and 46 *black asterisks* as thunderstorms cases studies of the CHUVA-Vale field campaign (see subsection 3.2.4).

### 3.2.4 Thunderstorms cases studies

As mentioned before, the radar and lightning data has taken part in the identification of thunderstorms cases studies. Henceforward in accordance with Mattos et al. (2017), the term *compact thunderstorm* is referred to isolated small precipitating cells of diameter  $< 20 Km$  that have been identified in a distance between 20 and 60  $Km$  range from the radar, and have produced an intra-cloud/cloud-to-ground lightning flashes throughout the electrification life cycle. This simplification can be assumed as physical interpretation of incipient thunderstorm development and will be the basic unit to build a conceptual model for thunderstorm detection.

For the present work, each case study is a *compact thunderstorm* without additional thunderstorm obstruction between 20 and 60 *Km* range from the radar; and presents the following *demarcation* of lightning *time steps*: ( $t_0$ ) - the first radar echo with any value of reflectivity above the reflectivity noise level at any height; ( $t_1$ ) - the intermediary, ( $t_2$ ) - the first intra-cloud lightning flash and ( $t_3$ ) - the cloud-to-ground lightning flash time. Again, the figure 3.3 represents 46 *black asterisks* as the thunderstorms cases studies of CHUVA-Vale field campaign.

### 3.2.5 Co-located radar-lightning data set

Considering the radar and lightning data along with our cases studies, Williams et al. (2016) and Mattos et al. (2016) created a co-located radar-lightning data set for the electrification life cycle of each thunderstorm, that is, information on the time of occurrence, latitude and longitude of the corresponding *1Echo* ( $t_0$ ) - the first echo with any value of reflectivity above the reflectivity noise level; *Int* ( $t_1$ ) - intermediate stage between first reflectivity echo and first intra-cloud lightning flash, *1IC* ( $t_2$ ) - the first intra-cloud lightning flash and *1CG* ( $t_3$ ) - the first cloud-to-ground lightning flash time, respectively. In this work, the *demarcation* of lightning *time steps* is crucial for the thunderstorm detection conceptual model.

To achieve these *demarcations*, Williams et al. (2016) and Mattos et al. (2016) examined the XPOL radar data in the Plan Position Indicator (PPI) scan and established at first, a spatial criteria of 20 *Km* threshold (similar to precipitating cells diameter) and a temporal criteria of 0.5  $\mu s$  threshold. Second, the return stroke observations from BrasilDAT had been grouped into intra-cloud and cloud-to-ground lightning flashes. Third, these intra-cloud and cloud-to-ground lightning flashes were accumulated every 6-minutes and assigned to each thunderstorm by using the spatial criteria established (20 *Km*). Finally, to determine the lightning initiation height of these flashes, the VHF sources from SPLMA had been linked with the intra-cloud and the cloud-to-ground lightning flashes from BrasilDAT by using the same spatial-temporal criteria established. More specifications of the radar-lightning data set can be found in (MATTOS, 2015; MATTOS et al., 2016).

## 3.3 Methods

The present section examines the methods to build a conceptual model of thunderstorm detection during the electrification life cycle. For achieving this conceptual model, the figure 3.4 outlines the data set in *red* (already presented above), the methods in *yellow*; following between subsections 3.3.1 and 3.3.6, some tests in

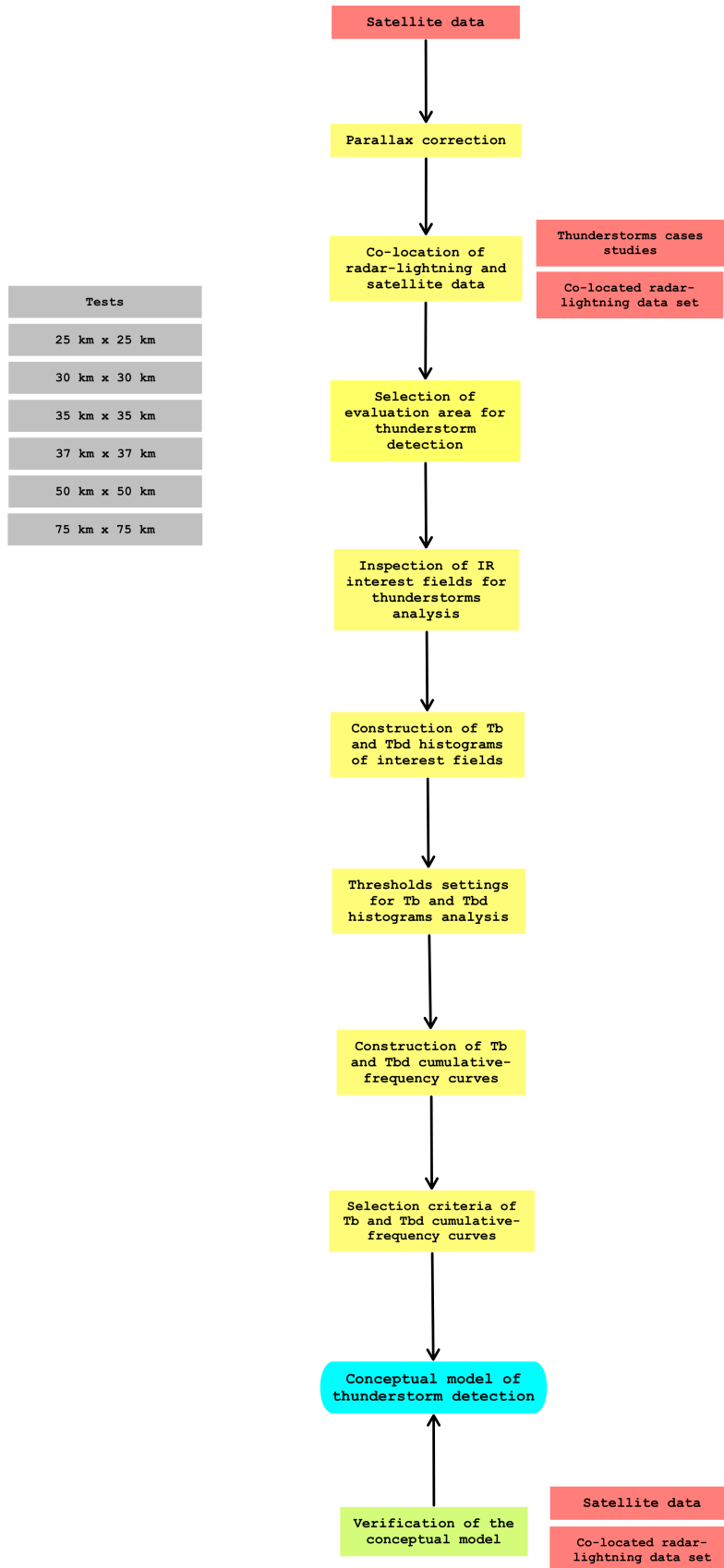


Figure 3.4 - Data (red rectangles); methods and tests (yellow and grey rectangles), and verification (green rectangle) for a conceptual model of thunderstorm detection.

*grey*; implemented to select an evaluation area for thunderstorm detection, and the conceptual model and corresponding verification in *green*; that will be presented in chapters 4 and 5, respectively.

### 3.3.1 Parallax correction

The Meteosat (MSG) satellites can be used for meteorological monitoring over southeastern Brazil. The southeastern region of Brazil is in the extreme corner of the MSG scanning domain (see figure 3.5). This accentuates the parallax error.

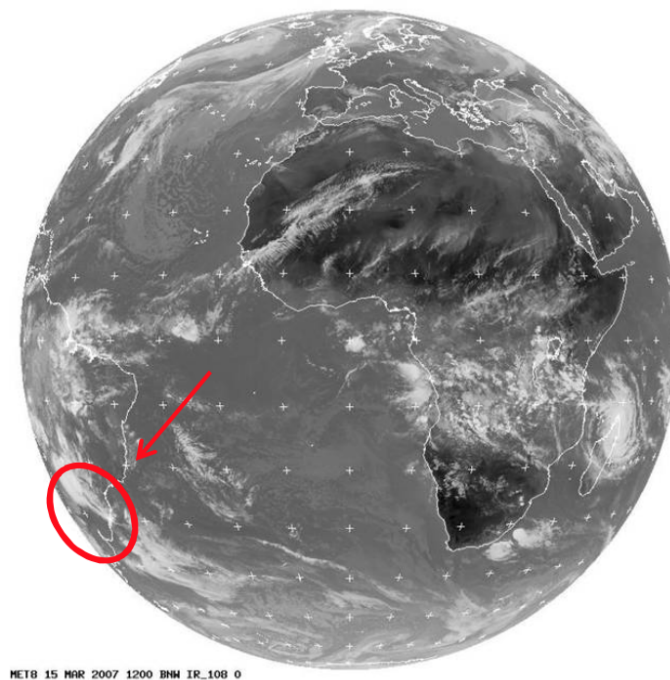


Figure 3.5 - The MSG-8 scanning domain and the southeastern region of Brazil located in the extreme corner of this domain. The image is observed in the infrared  $10.8 \mu\text{m}$  channel on March 15, 2007 at 1200 *UTC*.

Source: Adapted from (NASCIMENTO, 2014) and MSG-8 image provided by EUMETSAT.

There are procedures to reduce this parallax error and as mentioned in 2.2.2, the present study has employed a functionality available in the *Convection Working Group* website operated by *EUMETSAT*. This functionality for parallax correction to any cloud-top height information depicts in figure 3.6, the object at height  $-h_{cloud}$  – observed by a satellite at height  $-h_{sat}$  – above the Earth’s center, in a slightly different position than the position recorded by the satellite, so the functionality implementation required the following input: (i) several earth radius and satellite

information (earth radius at the pole, earth radius at the pole, radius ratio, satellite height above the Earth’s center, etc.); (ii) latitude and longitude of the sub-satellite point; (iii) latitude and longitude of the object (point B), and the (iv) satellite estimated height of the observed (cloud) object. The parallax correction functionality generates as *output*, the parallax corrected latitude of the object (point A) and the parallax corrected longitude of the object (point A).

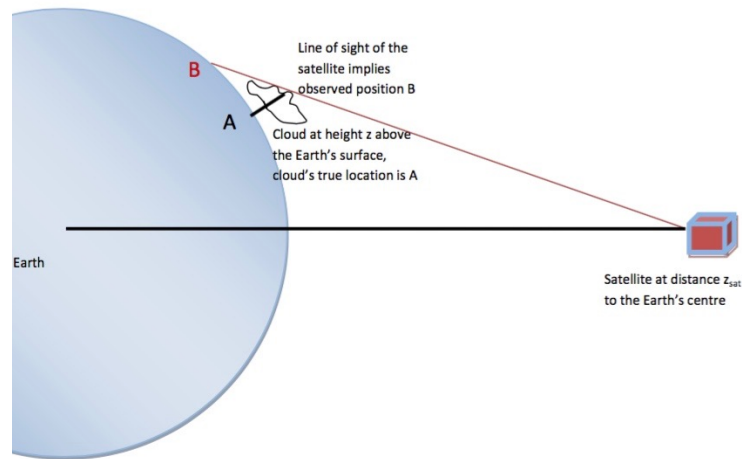


Figure 3.6 - Illustration (*not to scale*) of the concept of the parallax correction, where **B** is the observed position and **A** is the cloud’s true location.

Source: [http://www.essl.org/cwg/?page\\_id=33](http://www.essl.org/cwg/?page_id=33).

Following this for each case study lightning *time step*: first, the data and calculations for the input indicated in (i) and (ii), are known information. Second, the latitude and longitude of each *time step* have been considered as input for the assigned coordinates of the object indicated in (iii). Third, another functionality provided by the Satellite Division & Environmental Systems Group (DSA); based in the  $H_2O - IRW$  intercept method, has been implemented for the cloud height calculations indicated in (iv). More details of the  $H_2O - IRW$  intercept method can be found in (SZEJWACH, 1982; NIEMAN et al., 1993).

Figure 3.7 displays a flowchart as means to obtain these height calculations, so then the *Convection Working Group* functionality is implemented for the parallax correction and pixels re-location in corresponding (*MSG*) satellite observations.

Nevertheless, the parallax correction generates a problem related to empty pixels or pixels without information that appear in the recently corrected satellite images. This is due to the re-location of pixels, which in some cases can occupy the same

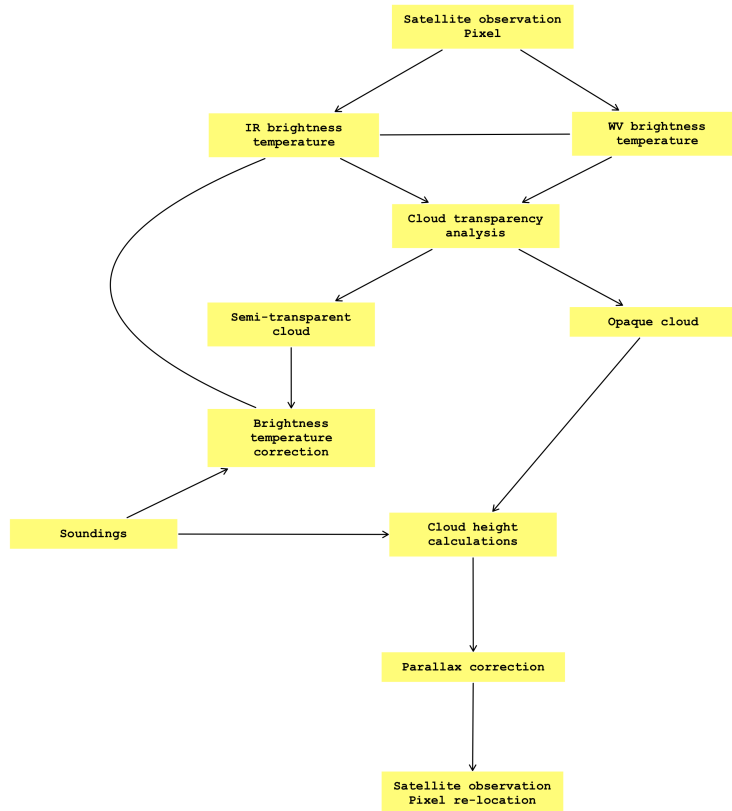


Figure 3.7 - Cloud-top height calculations for the parallax correction in *MSG* satellite imagery. For height calculations has been employed a functionality from *DSA-CPTEC/INPE* based in the  $H_2O - IRW$  intercept method. For parallax correction has been employed a functionality from *EUMETSAT*.  
Source: Adapted from (HUAMÁN, 2017).

place of other pixels after the correction; leaving pixels without information. Lábó et al. (2007) suggests a methodology to solve the problem of empty pixels, but the pixels without information are not taken into account for our study.

To put on view the effect of this correction in satellite images, figure 3.8 illustrates on the left, the  $10.8 \mu m$  channel observation without the parallax correction, and on the right, the  $10.8 \mu m$  channel observation without the parallax correction for a thunderstorm case study observed on March 10, 2012 at 1530 *UTC* (at  $t_3$  - the cloud-to-ground lightning flash). The parallax application is important when using radar and satellite data in tandem.

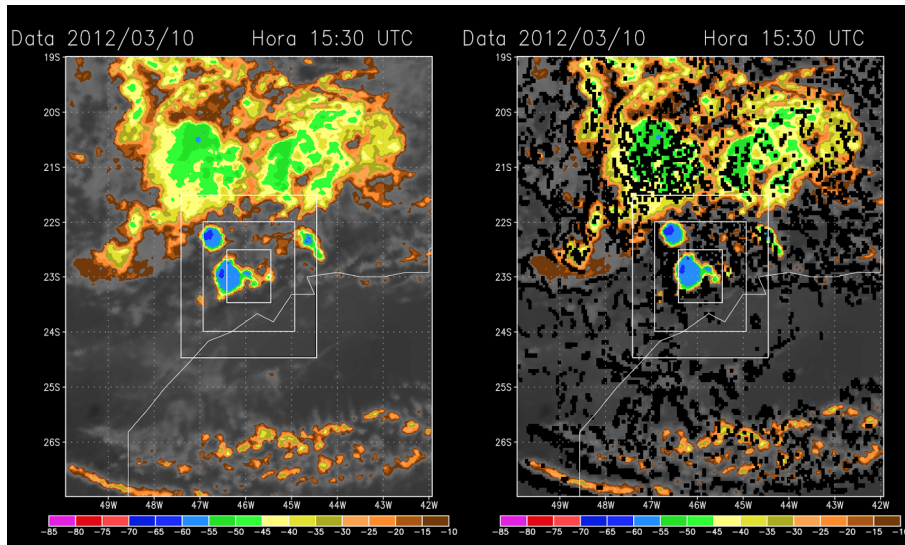


Figure 3.8 - Thunderstorm case study observed in  $10.8 \mu m$  channel on March 10, 2012 at 1530 UTC. **(left)** Satellite image without the parallax correction and **(right)** satellite image with the parallax correction. Pixels without information (or *black* pixels in the corrected satellite image) are not taken into account.

### 3.3.2 Co-location of radar-lightning and satellite data

The radar-lightning data set provides information for each case study evolution from the first radar echo up to the time of the first cloud-to-ground flash; information on the latitude, longitude and time of occurrence. Then, for these radar-lightning data has been selected the closest 15 – *min* satellite observation of the scene, that is, each *time step*'s latitude, longitude and time of occurrence have been co-located into corresponding satellite data. For example, the figure 3.9 is a vertical display of a thunderstorm case study from the first radar echo ( $t_0$ ) up to the time of the first cloud-to-ground flash ( $t_3$ ), whose radar and satellite data have been co-located. On the left, the radar reflectivity echo plots display information on a thunderstorm coordinates and time of occurrence for each lightning *time step*. On the right, corresponding  $10.8 \mu m$  channel plots display the closest 15 – *min* satellite observations selected for each lightning *time step*.

Consequently, these co-location of radar-lightning and satellite data allows each *time step* to become the center of an area for thunderstorm detection during the electrification life cycle. The selection of this evaluation area along with the dimensional constraints are discussed in subsection 3.3.3.

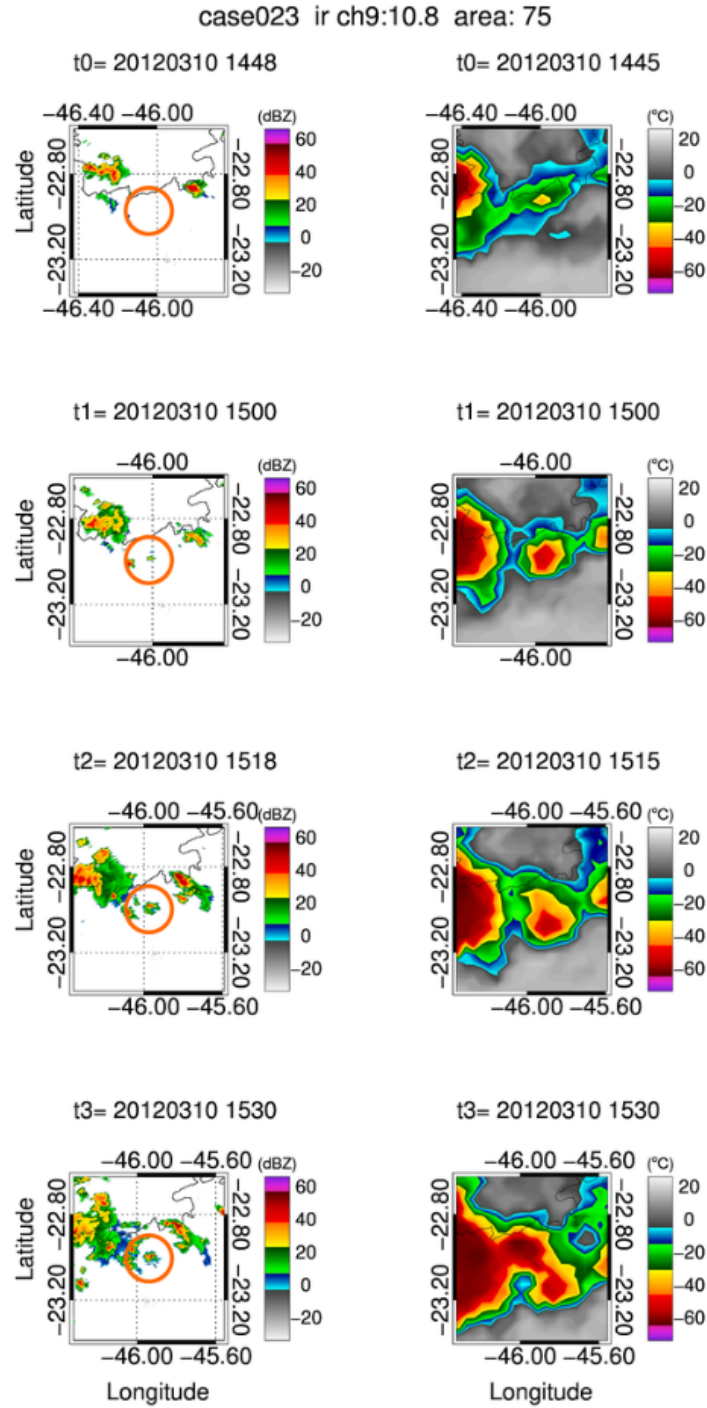


Figure 3.9 - Thunderstorm observed on March 10, 2012; within a  $75 \text{ Km} \times 75 \text{ Km}$  extension. **(left)** Radar echo plots of the electrification life cycle evolution from the first radar echo up to the time of the cloud-to-ground flash corresponding to  $1Echo (t_0) = 1448 \text{ UTC}$ ;  $Int (t_1) = 1500 \text{ UTC}$ ;  $1IC (t_2) = 1518 \text{ UTC}$ , and  $1CG (t_3) = 1530 \text{ UTC}$ ; **(right)**  $10.8 \mu\text{m}$  channel plots of the thunderstorm evolution at the co-located lightning *time steps*:  $1Echo (t_0) = 1445 \text{ UTC}$ ,  $Int (t_1) = 1500 \text{ UTC}$ ,  $1IC (t_2) = 1515 \text{ UTC}$ , and  $1CG (t_3) = 1530 \text{ UTC}$ .

### 3.3.3 Selection of an evaluation area for thunderstorm detection

An evaluation area for thunderstorm detection has been selected in the satellite observations considering the latitude and longitude of each thunderstorm's lightning *time step* as the area's center. Also, two physical requirements were assumed to determine the dimensions of this evaluation area.

The first requirement assumed for the dimensions ( $km \times km$ ) of the evaluation area is the detection efficiency of the SPLMA lightning mapping out of 100 to 150  $Km$  covering the CHUVA-Vale surveillance region (BLAKESLEE et al., 2013; CHMIELEWSKI; BRUNING, 2016; MATTOS et al., 2016). The second requirement assumed is the minimal noise required in the brightness temperature histograms or  $Tb$  ( $Tbd$ ) *relative frequency* distributions to be described in 3.3.5.

Thus, larger values for an evaluation area leads to a reduced noise in  $Tb$  ( $Tbd$ ) *relative frequency* distributions but increases the extent for thunderstorm detection. For example, an evaluation area of  $50 km \times 50 Km$  in a MSG observation of 4 km pixel resolution is equivalent to a square of 200  $Km$  side. A distance of 200  $Km$  exceeds the SPLMA distance of 100 to 150  $Km$  covering the surveillance region.

Consequently, the evaluation area could attain values between  $25 km \times 25 Km$  and  $37.5 Km \times 37.5 Km$  to comply with the SPLMA distance requirement. Then, dimensions as  $25 Km \times 25 Km$ ,  $30 Km \times 30 Km$ ,  $35 Km \times 35 km$  and  $37.5 Km \times 37.5 Km$ , respectively, have been tested for selection of the befitting area. The tests implemented with dimensions as  $50 Km \times 50 Km$  and  $75 Km \times 75 Km$  have been discarded for not complying with the first requirement.

The maximum and minimum noise in  $Tb$  ( $Tbd$ ) *relative frequency* distributions, or second requirement, are determined from the evaluation areas of  $25 Km \times 25 Km$  to  $37.5 Km \times 37.5 Km$ , respectively. After the visual assessment of a case study's corresponding  $10.8 \mu m$  channel  $Tb$  *relative frequency* distributions, for areas between  $25 Km \times 25 Km$  and  $37.5 Km \times 37.5 Km$ , the dimensions of  $30 Km \times 30 Km$  satisfied both requirements: the SPLMA distance and minimum noise in  $Tb$  *relative frequency* distributions, so these dimensions have been selected for the evaluation area for thunderstorm detection. See figures 3.10(a), 3.10(b) and 3.10(c) corresponding to  $10.8 \mu m$   $Tb$  *relative frequency* distributions for evaluation areas of  $25 km \times 25 Km$ ,  $30 Km \times 30 Km$  and  $37.5 Km \times 37.5 Km$ .

After an assessment of the cases studies from 3.2.4 with corresponding their lightning *time steps* centered around an evaluation area of  $30 \text{ Km} \times 30 \text{ Km}$ , a sequential sample of cases studies has been selected containing the electrification life cycles with best response in the  $10.8 \mu\text{m}$  channel.

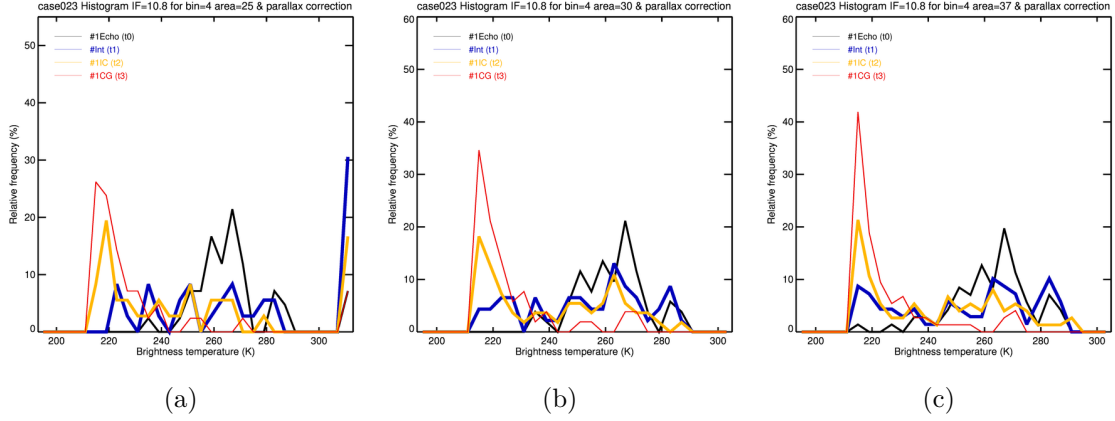


Figure 3.10 - *Tb relative frequency* distributions of  $10.8 \mu\text{m}$  channel for a thunderstorm electrification life cycle observed on March 10, 2012 within the evaluation areas of (a)  $25 \text{ Km} \times 25 \text{ Km}$ , (b)  $30 \text{ Km} \times 30 \text{ Km}$  and (c)  $37.5 \text{ Km} \times 37.5 \text{ Km}$ , respectively, centered around the following lightning *time steps*:  $1\text{Echo} (t_0) = 1445 \text{ UTC}$ ;  $1\text{Int} (t_1) = 1500 \text{ UTC}$ ;  $1\text{IC} (t_2) = 1515 \text{ UTC}$ , and  $1\text{CG} (t_3) = 1530 \text{ UTC}$ . These distributions have class interval width of  $+4.0 \text{ K}$ .

### 3.3.4 Inspection of IR *interest fields* for thunderstorm detection

First of all, the infrared radiation (longwave) detected by meteorological satellites is the terrestrial and atmospheric radiation emitted by the Earth's surface, the atmospheric components and clouds. Thus, between the most used IR bands can be mentioned the following from Meteosat Satellites:  $6.5 \mu\text{m}$  (channel 5),  $7.3 \mu\text{m}$  (channel 6),  $8.7 \mu\text{m}$  (channel 7),  $9.7 \mu\text{m}$  (channel 8) and  $12.0 \mu\text{m}$  (channel 10). The figure 3.11 shows the absorption of electromagnetic radiation by the Earth's atmosphere across a wide wavelength range and indicates five of the most used IR bands.

Besides, this subsection aims to inspect a subset of 4 *interest fields* calculated from the five IR channels ( $6.2, 7.3, 8.7, 10.8$  and  $12.0 \mu\text{m}$ ); 4 *interest fields* capable of demonstrating a *differentiation* between the *Tb* (*Tbd*) *relative frequency* distributions of lightning *time steps*, and capable of detecting the region of development of convective and electrification processes inside these distributions of *Tb* (*Tbd*) *relative frequency*. Consequently, an inspection of these channel differences

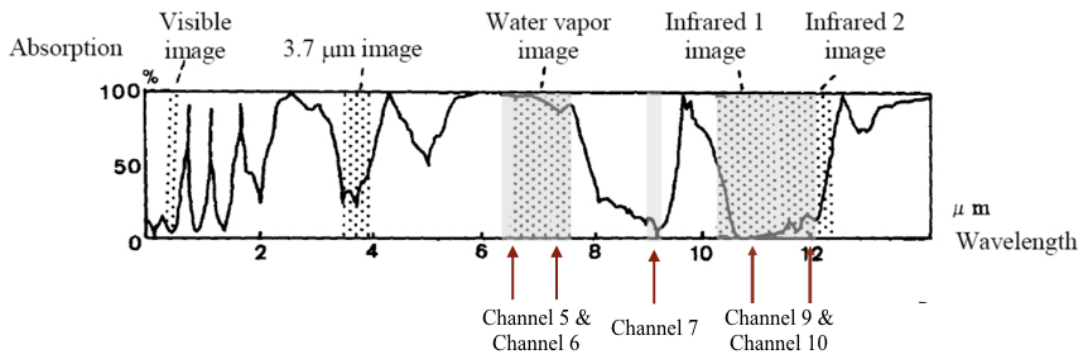


Figure 3.11 - Absorption spectrum of electromagnetic radiation by the Earth's atmosphere across a wide wavelength range. Five of the most used IR channels from Meteosat Satellites are indicated with arrows: Channels 5 and 6 (water vapor image), channels 9 and 10 (infrared images), and channel 7 ( $8.7\mu m$ ).  
Source: Adapted from (NASCIMENTO, 2014).

and corresponding assessment direction inside the  $Tb$  ( $Tbd$ ) histograms for thunderstorm detection is built below around physical attributes such as cloud depth and cloud-top glaciation.

### 3.3.4.1 Ch05-Ch06: ( $6.2 - 7.3$ ) $\mu m$

The radiance measured by the satellite in these water vapor bands can be associated with a brightness temperature, but there is a strong absorption by the water vapor in the atmosphere, of the longwave radiation emitted by the surface. Thus, almost nothing of the longwave radiation of the surface in these bands reach the satellite.

The troposphere at low levels is very rich in water vapor, therefore there is strong emission of longwave radiation by water vapor. However, the path to be covered by the longwave radiation at low levels is very long before reaching the satellite. Then, in the water vapor bands, the longwave radiation of the troposphere at low levels is almost entirely absorbed before reaching the satellite, either by the water vapor of the troposphere at medium and high levels.

The troposphere at medium levels still has a significant proportion of water vapor; therefore the emission of longwave radiation in this layer in the water vapor bands is still significant. As the rising longwave radiation of this layer will find only the water vapor of the troposphere at high levels, which is a very low proportion, then there will be a little absorption by the water vapor at high levels and much of the longwave radiation's emission of the medium levels will reach the satellite.

The troposphere at high levels contains a low proportion of water vapor, that is why the longwave radiation emitted at high levels is not as significant as at medium levels in the water vapor bands. (See figure 3.12).

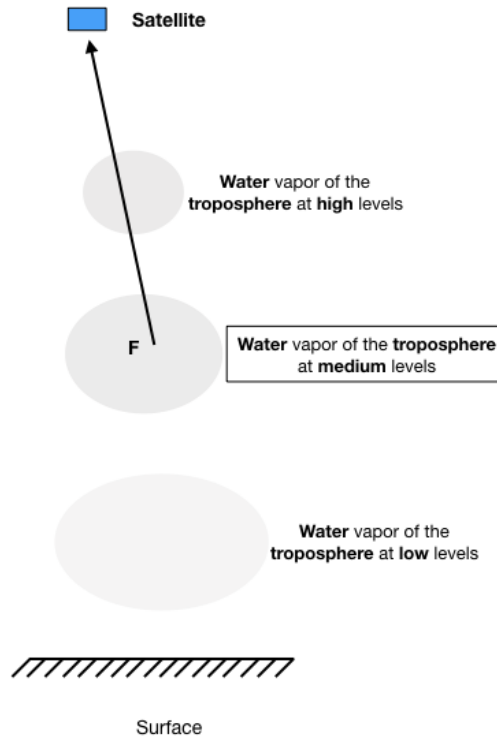


Figure 3.12 - Schematic depiction of radiative coupling in water vapor channels as an indicator of moisture content at medium levels of the troposphere. F is the longwave emission upward by the troposphere at medium levels.

Source: Adapted from (PETTY, 2006; NASCIMENTO, 2014).

Moreover, the water vapor channel differences such as  $(6.2 - 7.3) \mu m$  demonstrate sensitivity for the water vapor content in the upper and medium troposphere, thus can give an indication of the moisture content at medium levels and cloud depth. The premise is that when the difference's values gradually approach to zero, it is an indication of changes of brightness temperature because the deepening of cumulus clouds. (ROESLI et al., 2007; MATTHEE; MECIKALSKI, 2013).

This *interest field* of  $(6.2 - 7.3) \mu m$  will be considered a cloud depth indicator. For example, the statistical values for 123 cases studies identified by Mecikalski et al. (2010) in this *interest field* were to use a mean of  $Tbd = -6.6 K$  and standard deviation of  $Tbd = +5.94 K$ ; as deep cumulus clouds grow along with the channel difference becoming smaller or near to zero, or even becoming slightly negative.

Accordingly for the analysis of our cases studies, the corresponding assessment direction in the  $(6.2 - 7.3) \mu m$  *Tbd relative frequency* distributions has been established from the negative channel differences toward the positive channel differences.

#### 3.3.4.2 Ch09: 10.8 $\mu m$

In a infrared channel such as  $10.8 \mu m$ , the satellite will detect a more intense radiance emitted by the heated surface of the Earth than the radiance emitted by the top of a cloud (see figure 3.13). Besides, the lowest values of brightness temperature of the  $10.8 \mu m$  channel are to be related with highest cloud tops and regions of intense convective updrafts, that is, with processes of cloud depth (MECIKALSKI et al., 2010; MATTHEE; MECIKALSKI, 2013).

The *interest field* of  $10.8 \mu m$  is intuitively related to cloud processes and will be considered as a cloud depth indicator. For example, the statistical values for 123 cases in Europe identified by Mecikalski et al. (2010) in this channel were to use a mean of  $Tb = +242.5 K$  and standard deviation of  $Tb = +16.79 K$  (see 2.2.1.1); as cases of deep cumulus cloud-tops grow along South America with  $Tb$  values colder than  $+235.0 K$  (VILA, 2004).

Accordingly for the analysis of our cases studies, the corresponding assessment direction in  $10.8 \mu m$  *Tb relative frequency* distributions has been established from  $Tb$  values colder than  $+235.0 K$ .

#### 3.3.4.3 Ch05-Ch09: $(6.2 - 10.8) \mu m$

In channel differences such as  $(6.2 - 10.8) \mu m$ , the brightness temperature of  $10.8 \mu m$  channel is normally warmer than  $6.2 \mu m$  absorption channel, thus the  $(6.2 - 10.8) \mu m$  channel difference is normally negative. Nevertheless, it is found that over high level cloud tops, the brightness temperature in the WV channel can be larger than the IR channel by as much as  $6.0$  to  $8.0 K$ , so positive values of this *field* had been demonstrated to correspond with convective cloud-tops that are at or above the tropopause (overshooting tops) (ACKERMAN, 1996; SCHMETZ et al., 1997; MECIKALSKI; BEDKA, 2006).

This *field* is related to overshooting tops and will be considered as a cloud depth indicator. For example, the mean and standard deviation values for 123 cases studies identified by Mecikalski et al. (2010) were to use values of  $-14.6 K$  and  $+11.27 K$ ; as deep cumulus clouds grow along with *Tbd* values becoming larger than  $-15.0 K$  due to a large potential for cloud-to-ground discharge activity (MACHADO et al., 2009).

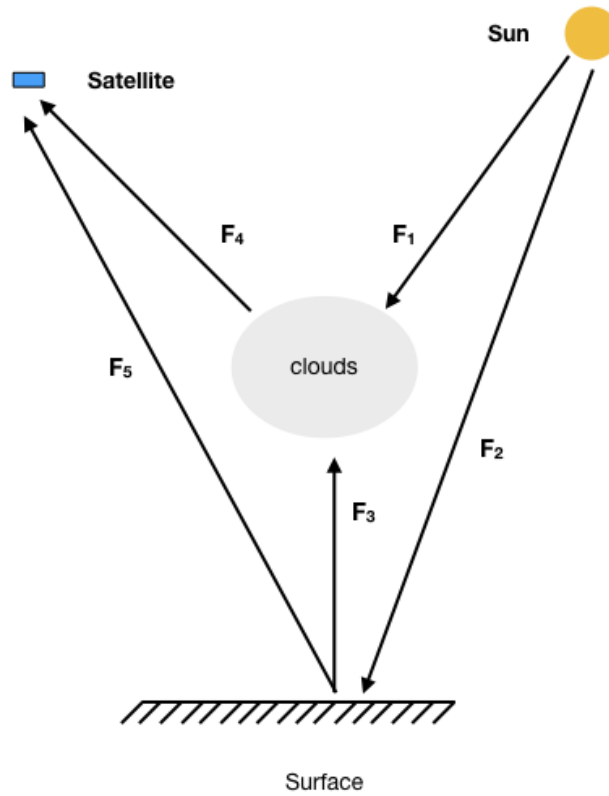


Figure 3.13 - Schematic figure of radiative coupling in infrared channel between the surface and a layer of clouds.  $F_1$  and  $F_2$  are the incident shortwave flux from the sun,  $F_3$  and  $F_5$  are the longwave emission by the surface and  $F_4$  is the longwave emission by the layer of clouds.

Source: Adapted from (PETTY, 2006; NASCIMENTO, 2014).

Accordingly for the analysis of our cases studies, the corresponding assessment direction in the  $(6.2-10.8) \mu m$  *Tbd relative frequency* distributions has been established from  $-14.0 K$  toward the positive channel differences.

#### 3.3.4.4 Trispectral: $[(8.7 - 10.8) - (10.8 - 12.0)] \mu m$

A trispectral combination of observations at  $8.7$ ,  $10.8$  and  $12.0 \mu m$  channels, such as the  $[(8.7 - 10.8) - (10.8 - 12.0)] \mu m$  *interest field*, is suggested for detecting cloud physical attributes as glaciation indicators. Channel differences as  $(10.8 - 12.0) \mu m$  have the characteristic of larger *Tbd* values than channel differences as  $(8.7 - 10.8) \mu m$  in water clouds, but  $(10.8 - 12.0) \mu m$  have lower *Tbd* values than  $(8.7 - 10.8) \mu m$  values in ice clouds. Consequently, water clouds will have negative *Tb* values for the trispectral combination, whereas ice clouds will have positive values (STRABALA; ACKERMAN, 1994; MATTHEE; MECIKALSKI, 2013).

This *interest field* is related to ice clouds and will be considered as a cloud-top glaciation indicator. For example, the statistical values for 123 cases studies in Europe identified by Mecikalski et al. (2010) were to use a mean of  $Tbd = -0.6 K$  and standard deviation of  $Tbd = +1.9 K$ ; as deep cumulus clouds grow along with positive values of the channel difference (MATTHEE; MECIKALSKI, 2013).

Accordingly for the analysis of our cases studies, the corresponding assessment direction in the  $(8.7 - 10.8) - (10.8 - 12.0) \mu m$   $Tbd$  relative frequency distributions has been established from  $0 K$  toward the positive channel differences.

### 3.3.5 Construction of the $Tb$ ( $Tbd$ ) histograms of IR interest fields

*Histograms* are graphic representations of *frequency distributions* for summarizing a data set and disclosing its attributes (WILKS, 1995; SPIEGEL; STEPHENS, 2007).

For disclosing the attributes of our  $Tb$  ( $Tbd$ ) data set in every interest field during the electrification processes, here is to be represented the  $Tb$  ( $Tbd$ ) histograms of a thunderstorm observed within an evaluation area of  $30 Km \times 30 Km$  centered at each lightning *time step*; where also the largest and the smallest values of  $Tb$  ( $Tbd$ ) have been determined and thus the range is found. Then this range has been divided into a convenient number of class intervals having the same size.

But in accordance to Wilks (1995), the main issue to be confronted when representing a *histogram* is the choice of the interval size, because intervals too wide will result in important details of the data being masked and intervals too narrow result in a plot that is difficult to interpret. Therefore, the best interval size in each interest field for describing the electrification life cycle processes has resulted from the capability to represent a *differentiation* between the thunderstorm's lightning *time steps* with a minimum noise in corresponding  $Tb$  ( $Tbd$ ) histograms for an evaluation area of  $30 Km \times 30 Km$ .

Again, the number of  $Tb$  ( $Tbd$ ) values falling into each class interval or class frequency has been determined and divided by the total frequency of all classes to represent the *relative frequency* in the vertical-axis. Next, a polygon of the class frequency has been plotted against the class mark to obtain each lightning *time step* histogram, so the 4 histograms of lightning *time steps* has been represented inside a 4 polygons; where the *black* is for  $1Echo$  ( $t_0$ ), the *blue* is for  $Int$  ( $t_1$ ), the *yellow* is for  $1IC$  ( $t_2$ ) and the *red polygon* is for  $1CG$  ( $t_3$ ).

For example, figure 3.14(b) details the  $10.8 \mu\text{m}$   $Tb$  histograms and figure 3.14(a) details the  $(6.2 - 7.3) \mu\text{m}$   $Tbd$  histograms for a thunderstorm electrification life cycle observed within an evaluation area of  $30 \text{ km} \times 30 \text{ Km}$  centered around the following *time steps*: 1Echo ( $t_0$ )= 1445 UTC (*black*); Int ( $t_1$ )= 1500 UTC (*blue*); 1IC ( $t_2$ )= 1515 UTC (*yellow*) and 1CG ( $t_3$ )= 1530 UTC (*red*). These  $Tb$  and  $Tbd$  histograms have an equal interval width of  $+4.0 \text{ K}$ .

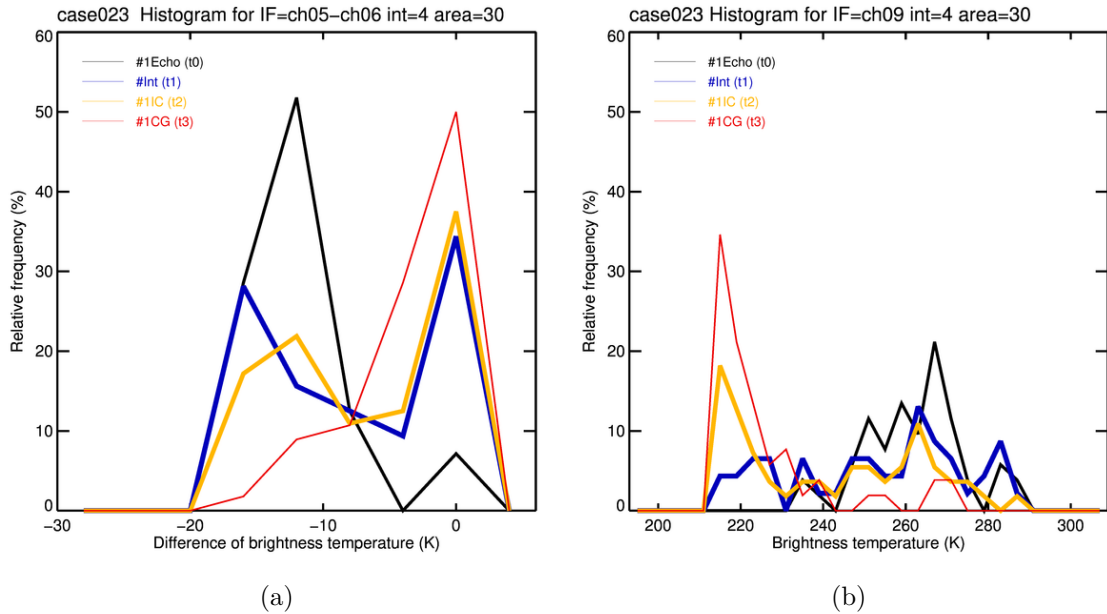


Figure 3.14 - *Histograms* of (a)  $(6.2-7.3) \mu\text{m}$  channel difference and (b)  $10.8 \mu\text{m}$  channel for a thunderstorm observed on March 10, 2012 within an evaluation area of  $30 \text{ km} \times 30 \text{ Km}$  centered around the following *time steps*: 1Echo ( $t_0$ ) = 1445 UTC; Int ( $t_1$ ) = 1500 UTC; 1IC ( $t_2$ ) = 1515 UTC, and 1CG ( $t_3$ ) = 1530 UTC. These *histograms* have class interval width of  $+4.0 \text{ K}$ .

### 3.3.6 Thresholds settings for analysis of the $Tb$ ( $Tbd$ ) histograms

The IR interest fields inspection built around physical attributes inside an incipient thunderstorm; the  $Tb$  (or  $Tbd$ ) histograms and correspondent assessment directions are for disclosing which region inside these histograms presents indicators of intensification in the convective and electrification processes.

Moreover, for analyzing this histogram's region of cloud intensification in each interest field, some thresholds must be established to detect the strongest convective indicators and thus, to detect the largest differentiation among the corresponding  $Tb$  (or  $Tbd$ ) histograms of a case study's lightning time steps.

For further analysis, all the  $Tb$  ( $Tbd$ ) observations belonging to a given class interval are assumed to coincide with the class mark, or the midpoint of the class; so this assumption is also valid in the *thresholds* settings.

Recalling, the (6.2 – 7.3)  $\mu m$  assessment direction to detect cloud *intensification* is from negative channel differences toward the positive channel differences. Hence, the region to detect largest *differentiation* among the lightning *time steps* begins from *thresholds* established as  $Tbd \geq -16.0 K$ ; that should provide significant information regarding *intensification* of cloud and electrification processes throughout the *histograms* of  $Tbd = +4.0 K$  class interval width.

Concerning the 10.8  $\mu m$  channel, the assessment direction to detect cloud *intensification* is for  $Tb$  values colder than  $+235.0 K$ . Hence, the region to detect the largest differences among the lightning *time steps* begins from *thresholds* established as  $Tb \leq +235.0 K$ ; that should provide significant information about *intensification* of cloud and electrification processes throughout the *histograms* of  $Tb = +4.0 K$  class interval width.

As mentioned for (6.2 – 10.8)  $\mu m$ , the assessment direction to detect cloud *intensification* is from  $-14.0 K$  toward the positive channel differences. Hence, the region to detect largest *differentiation* among the lightning *time steps* begins from *thresholds* established as  $Tbd \geq -14.0 K$ ; that should provide significant information regarding *intensification* of cloud and electrification processes throughout the *histograms* of  $Tbd = +4.0 K$  class interval width.

In addition, the *trispectral* interest field assessment direction to detect cloud *intensification* is from  $0 K$  toward the positive channel differences. Hence, the region to detect largest *differentiation* among the lightning *time steps* begins from *thresholds* established as  $Tbd \geq 0 K$ ; that should provide significant information regarding *intensification* of cloud and electrification processes throughout the *histograms* of  $Tbd = +1.0 K$  class interval width.

### 3.3.7 Construction of the $Tb$ ( $Tbd$ ) relative cumulative-frequency curves

For the  $Tb$  ( $Tbd$ ) *histograms* of a case study's lightning *time steps*, the sum of the *relative frequency* of all class intervals is 100%. Besides, the *relative cumulative-frequency* distribution of all values *less* than or equal to a class boundary of each class interval is called a "less" distribution. In the same way, the *relative cumulative-frequency* distribution of all values *greater* than or equal to the lower

class boundary of each class interval is called a "more" distribution (WILKS, 1995; SPIEGEL; STEPHENS, 2007).

Here, it depends if the  $Tb$  ( $Tbd$ ) *histograms* assessment direction to detect cloud *intensification* is toward the negative values, so "less" is a distribution, or, toward the positive values, so is a "more" distribution.

Considering the  $Tb$  ( $Tbd$ ) *histograms* of a case study's lightning *time steps* and corresponding *thresholds* in each interest field, the "less" or "more" distribution for one *threshold* has been built as follows: (i) a "less" curve is obtained plotting against each *time step*, the value less than or equal to the class boundary of that *threshold* class interval, and then connecting all these points, or, (ii) a "more" curve is obtained plotting against each *time step*, the value greater than or equal to the lower class boundary of that *threshold* class interval, and then connecting all these points. Similarly for all the  $Tb$  ( $Tbd$ ) *thresholds* of a thunderstorm case study.

For example, a case study observed through the  $10.8 \mu m$  channel within an evaluation area of  $30 km \times 30 Km$ ; figure 3.15 presents the "less" distributions for all *thresholds* from  $Tb \leq +235.0 K$ , as we are looking for the smaller values associated to higher cloud-tops. Additional *thresholds* were plotted like  $Tb = +263.0 K$  is displayed in the *black line*.

Table 3.3 presents the  $Tb$  *relative frequency* and "less" distributions for *thresholds* from  $Tb \leq +235.0 K$  during the 1*Echo* and 1*CG* lightning *time steps*, respectively. The histograms populations denoted an increase from 3.85 to 84.61% in pixels with values of  $Tb \leq +235.0 K$ . This increasing variability in the histograms populations is also noted in figure 3.15 and can be related to *intensification* of the thunderstorm processes along the lighting time steps.

### 3.3.8 Analysis of the $Tb$ ( $Tbd$ ) *relative cumulative-frequency curves*

After the construction of the  $Tb$  ( $Tbd$ ) *relative cumulative-frequency curves* for all *thresholds*, it was established a selection criteria as means to find the *threshold* which is most capable of detecting *differentiation* between lightning *time steps* and *intensification* of thunderstorm processes inside the corresponding histograms.

The operation of finding a differentiation in a function also is called *derivative* of that function. The geometric meaning of the *derivative* can be approached to the tangent of the angle formed with the positive direction of the horizontal-axis by the line tangent to the "less" ("more") curve at corresponding lightning *time step*.

Table 3.3 - The  $10.8 \mu m$   $Tb$  relative frequency and "less" distributions for thresholds from  $Tb \leq +235.0 K$  during 1Echo and 1CG of a thunderstorm observed on March 10, 2012 within an evaluation area of  $30 km \times 30 Km$  centered around respective lightning time steps: 1Echo= 1445 UTC and 1CG= 1530 UTC.

Class No.	Class mark(K)	Interval width(K)	Rel. freq.(%)	Less rel. freq.(%)
1Echo (t0) = 1445 UTC				
01	+195.0	+4.0	0.00	0.00
02	+199.0	+4.0	0.00	0.0
03	+203.0	+4.0	0.00	0.00
04	+207.0	+4.0	0.05	0.00
05	+211.0	+4.0	0.00	0.00
06	+215.0	+4.0	0.00	0.00
07	+219.0	+4.0	0.00	0.00
08	+223.0	+4.0	0.00	0.00
09	+227.0	+4.0	0.00	0.00
10	<b>+231.0</b>	+4.0	0.00	<b>0.00</b>
11	+235.0	+4.0	3.85	3.85
1CG (t3) = 1530 UTC				
01	+195.0	+4.0	0.00	0.00
02	+199.0	+4.0	0.00	0.0
03	+203.0	+4.0	0.00	0.00
04	+207.0	+4.0	0.05	0.00
05	+211.0	+4.0	0.00	0.00
06	+215.0	+4.0	34.62	34.62
07	+219.0	+4.0	21.15	55.77
08	+223.0	+4.0	13.46	69.23
09	+227.0	+4.0	5.77	75.00
10	<b>*+231.0</b>	+4.0	7.69	<b>82.69</b>
11	+235.0	+4.0	1.92	84.61

For all *thresholds* of the "less" ("more") curves against a case's lightning *time steps*, the *threshold* correspondent to the curve with greater value of *maxima derivative* has been established as selection criteria for detecting the most significant *intensification* of cloud and electrification processes to be attained.

As example of a case observed through the 10.8  $\mu m$  channel within an area of 30  $km \times 30 Km$ , the figure 3.16 and table 3.4 present that the *threshold* correspondent to the "less" curve with greater value of *maxima derivative* is  $Tb = +231.0 K$  for detecting the most significant *intensification* of cloud processes to be attained.

Furthermore, linking the 1Echo ( $t_0$ ) and the 1CG ( $t_3$ ) *time step* in table 3.3 and figure 3.16, there is a variability of pixels with values of  $Tb \leq +231.0 K$  from 0 to 82.69% in the *Tb histograms* populations. This variability has an *increasing* trend and might be considered as potential information regarding *intensification* of the thunderstorm processes.

As consequence for a 1 case study observed through 1 *IR interest field* within an evaluation area of 30  $km \times 30 Km$ ; taking into account the *Tb (Tbd) threshold* correspondent to the "less" ("more") curve with greater value of *maxima derivative* and the variability between each lightning *time step's Tb (Tbd) histogram* population, all these might be contemplated as potential information with regard to *intensification* of cloud and electrification processes.

Considering this information in a large sample of 40 cases studies observed through 4 *IR interest fields* within an evaluation area of 30  $Km \times 30 Km$  will be crucial for the accuracy of the conceptual model of thunderstorm detection.

Following the data and methods presented above, chapter 4 outlines the results for a sample of forty cases studies from the CHUVA-Vale field campaign observed through 4 *IR interest fields* within an evaluation area of 30  $km \times 30 Km$ . Next, chapter 5 summarizes a verification of the conceptual model of thunderstorm detection.

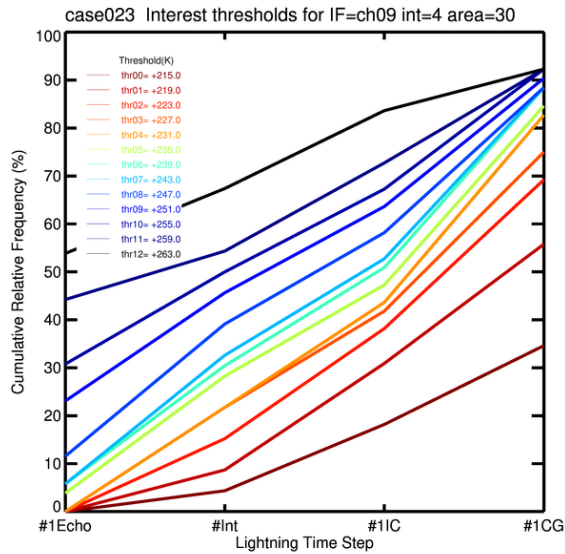


Figure 3.15 - The  $10.8 \mu m$  "less" distributions for *thresholds* from  $T_b \leq +263.0 K$  plotted against each lightning *time step* considering a thunderstorm observed on March 10, 2012 within an evaluation area of  $30 km \times 30 km$  centered around respective *time steps*:  $1Echo (t_0) = 1445 UTC$ ;  $Int (t_1) = 1500 UTC$ ;  $1IC (t_2) = 1515 UTC$ , and  $1CG (t_3) = 1530 UTC$ . The *thresholds* of  $T_b \leq +215.0 K$  have negligible slopes.

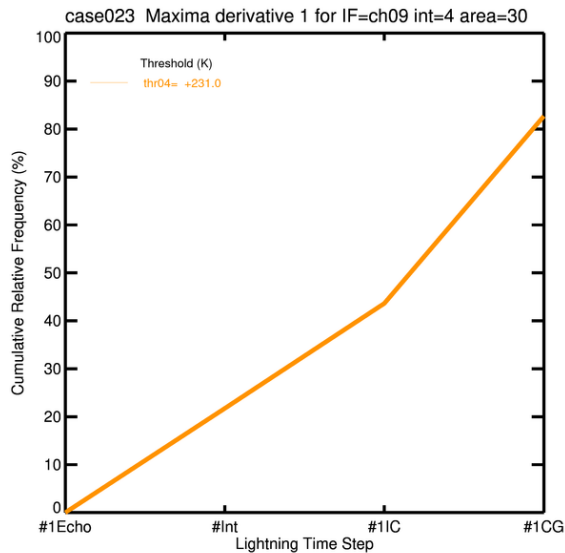


Figure 3.16 -  $T_b$  *relative cumulative-frequency* or "less" distribution with greater value of *maxima derivative* plotted against each *time step* considering a thunderstorm observed through the  $10.8 \mu m$  channel on March 10, 2012 within an area of  $30 km \times 30 Km$  centered around respective *time steps*:  $1Echo (t_0) = 1445 UTC$ ;  $Int (t_1) = 1500 UTC$ ;  $1IC (t_2) = 1515 UTC$ , and  $1CG (t_3) = 1530 UTC$ . The *threshold* with greater value of *maxima derivative* is  $T_b = +231.0 K$ .

Table 3.4 - The  $Tb$  thresholds of *maxima derivative* and correspondent lightning *time step* locations in the  $10.8 \mu m$  "more" distributions curves considering a thunderstorm observed through the  $10.8 \mu m$  channel on March 10, 2012 within an area of  $30 km \times 30 Km$  centered around respective *time steps*:  $1Echo (t0)= 1445$  UTC;  $1Int (t1)= 1500$  UTC;  $1IC (t2)= 1515$  UTC, and  $1CG (t3)= 1530$  UTC. The *threshold* with greater value of *maxima derivative* is  $Tb= +231.0 K$  (*asterisk*).The *thresholds* of  $Tb \leq +215.0 K$  have negligible slopes.

Class No.	Threshold (K)	Max derivative	Time step
06	+215.0	1.63	$1CG (t3)$
07	+219.0	2.48	$1CG (t3)$
08	+223.0	3.10	$1CG (t3)$
09	+227.0	3.31	$1CG (t3)$
10	<b>*+231.0</b>	<b>3.90</b>	$1CG (t3)$
11	+235.0	3.73	$1CG (t3)$
12	+239.0	3.75	$1CG (t3)$
13	+243.0	3.57	$1CG (t3)$
14	+247.0	3.02	$1CG (t3)$
15	+251.0	2.67	$1CG (t3)$
16	+255.0	2.50	$1CG (t3)$
17	+259.0	1.95	$1CG (t3)$
17	+263.0	1.62	$IC (t2)$

## 4 Results

Recalling the methods to obtain information with regard to *intensification* of thunderstorm processes through 4 *IR interest fields*, that is, the (i.) parallax correction in satellite data; (ii.) co-location of satellite and radar-lightning data; (iii.) selection of an evaluation area for thunderstorm detection; (iv.) construction of *Tb (Tbd) histograms*; (v.) thresholds settings for *Tb (Tbd) histograms*, (vi.) construction of *Tb (Tbd) relative cumulative-frequency* distributions, and the (vii.) selection criteria for *Tb (Tbd) relative cumulative-frequency* curves.

Considering the methods in a sample of 40 compact thunderstorms cases studies, the results presented below in 4.1 are the *Tb (Tbd) histograms* and respective statistical values in each lightning *time step*, the *Tb (Tbd) thresholds* correspondent to each "less" ("more") curve with greater value of *maxima derivative* and the variability between *Tb (Tbd) histograms* populations to detect significant information regarding *intensification* of thunderstorm processes. Also 4 predictors for a conceptual model of thunderstorm detection obtained using 4 *IR interest fields* and based on corresponding *Tb (Tbd) thresholds* are presented in section 4.2.

### 4.1 Thunderstorm detection using each *IR interest field* imagery

First, the parallax correction has been applied using each *IR interest field* observations from 01 November 2011 to 31 March 2012 as detailed in subsection 3.3.1. Subsequently, the co-location of corrected satellite observations and radar-lightning data of the 40 selected electrification life cycles has been performed as detailed in subsection 3.3.2 for analyzing the information derived from the *Tb (Tbd) histograms*.

Second, in subsections 4.1.1; 4.1.3, 4.1.1 and 4.1.7 are presented the *Tb (Tbd) histograms* and statistical values, and next in subsections 4.1.2; 4.1.4, 4.1.6 and 4.1.8 are presented the *Tbd thresholds* and the variability between *Tb (Tbd) histograms* populations for each *IR interest field*.

#### 4.1.1 (6.2 – 7.3) $\mu\text{m}$ : *Tbd histograms* and statistical values

The (6.2–7.3)  $\mu\text{m}$  interest field can give an indication of moisture content at medium levels and depth of the convective clouds. For more details see 3.3.4.1.

Figure 4.1 illustrates the *Tbd histograms* of this interest field for 40 cases studies within an evaluation area of  $30\text{ km} \times 30\text{ km}$  centered around the 4 lightning *time steps*: 1*Echo* ( $t_0$ ) - first echo with any value of reflectivity above the reflectivity

noise level; *Int* (*t1*) - intermediate stage between first reflectivity echo and first intra-cloud lightning flash, *1IC* (*t2*) - first intra-cloud lightning flash and *1CG* (*t3*) - first cloud-to-ground lightning flash.

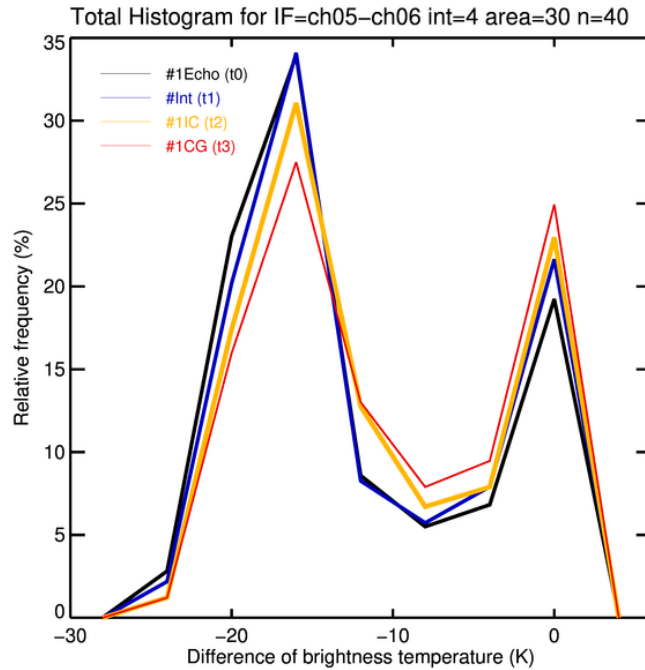


Figure 4.1 - *Tbd* histograms of  $(6.2 - 7.3) \mu m$  interest field for a sample of 40 thunderstorms size within an evaluation area of  $30 km \times 30 km$  centered around respective lightning *time steps*. The *histograms* interval width is  $+4.0 K$ .

In the histograms of  $(6.2 - 7.3) \mu m$  field, the range data has been divided into 9 class intervals or *bins* of  $Tbd = +4.0 K$  equal interval width. The distribution of the data is multimodal with *relative frequency* humps in  $-16.0 K$  and  $0 K$ . These humps are inside the region of the *threshold* settings, established as  $Tbd \geq -16.0 K$  that can provide significant information regarding *intensification* of cloud processes.

Following this in  $Tbd = -16.0 K$ , the relative frequency is 33.93% for *1Echo* (black polygon), 34.09% for *Int* (blue polygon), 31.07% for *1IC* (yellow polygon) and 27.50% for *1CG* (red polygon). Also in  $Tbd = 0 K$ , the relative frequency is 19.23% for *1Echo*, 21.63% for *Int*, 22.96% for *1IC* and 24.94% for *1CG*. More details of the *Tbd* *relative cumulative-frequency* distributions can be found in table 4.3.

The statistical values for 40 cases studies are synthesized in table 4.1, which from *1Echo* (*t0*) to *1CG* (*t3*) *time steps* are to use mean values between  $Tbd = -12.47$  and  $-10.44 K$ , and standard deviation values between  $Tbd = +7.60$  and  $+7.39 K$ .

Nevertheless, the values for 123 cases identified by Mecikalski et al. (2010)'s study and mentioned in 3.3.4.1 were to use a mean of  $Tbd = -6.6 K$  and standard deviation of  $Tbd = +5.94 K$ . The statistical values obtain by these 2 studies may differ due to the region of study and dissimilarity in defined stages of the thunderstorms cases (see 2.1), but can be noted that main statistical signals are well represented in the present study analysis.

Inspecting the present study's statistical values from 1Echo ( $t_0$ ) to 1CG ( $t_3$ ) lighting time steps in table 4.1, can be indicated an increase greater than  $Tbd = +2.0 K$  in the mean and median values. The channel differences become smaller accordingly with the trend expected in 3.3.4.1 correspondent with growing cumulus cloud-tops. On the other hand, following the trend expected in 3.3.4.1, cannot be indicated a significant change between the minimum  $Tbd$  values (less than  $Tbd = +1.0 K$ ) from 1Echo ( $t_0$ ) to 1CG ( $t_3$ ) lighting time steps.

Table 4.1 - Mean, standard deviation, median and minimum values for the (6.2 – 7.3)  $\mu m$   $Tbd$  histograms of +4.0 K interval width considering the sample of 40 thunderstorms size (see figure 4.1). These  $Tbd$  values are compared above with the values of Mecikalski et al. (2010) indicated in 3.3.4.1.

Time	Step	Mean (K)	Std dev (K)	Median (K)	Min (K)
$t_0$	1Echo	-12.47	+7.47	-15.64	-25.09
$t_1$	Int	-11.81	+7.60	-15.08	-25.53
$t_2$	1IC	<b>-11.09</b>	+7.39	-13.92	<b>-25.27</b>
$t_3$	1CG	-10.44	+7.43	-12.90	-25.27

#### 4.1.2 (6.2 – 7.3) $\mu m$ : $Tbd$ thresholds and histograms populations

Figure 4.2 presents the "more" curves from thresholds established as  $Tbd \geq -16.0 K$  for 40 cases within an evaluation area of  $30 km \times 30 km$ . In the vertical-axis, the values of  $Tbd$  relative cumulative-frequency (%) greater than or equal to the lower class of each threshold class have been plotted against each lighting time step in the horizontal-axis. The thresholds are -16.0, -12.0, -8.0, -4.0, 0 and +4.0 K.

Table 4.3 presents the  $Tbd$  relative frequency and "more" distributions from 1Echo ( $t_0$ ) to 1CG ( $t_3$ ) for thresholds established as  $Tbd \geq -16.0 K$ , thus we are looking for cloud intensification from the negative channel differences toward the positive channel differences.

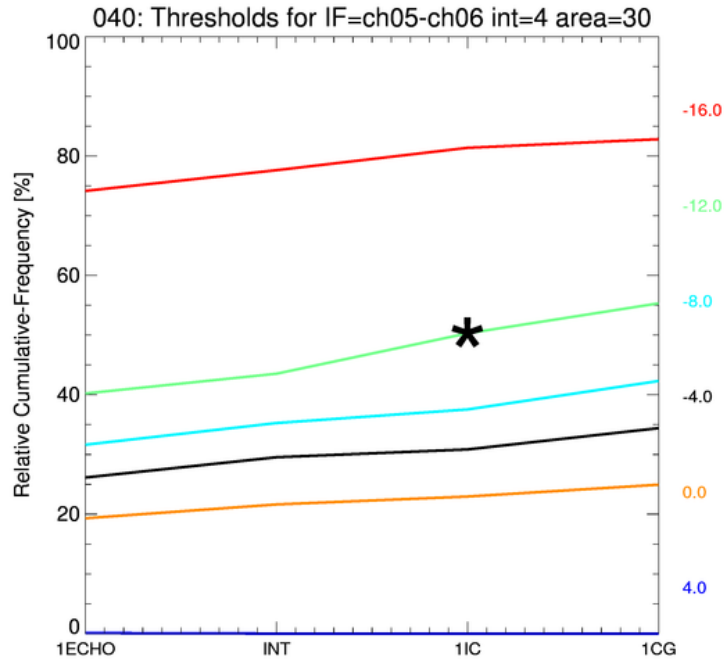


Figure 4.2 - The  $(6.2 - 7.3) \mu\text{m}$  relative *cumulative-frequency* or "more" distributions curves from *thresholds* established as  $Tbd \geq -16.0 K$  considering 40 compact thunderstorms cases studies within an evaluation area of  $30 \text{ km} \times 30 \text{ km}$  centered around respective lightning *time steps*. The threshold with greater value of *maxima derivative* is  $Tbd = -12.0 K$ , indicated with a *black asterisk*. Also see table 4.2.

Following the selection criteria for detecting a significant cloud *intensification* to be attained, table 4.2 and figure 4.2 present the values of *maxima derivative* for each *threshold* at correspondent lightning time step in the "more" distributions. Consequently, the *threshold* with greater value of *maxima derivative* is  $Tbd = -12.0 K$  at the 1IC ( $t_2$ ) *time step*.

Furthermore, linking the 1Echo ( $t_0$ ) and the 1CG ( $t_3$ ) *time steps* in figure 4.2 and table 4.3, there is a variability of pixels with values of  $Tbd \geq -12.0 K$  from 40.22 to 55.32% in the  $(6.2 - 7.3) \mu\text{m}$  *Tbd histograms* populations. This variability has an *increasing* trend in the histograms populations that can be related to an *intensification* of the convective clouds processes among the lightning time steps.

Although the  $(6.2 - 7.3) \mu m$  *interest field* can not be used like a single predictor, it can be a potential predictor regarding *intensification* of cloud processes within a subset of 4 *interest fields* in order to make the conceptual model of thunderstorm detection more accurate.

*Observation:* Figure 4.2; tables 4.2 and 4.3, indicate the *threshold*  $-12.0 K$  with *asterisk* and/or boldface at the *1IC (t2) time step*.

Table 4.2 - *Tbd thresholds* values of *maxima derivative* and correspondent lightning *time step* location in the  $(6.2 - 7.3) \mu m$  "more" distributions (see figure 4.2). The *Tbd threshold* with greater value of *maxima derivative* is  $-12.0 K$  (*asterisk*).

Class No.	Threshold (K)	Max derivative	Time step
04	-16.0	3.8	1IC (t2)
05	<b>*-12.0</b>	<b>6.8</b>	1IC (t2)
06	-8.0	4.8	1CG (t3)
07	-4.0	3.6	1CG (t3)
08	0.0	2.3	1CG (t3)
09	+4.0	0.1	Int (t1)

#### 4.1.3 10.8 $\mu m$ : *Tb histograms* and statistical values

The  $10.8 \mu m$  channel is related to cloud depth and convective processes. For more details see 3.3.4.2.

Figure 4.3 illustrates *Tb histograms* of  $10.8 \mu m$  channel for 40 cases studies within an evaluation area of  $30 km \times 30 km$  centered around respective *1Echo (t0)*, *Int (t1)*, *1IC (t2)* and *1CG (t3)* lightning *time steps*.

In the  $10.8 \mu m$  histograms, the range data has been divided into 30 classes or *bins* of  $Tb = +4.0 K$  equal interval width. The distribution of data is multimodal with *relative frequency* hump in  $Tb = +215.0$  inside the region of  $Tb \leq +235.0 K$  that can provide important information of *intensification* of cloud processes.

Following this in  $Tb = +215.0 K$ , the relative frequency is 2.00% for *1Echo* (*black* polygon), 2.15% for *Int* (*blue* polygon), 2.83% for *1IC* (*yellow* polygon) and 4.25% for *1CG* (*red* polygon). More details of the *Tb relative cumulative-frequency* distributions can be found in table 4.6.

Table 4.3 - The  $(6.2 - 7.3) \mu m$   $Tbd$  relative frequency and "more" distributions from thresholds established as  $Tbd \geq -16.0 K$ ; considering 40 thunderstorms cases studies within an evaluation area of  $30 km \times 30 km$  centered around respective lightning time steps. The  $Tbd$  threshold with greater value of maxima derivative is indicated with an asterisk (see table 4.2).

Class No.	Class mark(K)	Interval width(K)	Rel. freq.(%)	Less rel. freq.(%)
<i>1Echo (t0)</i>				
04	-16.0	+4.0	33.93	74.75
05	<b>-12.0</b>	+4.0	8.58	<b>40.22</b>
06	-8.0	+4.0	5.50	31.64
07	-4.0	+4.0	6.82	26.14
08	0.00	+4.0	19.23	19.32
09	+4.0	+4.0	0.09	0.09
<i>Int (t1)</i>				
04	-16.0	+4.0	34.09	77.62
05	<b>-12.0</b>	+4.0	8.26	<b>43.53</b>
06	-8.0	+4.0	5.73	35.27
07	-4.0	+4.0	7.91	29.54
08	0.00	+4.0	21.63	21.63
09	+4.0	+4.0	0.00	0.00
<i>1IC (t2)</i>				
04	-16.0	+4.0	31.07	81.37
05	<b>*-12.0</b>	+4.0	12.75	<b>50.30</b>
06	-8.0	+4.0	6.70	37.55
07	-4.0	+4.0	7.89	30.85
08	0.00	+4.0	22.96	22.96
09	+4.0	+4.0	0.00	0.00
<i>1CG (t3)</i>				
04	-16.0	+4.0	27.50	82.82
05	<b>-12.0</b>	+4.0	13.01	<b>55.32</b>
06	-8.0	+4.0	7.90	42.31
07	-4.0	+4.0	9.47	34.41
08	0.00	+4.0	24.94	24.94
09	+4.0	+4.0	0.00	0.00

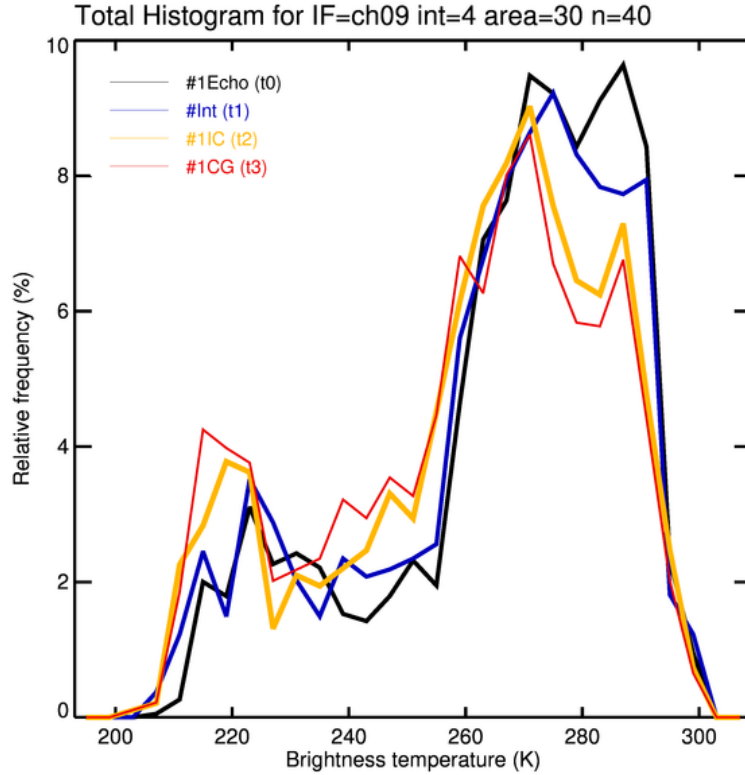


Figure 4.3 -  $T_b$  histograms of the  $10.8 \mu\text{m}$  interest field for a sample of 40 thunderstorms size within an evaluation area of  $30 \text{ km} \times 30 \text{ km}$  centered around respective lightning time steps. The histograms interval width is  $+4.0 \text{ K}$ .

The statistical values for 40 cases studies are synthesized in table 4.4, which from  $1Echo (t_0)$  to  $1CG (t_3)$  time steps are to use mean values between  $T_b = +274.34$  and  $+268.30$ , and standard deviation values between  $T_b = +25.29$  and  $+28.98 \text{ K}$ . In contrast, the values for 123 cases identified by Mecikalski et al. (2010) and mentioned in 3.3.4.2 were to use a mean of  $T_b = +242.5 \text{ K}$  and standard deviation of  $T_b = +16.79 \text{ K}$ . The statistical values between these 2 studies may differ due to the region of study and dissimilarity in considered stages of the thunderstorms cases (see 2.1), although can be noted that main statistical signals are well represented in the present study.

Also inspecting the present study's values in table 4.4 from  $1Echo (t_0)$  to  $1CG (t_3)$  can be noted a decrease greater than  $T_b = +6.0 \text{ K}$  between the mean, median and minimum values, which is representing well the trend expected in 3.3.4.2 correspondent with growing cumulus cloud-tops.

Table 4.4 - Mean, standard deviation, median and minimum values for 10.8  $\mu m$  histograms of  $Tb = +4.0 K$  interval width considering the sample of 40 thunderstorms size (see figure 4.3). These statistical values are compared above with the values of Mecikalski et al. (2010) indicated in 3.3.4.1.

Time	Step	Mean (K)	Std dev (K)	Median (K)	Min (K)
$t_0$	1Echo	+274.34	+25.29	+276.46	+208.55
$t_1$	Int	+273.13	+26.85	+275.08	+208.13
$t_2$	1IC	+269.50	+27.89	+270.81	+201.72
$t_3$	1CG	+268.30	+28.98	+269.51	+201.72

#### 4.1.4 10.8 $\mu m$ : $Tb$ thresholds and histograms populations

Figure 4.4 indicates the "less" curves from thresholds established as  $Tb \leq +235.0 K$  for 40 cases within an evaluation area of  $30 km \times 30 km$ . In the vertical-axis, the values of  $Tb$  relative cumulative-frequency (%) greater than or equal to the lower class of each threshold class have been plotted against each lightning time step in the horizontal-axis. The thresholds are +215, +195, +199, +203, +207, +211, +219, +223, +227, +231 and +235 K, respectively.

Table 4.6 presents only the 10.8  $\mu m$   $Tb$  relative frequency and "less" distributions for 1Echo ( $t_0$ ) and 1CG ( $t_3$ ) time steps for an extension reason and for thresholds established as  $Tb \leq +235.0 K$  thus we are looking for the  $Tb$  values associated to growing cumulus cloud-tops.

Following our selection criteria for detecting a significant cloud intensification to be attained, table ?? and figure 4.4 present the values of maxima derivative for each threshold at correspondent lightning time step in the "less" distributions. Consequently, the threshold with greater value of maxima derivative is +223.0 K at the 1IC ( $t_2$ ) time step.

Furthermore, linking the 1Echo ( $t_0$ ) and the 1CG ( $t_3$ ) time steps in figure 4.4 and table 4.5, there is a variability of pixels with values  $Tb \leq +223.0 K$  from 7.21 to 14.17% in the 10.8  $\mu m$   $Tb$  histograms populations. This variability has an increasing trend in the histograms populations that might be related to an intensification of the convective processes among the lightning time steps.

Although the 10.8  $\mu m$  channel can not be used like a single predictor, it can be a potential thunderstorm predictor regarding intensification of cloud processes within a subset of 4 fields in order to make the conceptual model more accurate.

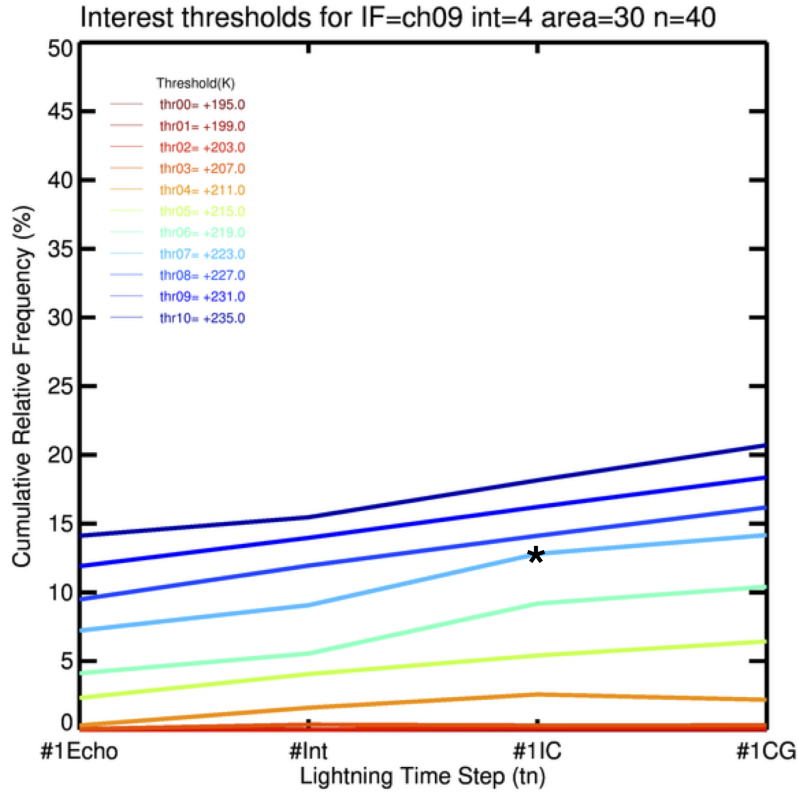


Figure 4.4 - The  $10.8 \mu\text{m}$   $T_b$  relative cumulative-frequency or "less" distributions from thresholds established as  $T_b \leq +235.0 \text{ K}$ . The  $10.8 \mu\text{m}$   $T_b$  relative cumulative-frequency distribution or "less" curve with greater value of maxima derivative plotted against each lightning time step and corresponding to a threshold with value of  $+223.0 \text{ K}$ ; considering 40 thunderstorms within an area of  $30 \text{ km} \times 30 \text{ km}$  centered around respective time steps.

Observation: Figure 4.4; tables 4.5 and 4.6, indicate the threshold  $+223.0 \text{ K}$  with asterisk and/or boldface at the  $1IC (t_2)$  time step.

#### 4.1.5 (6.2 – 10.8) $\mu\text{m}$ : $T_b$ d histograms and statistical values

The (6.2 – 10.8)  $\mu\text{m}$  interest field is related to overshooting tops and to a potential for cloud-to-ground discharge activity. For more details see 3.3.4.3.

Figure 4.5 presents  $T_b$ d histograms of the (6.2 – 10.8)  $\mu\text{m}$  interest field for 40 cases studies within an evaluation area of  $30 \text{ km} \times 30 \text{ km}$  centered around respective lightning time steps:  $1Echo (t_0)$ ,  $1Int (t_1)$ ,  $1IC (t_2)$  and  $1CG (t_3)$ .

In the histograms of (6.2 – 10.8)  $\mu\text{m}$  field, the range data has been divided into 9 class intervals of  $T_b$ d=  $+4.0 \text{ K}$  equal interval width. The distribution of the data is multimodal with relative frequency humps in  $T_b$ d=  $-50.0$ ,  $-14.0$ ,  $-10.0$  and  $-2.0$

Table 4.5 - The  $T_b$  thresholds of *maxima derivative* and correspondent lightning *time step* locations in the  $10.8 \mu\text{m}$  "more" distributions curves. The *threshold* with greater value of *maxima derivative* is  $T_b = +223.0 \text{ K}$  (*asterisk*).

Class No.	Threshold (K)	Max derivative	Time step
01	+195.0	0.00	<i>Int</i> ( $t_1$ )
02	+199.0	1.73	<i>Int</i> ( $t_1$ )
03	+203.0	1.73	<i>1IC</i> ( $t_2$ )
04	+207.0	1.73	<i>Int</i> ( $t_1$ )
05	+211.0	1.73	<i>Int</i> ( $t_1$ )
06	+215.0	1.73	<i>Int</i> ( $t_1$ )
07	+219.0	3.64	<i>1IC</i> ( $t_2$ )
08	<b>* +223.0</b>	<b>3.74</b>	<i>1IC</i> ( $t_2$ )
09	+227.0	2.46	<i>Int</i> ( $t_1$ )
10	+231.0	2.25	<i>1IC</i> ( $t_2$ )
11	+235.0	2.69	<i>1IC</i> ( $t_2$ )

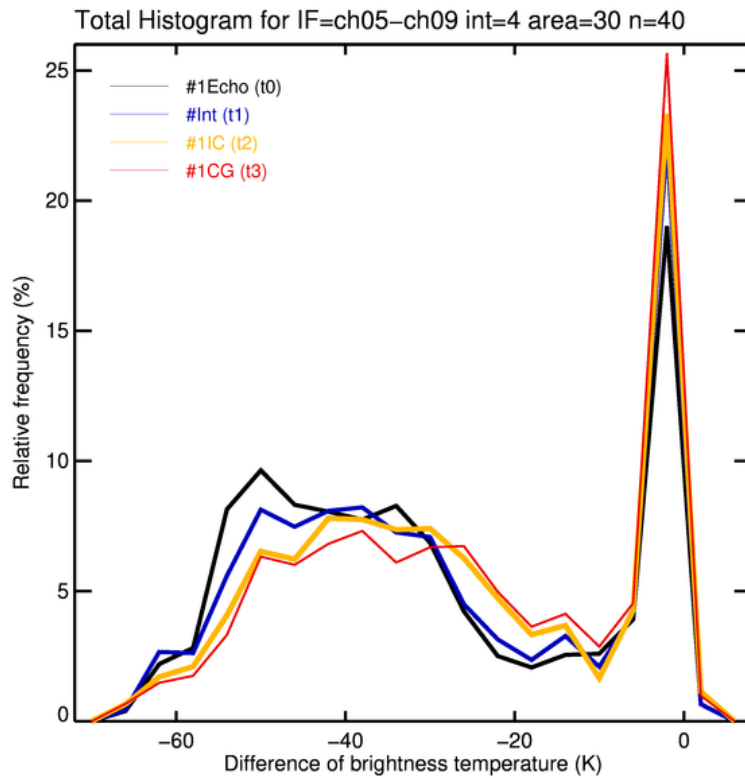


Figure 4.5 -  $T_b$  histograms of the  $(6.2 - 10.8) \mu\text{m}$  interest field for a sample of 40 thunderstorms size within an evaluation area of  $30 \text{ km} \times 30 \text{ km}$  centered around respective lightning *time steps*. The *histograms* interval width is  $+4.0 \text{ K}$ .

Table 4.6 - The  $10.8 \mu\text{m}$   $T_b$  relative frequency and "less" distributions for 1Echo and 1CG time steps, considering thresholds from  $T_b \leq +235.0 \text{ K}$  and 40 cases within an evaluation area of  $30 \text{ km} \times 30 \text{ km}$ . The  $T_b$  threshold with greater value of maxima derivative is indicated with an asterisk (see table 4.5).

Class No.	Class mark(K)	Interval width(K)	Rel. freq.(%)	Less rel. freq.(%)
<i>1Echo (t0)</i>				
01	+195.0	+4.0	0.00	0.00
02	+199.0	+4.0	0.00	0.0
03	+203.0	+4.0	0.00	0.00
04	+207.0	+4.0	0.05	0.05
05	+211.0	+4.0	0.26	0.31
06	+215.0	+4.0	2.00	2.31
07	+219.0	+4.0	1.79	4.10
08	<b>+223.0</b>	+4.0	<b>3.11</b>	<b>7.21</b>
09	+227.0	+4.0	2.26	9.47
10	+231.0	+4.0	2.42	11.89
11	+235.0	+4.0	2.21	14.10
<i>Int (t1)</i>				
08	<b>+223.0</b>	+4.0	3.52	<b>9.06</b>
<i>1IC (t2)</i>				
08	<b>*+223.0</b>	+4.0	3.62	<b>12.80</b>
<i>1CG (t3)</i>				
01	+195.0	+4.0	0.00	0.00
02	+199.0	+4.0	0.00	0.0
03	+203.0	+4.0	0.11	0.11
04	+207.0	+4.0	0.22	0.33
05	+211.0	+4.0	1.85	2.18
06	+215.0	+4.0	4.25	6.43
07	+219.0	+4.0	3.98	10.41
08	<b>+223.0</b>	+4.0	<b>3.76</b>	<b>14.17</b>
09	+227.0	+4.0	2.02	16.19
10	+231.0	+4.0	2.18	18.37
11	+235.0	+4.0	2.34	20.71

$K$ , respectively. These latter 3 humps are inside the region of the *threshold* settings established as  $Tbd \geq -14.0 K$ ; that should provide the most important information regarding *intensification* of thunderstorm processes.

Following this in  $Tbd = -14.0 K$ , the relative frequency is 2.55% for *1Echo* (black polygon), 3.28% for *Int* (blue polygon), 3.68% for *1IC* (yellow polygon) and 4.13% for *1CG* (red polygon). In  $-10.0 K$ , the relative frequency is 2.60% for *1Echo*, 2.10% for *Int*, 1.67% for *1IC* and 2.87% for *1CG*. Also in  $-2.0 K$ , the relative frequency is 19.01% for *1Echo*, 22.29% for *Int*, 23.31% for *1IC* and 25.66% for *1CG*. More details of the relative cumulative–frequency distribution can be found in table 4.3.

The statistical values for 40 cases are synthesized in table 4.7, which from *1Echo* ( $t_0$ ) to *1CG* ( $t_3$ ) *time steps* are to use mean values between  $Tbd = -30.38$  and  $-24.62 K$ , and standard deviation values between  $Tbd = -14.6$  and  $+11.27 K$ . Nevertheless, the values for 123 cases identified by Mecikalski et al. (2010) and mentioned in 3.3.4.1 were to use a mean of  $Tb = -14.6 K$  and standard deviation of  $Tb = +11.27 K$ . The statistical values obtain by these 2 studies about convective processes may differ due to the region and dissimilarity in defined stages of the thunderstorms cases (see 2.1), but can be noted that main statistical signals are well represented here.

Also inspecting the present study’s values in table 4.7 from *1Echo* ( $t_0$ ) to *1CG* ( $t_3$ ), there is an increase greater than  $+5.0 K$  in the mean and median values. These channel differences become smaller accordingly with the trend expected in 3.3.4.3, correspondent with convective cloud-tops that are at or above the tropopause (overshooting tops). However not following this expected trend, there is not significant change between the minimum values (less than  $Tbd = +1.0 K$ ) from *1Echo* ( $t_0$ ) to *1CG* ( $t_3$ ) *time steps*.

Table 4.7 - Mean, standard deviation, median and minimum values for the (6.2 – 10.8)  $\mu m$  histograms of  $Tbd = +4.0 K$  interval width considering the sample of 40 thunderstorms size (see figure 4.5). These statistical values are compared above with the values of Mecikalski et al. (2010) indicated in 3.3.4.1.

<b>Time</b>	<b>Step</b>	<b>Mean (K)</b>	<b>Std dev (K)</b>	<b>Median (K)</b>	<b>Min (K)</b>
$t_0$	<i>1Echo</i>	-30.38	+19.79	-34.38	-65.97
$t_1$	<i>Int</i>	-28.35	+20.02	-32.39	-66.29
$t_2$	<i>1IC</i>	-26.33	+19.35	-28.94	-66.55
$t_3$	<i>1CG</i>	-24.62	+19.32	-26.06	-66.55

#### 4.1.6 (6.2 – 10.8) $\mu\text{m}$ : *Tbd* thresholds and histograms populations

Figure 4.6 indicates the "more" curves from *thresholds* established as  $Tbd \geq -14.0$  K for 40 cases studies within an evaluation area of  $30 \text{ km} \times 30 \text{ km}$ . In the vertical-axis, the values of *Tbd relative cumulative-frequency* (%) greater than or equal to the lower class of each *threshold* class have been plotted against each lighting *time step* in the horizontal-axis. The *thresholds* are  $Tbd = -14.0, -10.0, -6.0, -2.0, +2.0$  and  $+6.0$  K, respectively.

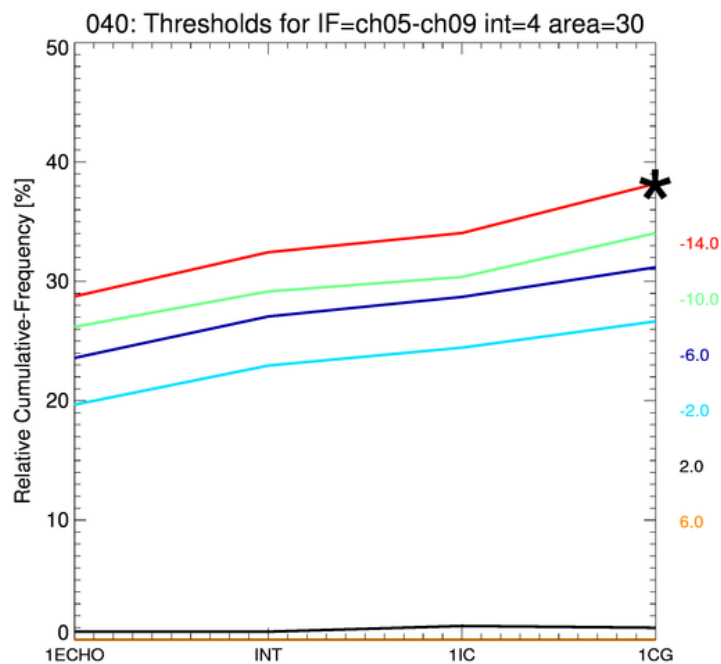


Figure 4.6 - The (6.2 – 10.8)  $\mu\text{m}$  *Tbd* relative cumulative-frequency or "more" distributions curves from *thresholds* established as  $Tbd \geq -14.0$  K considering 40 thunderstorms cases studies within an evaluation area of  $30 \text{ km} \times 30 \text{ km}$  centered around respective lightning *time steps*. The *thresholds* with greater value of *maxima derivative* is  $Tbd = -14.0$  K at the 1CG ( $t_3$ ) *time step*, indicated with a *black asterisk*. Also see table 4.8.

Table 4.9 presents the *Tbd* relative frequency and "more" distributions curves from 1Echo ( $t_0$ ) to 1CG ( $t_3$ ) *time steps* for *thresholds* established as  $Tbd \geq -14.0$  K, thus we are looking for *intensification* of electrification processes toward the positive channel differences.

Following the selection criteria for detecting a significant *intensification* of electrification processes to be attained, table 4.8 and figure 4.6 present the values of *maxima derivative* for each *threshold* at correspondent lightning time step in the "more" distributions curves. Consequently, the *threshold* with greater value of *maxima derivative* is -14.0 K at the 1CG (*t3*) time step.

Furthermore, linking the 1Echo (*t0*) and the 1CG (*t3*) time steps in figure 4.6 and table 4.9, there is a variability of pixels with values of  $Tbd \geq -14.0$  K from 28.74 to 38.18% in the (6.2 – 10.8)  $\mu m$  histograms populations. This variability has an *increasing* trend in the histograms populations that might be related to an *intensification* of electrification processes among the lightning time steps.

Although the (6.2 – 10.8)  $\mu m$  interest field can not be used like a single predictor, it can be a potential predictor regarding *intensification* of electrification processes within a subset of 4 interest fields in order to make the conceptual model of thunderstorm detection more accurate.

*Observation:* figure 4.6; tables 4.8 and 4.9, indicate the *threshold* -12.0 K with *asterisk* and/or boldface at the 1CG (*t3*) time step.

Table 4.8 - *Tbd thresholds* values of *maxima derivative* and correspondent lightning time step location in the (6.2 – 10.8)  $\mu m$  "more" distributions (see figure 4.6). The *Tbd threshold* with greater value of *maxima derivative* is -14.0 K (*asterisk*).

Class No.	Threshold (K)	Max derivative	Time step
15	<b>*-14.0</b>	<b>4.1</b>	1CG
16	-10.0	3.7	1CG
17	-6.0	3.5	Int
18	-2.0	3.3	Int
19	+2.0	0.5	1IC
20	+6.0	0.0	Int

Table 4.9 - The (6.2 – 10.8)  $\mu m$  *Tbd* relative frequency and "more" distributions from thresholds established as  $Tbd \geq -14.0 K$ ; considering 40 thunderstorms cases studies within an evaluation area of  $30 km \times 30 km$  centered around respective lightning *time steps*. The *Tbd* threshold with greater value of *maxima derivative* is indicated with an *asterisk* (see table 4.8).

Class No.	Class mark(K)	Interval width(K)	Rel. freq.(%)	Less rel. freq.(%)
<i>1Echo (t0)</i>				
15	<b>-14.0</b>	+4.0	2.55	<b>28.74</b>
16	-10.0	+4.0	2.60	26.19
17	-6.0	+4.0	3.92	23.59
18	-2.0	+4.0	19.01	19.67
19	+2.0	+4.0	0.66	0.66
20	+6.0	+4.0	0.00	0.00
<i>Int (t1)</i>				
15	<b>-14.0</b>	+4.0	3.28	<b>32.44</b>
16	-10.0	+4.0	2.10	29.16
17	-6.0	+4.0	4.11	27.06
18	-2.0	+4.0	22.29	22.95
19	+2.0	+4.0	0.66	0.66
20	+6.0	+4.0	0.00	00.00
<i>1IC (t2)</i>				
15	<b>-14.0</b>	+4.0	3.68	<b>34.05</b>
16	-10.0	+4.0	1.67	30.37
17	-6.0	+4.0	4.25	28.70
18	-2.0	+4.0	23.31	24.45
19	+2.0	+4.0	1.14	1.14
20	+6.0	+4.0	0.00	0.00
<i>1CG (t3)</i>				
15	<b>*-14.0</b>	+4.0	4.13	<b>38.18</b>
16	-10.0	+4.0	2.87	34.05
17	-6.0	+4.0	4.53	31.18
18	-2.0	+4.0	25.66	26.65
19	+2.0	+4.0	0.99	0.99
20	+6.0	+4.0	0.00	0.00

#### 4.1.7 Trispectral: $Tbd$ histograms and statistical values

The  $(8.7 - 10.8) - (10.8 - 12.0)$  or *trispectral* interest field is related to glaciation in convective clouds. For more details see 3.3.4.4.

Figure 4.7 illustrates  $Tbd$  histograms of the *trispectral* interest field for 40 cases studies within an evaluation area of  $30\text{ km} \times 30\text{ km}$  centered around the 4 lightning *time steps*: 1Echo ( $t_0$ ) in *black* - first echo with any value of reflectivity above the reflectivity noise level; Int ( $t_1$ ) in *blue* - intermediate stage between first reflectivity echo and first intra-cloud lightning flash, 1IC ( $t_2$ ) in *yellow* - first intra-cloud lightning flash and 1CG ( $t_3$ ) in *red* - first cloud-to-ground lightning flash.

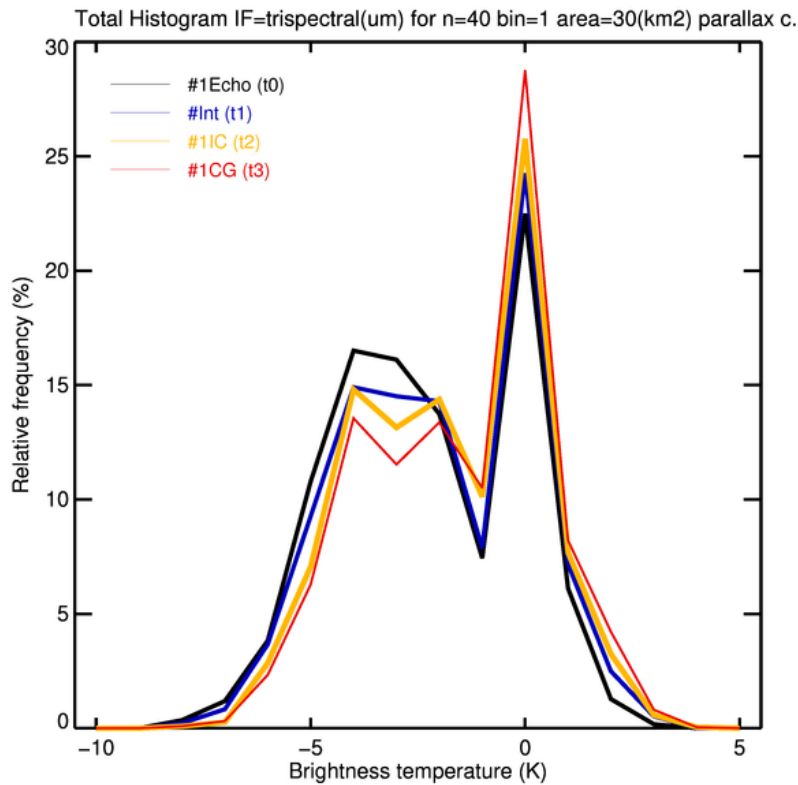


Figure 4.7 -  $Tbd$  histograms of the *trispectral* interest field for a sample of 40 thunderstorms size within an evaluation area of  $30\text{ km} \times 30\text{ km}$  centered around respective lightning *time steps*. The *histograms* interval width is  $+4.0\text{ K}$ .

In the  $(8.7 - 10.8) - (10.8 - 12.0)\ \mu\text{m}$  histograms, the  $Tbd$  range data has been divided into 16 classes or *bins* of  $Tb = +1.0\text{ K}$  equal interval width. The distribution of data is multimodal with *relative frequency* hump in  $Tbd =$  in  $4.0, -2.0$  and  $0\text{ K}$ , respectively. The latter hump is inside the region of the *thresholds* settings established

as  $Tbd \geq 0 K$  that can provide significant information regarding *intensification* of glaciation in convective clouds.

Following this in  $Tbd= 0 K$ , the relative frequency is 30.07% for 1*Echo* (*black* polygon), 34.44% for *Int* (*blue* polygon), 37.29% for 1*IC* (*yellow* polygon) and 42.02% for 1*CG* (*red* polygon). More details of the *Tb relative cumulative-frequency* distributions polygons can be found in table 4.12.

The statistical values for 40 cases are synthesized in table 4.10, which from 1*Echo* ( $t_0$ ) to 1*CG* ( $t_3$ ) lightning *time steps* are to use mean values between  $Tbd= -2.27$  and  $-1.55 K$ , and standard deviation values between  $Tbd= +2.07$  and  $+2.14 K$ . In contrast, the statistical values for 123 cases identified by the study of Mecikalski et al. (2010) and mentioned in 3.3.4.2, were to use a mean of  $Tbd= -0.6 K$  and standard deviation of  $Tbd= +1.9 K$ . These statistical values may differ due to the region and dissimilarity in defined stages of the thunderstorms cases (see 2.1), but can be noted that main statistical signals are well represented the present study.

Also inspecting the present study's values in table 4.10 from 1*Echo* ( $t_0$ ) to 1*CG* ( $t_3$ ) lightning *time steps*, can be noted an increase not greater than  $Tbd= +1.0 K$  in the mean, median and minimum values. But for all these values, the channel differences become slightly positive representing well the trend expected in 3.3.4.4, that is, a positive trend of  $Tbd$  is correspondent with cloud-top glaciation.

Table 4.10 - Mean, standard deviation, median and minimum values for the *trispectral histograms* of  $Tbd= +1.0 K$  interval width considering the sample of 40 thunderstorms size (see figure 4.7). These statistical values are compared above with the values of Mecikalski et al. (2010) indicated in 3.3.4.1.

Time	Step	Mean (K)	Std dev (K)	Median (K)	Min (K)
$t_0$	1 <i>Echo</i>	-2.27	+2.11	-2.41	-8.36
$t_1$	<i>Int</i>	-2.02	+2.14	-2.05	-7.94
$t_2$	1 <i>IC</i>	-1.75	+2.06	-1.65	-7.62
$t_3$	1 <i>CG</i>	<b>-1.55</b>	+2.07	-1.29	<b>-7.62</b>

#### 4.1.8 *Trispectral: Tbd thresholds and histograms populations*

Figure 4.8 illustrates the "more" curves from *thresholds* established as  $Tbd \geq 0 K$  for 40 cases within an evaluation area of  $30 km \times 30 km$ . In the vertical-axis, the values of *Tbd relative cumulative-frequency* (%) greater than or equal to the lower class of each *threshold* class have been plotted against each lightning *time step*

in the horizontal-axis. The *threshold* are 0, +1.0, +2.0 +3.0, +4.0 and +5.0 K; respectively. The last 2 *thresholds* present negligible slope.

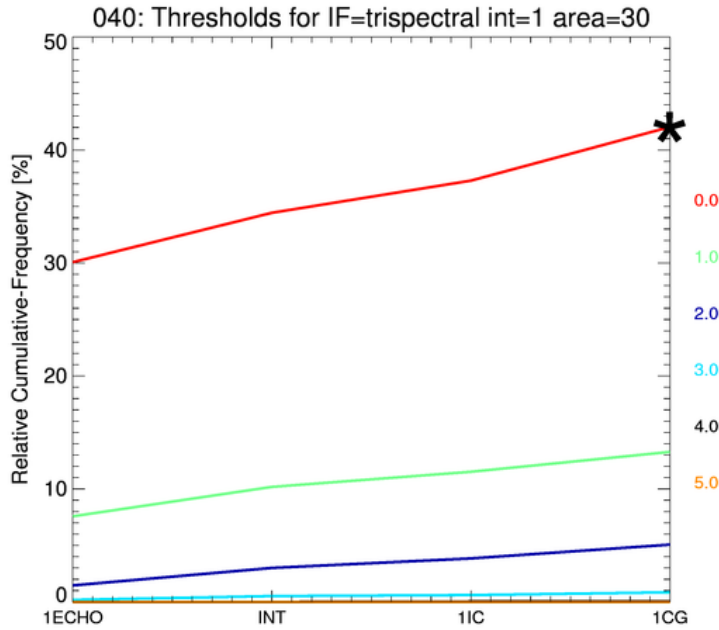


Figure 4.8 - *Trispectral Tbd relative cumulative-frequency* or "more" distributions curves from *thresholds* established as  $Tbd \geq 0 K$ ; considering 40 thunderstorms cases studies within an evaluation area of  $30 km \times 30 km$  centered around respective lightning *time steps*. The *Tbd threshold* with greater value of *maxima derivative* is indicated with a *black asterisk* (see table 4.11).

Table 4.12 presents *Tbd relative frequency* and "more" distributions curves from 1Echo ( $t_0$ ) to 1CG ( $t_3$ ) for *thresholds* established as  $Tbd \geq 0 K$ , thus from  $Tbd=0 K$  toward the positive channel differences we are looking for *intensification* of glaciation in convective clouds.

Following our selection criteria for detecting a significant cloud *intensification* of glaciation processes to be attained, table 4.11 and figure ?? present the values of *maxima derivative* for each *threshold* at correspondent lightning time step in the "more" distributions curves. Consequently, the *threshold* with greater value of *maxima derivative* is  $Tbd=0 K$  at the 1CG ( $t_3$ ) *time step*.

Table 4.11 - *Tbd thresholds* values of *maxima derivative* and correspondent lightning *time step* location in the *trispectral "more"* distributions (see figure 4.8). The *Tbd threshold* with greater value of *maxima derivative* is 0 K (*asterisk*).

Class No.	Threshold (K)	Max derivative	Time step
00	<b>*0.0</b>	<b>4.8</b>	1CG (t3)
01	+1.0	2.6	Int (t1)
02	+2.0	1.5	Int (t1)
03	+3.0	0.3	Int (t1)
04	+4.0	0.0	1IC (t2)
05	+5.0	0.0	Int (t1)

Furthermore, linking the 1Echo (t0) and the 1CG (t3) *time steps* in figure 4.8 and table 4.12, there is a variability of pixels with values  $Tbd \geq 0 K$  from 30.07 to 42.04% in the *trispectral histograms* populations. This variability has an *increasing* trend in the histograms populations that can be related to an *intensification* of the glaciation process among the lightning time steps.

Although the *trispectral interest field* can not be used like a single predictor, it can be a potential predictor regarding *intensification* of cloud glaciation processes within a subset of 4 *interest fields* in order to make the conceptual model of thunderstorm detection more accurate.

Again the figure 4.8; tables 4.11 and 4.12, indicate the *threshold 0 K* with *asterisk* and/or boldface at the 1CG (t3) lightning *time step*.

As mentioned previously, considering a sample of 40 cases studies, the analyses of the derived information from each *IR interest field* were presented above to gain insight into a representative behavior of the thunderstorm life cycle and its early electrification process. The resulting parameters for a conceptual model of thunderstorm detection using the 4 *IR interest fields* are outlined in section 4.2.

Table 4.12 - The *trispectral Tbd relative frequency* and "more" distributions from *thresholds* established as  $Tbd \geq 0 K$ ; considering 40 thunderstorms cases studies within an evaluation area of  $30 km \times 30 km$  centered around respective lightning *time steps*. The *Tbd threshold* with greater value of *maxima derivative* is indicated with an *asterisk* (see table 4.11).

Class No.	Class mark(K)	Interval width(K)	Rel. freq.(%)	Less rel. freq.(%)
<i>1Echo (t0)</i>				
11	<b>0.00</b>	+1.0	22.49	<b>30.07</b>
12	+1.0	+1.0	6.12	7.58
13	+2.0	+1.0	1.28	1.46
14	+3.0	+1.0	0.18	0.18
15	+4.0	+1.0	0.00	0.00
16	+5.0	+1.0	0.00	0.00
<i>Int (t1)</i>				
11	<b>0.00</b>	+1.0	24.26	<b>34.44</b>
12	+1.0	+1.0	7.17	10.18
13	+2.0	+1.0	2.49	3.01
14	+3.0	+1.0	0.52	0.52
15	+4.0	+1.0	0.00	0.00
16	+5.0	+1.0	0.00	00.00
<i>1IC (t2)</i>				
11	<b>0.00</b>	+1.0	25.77	<b>37.29</b>
12	+1.0	+1.0	7.67	11.52
13	+2.0	+1.0	3.24	3.85
14	+3.0	+1.0	0.57	0.61
15	+4.0	+1.0	0.04	0.04
16	+5.0	+1.0	0.00	0.00
<i>1CG (t3)</i>				
11	<b>*0.00</b>	+1.0	28.76	<b>42.04</b>
12	+1.0	+1.0	8.21	13.28
13	+2.0	+1.0	4.22	5.07
14	+3.0	+1.0	0.81	0.85
15	+4.0	+1.0	0.04	0.44
16	+5.0	+1.0	0.00	0.00

## 4.2 Thunderstorm detection using 4 IR interest fields imagery

The resulting predictors for the conceptual model of thunderstorm detection using *IR interest fields* in a sample of 40 cases studies; taking as potential information the *Tb (Tbd) histograms* in each lightning *time step*, *Tb (Tbd) threshold* correspondent to the "less" ("more") curve with greater value of *maxima derivative* and the variability between *Tb (Tbd) histograms* populations based on a *Tb (Tbd) threshold*, are summarized in figure 4.9.

The 4 predictors for the nowcasting tool were stratified according to 4 *interest fields*:  $(6.2 - 7.3) \mu m$ ;  $10.8 \mu m$ ,  $(6.2 - 10.8) \mu m$  and  $(8.7 - 10.8) - (10.8 - 12.0) \mu m$ . That is, separate parameters were calculated to predict cloud and electrification processes, and although each one of them can not be used like a single predictant of thunderstorm processes, considering all together will make the conceptual model more accurate.

The parameters for the 4 predictors at each lightning *time step* are indicated below according to the order in which were selected and calculated in figure 4.9.

- **Mean** ( $K$ ): *Tb (Tbd)* pixel average value in the *Tb (Tbd) histogram*.
- **Std dev** ( $K$ ): Standard deviation in the *Tb (Tbd) histogram*.
- **Median** ( $K$ ): Middle *Tb (Tbd)* pixel value or the arithmetic mean of the two middle pixels values in the *Tb (Tbd) histogram* population.
- **Minimum** ( $K$ ): Smallest *Tb (Tbd)* pixel value in the *Tb (Tbd) histogram*.
- **Threshold** ( $K$ ): *Tb (Tbd) threshold* with greater value of *maxima derivative* for detecting the most significant *intensification* of cloud and electrification processes that can be attained.
- **Relative cumulative-frequency** (%): Total frequency of all pixels with values *greater* (or *lower*) than the *Tb (Tbd) threshold*.
- **Maxima derivative** (\*): Lightning *time step* location of the greater value of *maxima derivative* for each *Tb (Tbd) threshold*.

*Observation*: for each thunderstorm predictor, the *range* value (the difference between the largest and smallest number) and the *average* value allow a rapid analysis of corresponding *nowcasting* parameters; are indicated in figure 4.9.

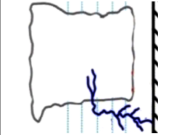
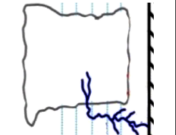
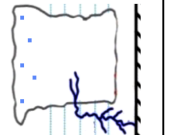
Predictor	Time Step	Mean (K)	Std dev (K)	Median (K)	Min (K)	Threshold (K)	Cum-Frequency (%)	Max derivative
 Predictor 1 cloud depth	<b>Ch05-Ch06</b>	Range 2,03 Average -11,45	Range 0,21 Average 7,47	Range 2,74 Average -14,39	Range -0,44 Average -25,29	Tbd > Thr	Range 15,10 Average 47,34	
	t0	-12,47	7,47	-15,64	-25,09		40,22	
	t1	-11,81	7,60	-15,08	-25,53	<b>-12,00</b>	43,53	
	t2	-11,09	7,39	-13,92	-25,27		50,30	*
	t3	-10,44	7,43	-12,90	-25,27		55,32	
 Predictor 2 cloud depth	<b>Ch09</b>	Range -6,04 Average 271,32	Range 3,69 Average 27,25	Range -6,95 Average 272,965	Range -6,83 Average 205,03	Tb < Thr	Range 16,43 Average 43,17	
	t0	274,34	25,29	276,46	208,55		34,80	
	t1	273,13	26,85	275,08	208,13	<b>263,00</b>	39,36	
	t2	269,50	27,89	270,81	201,72		47,28	*
	t3	268,30	28,98	269,51	201,72		51,23	
 Predictor 3 cloud depth	<b>Ch05-Ch09</b>	Range -5,76 Average -27,42	Range 0,70 Average 19,62	Range -8,32 Average -30,44	Range 0,58 Average -66,34	Tbd > Thr	Range 9,44 Average 33,35	
	t0	-30,38	19,79	-34,38	-65,97		28,74	
	t1	-28,35	20,02	-32,39	-66,29	<b>-14,00</b>	32,44	
	t2	-26,33	19,35	-28,94	-66,55		34,05	
	t3	-24,62	19,32	-26,06	-66,55		38,18	*
 Predictor 4 glaciation	<b>Trispectral</b>	Range -0,72 Average -1,90	Range 0,08 Average 2,10	Range -1,12 Average -1,85	Range -0,74 Average -7,89	Tbd > Thr	Range 11,97 Average 35,96	
	t0	-2,27	2,11	-2,41	-8,36		30,07	
	t1	-2,02	2,14	-2,05	-7,94	<b>0,00</b>	34,44	
	t2	-1,75	2,06	-1,65	-7,62		37,29	
	t3	-1,55	2,07	-1,29	-7,62		42,04	*

Figure 4.9 - *Thunderstorm predictors* using *SEVIRI* infrared (*IR*) fields for a nowcasting tool as follows: **Predictor 1 - Ch05-Ch06:** (6.2 – 7.3)  $\mu\text{m}$ ; **Predictor 2 - Ch09:** 10.8  $\mu\text{m}$ , **Predictor 3 - Ch05-Ch09:** (6.2 – 10.8)  $\mu\text{m}$  and **Predictor 4 - Trispectral:** (8.7 – 10.8) – (10.8 – 12.0)  $\mu\text{m}$ . The relation (Tbd >Thr) is for a "less" distribution with greater value of *maxima derivative*; on the contrary way is for (Tbd <Thr). The lightning *time step* location of the greater value of *maxima derivative* is indicated with *asterisk*. The *range* and *average* values allows a rapid analysis of corresponding *nowcasting* parameters.

## 5 Verification of the conceptual model of thunderstorm detection

According to Wilks (1995)'s verification, here will be taken the reference to categorical forecasts of discrete predictands for the verification of the conceptual model of thunderstorm detection. Categorical means that the forecasts consist of a flat statement that only one set of possible events will occur and discrete predictand is an observable variable that takes only one of a finite set of possible values.

The categorical forecasts of discrete predictands are displayed in forecasts and observations contingency table. Then, analyzing the correspondence between the predictions and observations values of this contingency table can help in the assessment of strengths and deficiencies of our conceptual model of thunderstorm detection.

As defined in Wilks (1995) and Mecikalski et al. (2008), the 3 scalar measures obtained from the contingency table, or *POD*, *FAR* and *TS*, are used here to evaluate the conceptual model of thunderstorm detection:

The first scalar measure, or Probability Of Detection (*POD*), is the fraction of occasions when the prediction of *IC* and/or *CG* lightning *time steps* occurred in which it were also predicted to occur, relative to all observations of *IC* and/or *CG* lightning *time steps*. The *POD* for perfect forecast is one and the worst *POD* is zero.

The second scalar measure, or False Alarm Ratio (*FAR*), is the fraction of predicted *IC* and/or *CG* lightning *time steps* that turned out to be incorrect, relative to all *IC* and/or *CG* lightning *time steps* predicted. The perfect *FAR* is zero and the worst *FAR* is one.

The third scalar measure, or Threat Score (*TS*), is the critical success index that represents the number of correct predictions of *IC* and/or *CG* lightning *time steps* divided by the total number of occasions in which the lightning *time steps* were predicted and/or observed.

These 3 scalar measures are calculated as  $POD = a/(a+c)$ ,  $FAR = b/(a+b)$  and  $TS = a/(a+b+c)$ ; where  $n$  is the total number of predicted/observed lightning *time steps* pairs in a data set, or  $n = a+b+c+d$ , arranged in 4 possible combinations of the contingency table:  $a$ ;  $b$ ,  $c$  and  $d$ . The 4 combinations are itemized below:

- **a:** occasions when a lighting *time step* was observed and was also predicted to occur. A lighting *time step* was observed through lightning data accumulated every 15 *min* as *1IC*, *1IC* and *1CG*, or *1CG* at evaluation areas of 30 *km* × 30 *km* within the CHUVA-Vale region. A lighting *time step* was predicted to occur through our nowcasting tool index as *1IC* or *1CG* at the same evaluation areas.
- **b:** occasions when a lighting *time step* was not observed but it was predicted to occur. A lighting *time step* was not observed if the lightning data accumulated every 15 *min* was null at evaluation areas of 30 *km* × 30 *km* within the CHUVA-Vale region. A lighting *time step* was predicted to occur through our nowcasting tool index as *1IC* or *1CG* at the same evaluation areas.
- **c:** occasions when a lighting *time step* was observed but it was not predicted to occur. A lighting *time step* was observed through lightning data accumulated every 15 *min* as *1IC*, *1IC* and *1CG*, or *1CG* at evaluation areas of 30 *km* × 30 *km* within the CHUVA-Vale region. A lighting *time step* was not predicted to occur if our nowcasting tool index was null at the same evaluation areas.
- **d:** occasions when the forecast lighting *time step* was not observed and was also not predicted to occur. A lighting *time step* was not observed if the lightning data accumulated every 15 *min* was null at evaluation areas of 30 *km* × 30 *km* within the CHUVA-Vale region. A lighting *time step* was not predicted to occur if our nowcasting tool index was null at the same evaluation areas.

With reference to the lighting *time steps* occurred, the observed lightning data from the BrasilDAT network were accumulated every 15 *min* at evaluation areas of 30 *km* × 30 *km* within the CHUVA-Vale region. For example, based on satellite observations at 18:00, 18:15 and 18:30; the *IC* and *CG* lightning flashes were accumulated from 18:00 to 18:14 and from 18:15 to 18:29 for the comparison between the lighting *time steps* observed and the lighting *time steps* predicted at 18:00 and 18:15, respectively, and so on.

Following the example above, 2 independent verification tests were implemented for the verification of the conceptual model of thunderstorm detection every 15 *min* cycle during 2-days with significant lightning activity, at evaluation areas of 30 *km* × 30 *km* within the CHUVA-Vale region.

The first independent verification test determined which *interest field* presents more and least association between brightness temperature and lighting detection at evaluation areas of 30 *km* × 30 *km*. This test was implemented using a comparison among the lightning data occurred and the lightning data predicted by our

conceptual model, that is, the *IC* and/or *CG* flashes from the BrasilDAT network within the CHUVA-Vale region were accumulated every 15 *min* and compared with corresponding lighting *time steps* model *indices*.

Regarding the lighting *time steps* model *indices*, a lighting *time steps* model *index* was computed by an interest field as follows: if the value of *relative cumulative-frequency* at an evaluation area of 30 *km* × 30 *km* is less than the model's 1*Echo t0 relative cumulative-frequency*, the *index* is equal to 0 or no lightning.

If the value of *relative cumulative-frequency* at an evaluation area of 30 *km* × 30 *km* is greater than the model's 1*Echo t0 relative cumulative-frequency*; but less than the model's 1*Int t1 relative cumulative-frequency*, the *index* is equal to 1. If the value is greater than the model's 1*Int t1 relative cumulative-frequency*, but less than the model's 1*IC t2 relative cumulative-frequency*, the *index* is 2. If the value is greater than the model's 1*IC t2 relative cumulative-frequency*; but less than the model's 1*CG t3 relative cumulative-frequency*, the *index* is 3. And if the value of *relative cumulative-frequency* at an evaluation area of 30 *km* × 30 *km* is greater than the model's 1*CG t3 relative cumulative-frequency*, the *index* is 4.

Regarding the comparison among the lightning data occurred and the lightning data predicted by our conceptual model during 2-days with significant lightning activity within the CHUVA-Vale region, see tables 5.1 and 5.2 for (6.2 – 7.3)  $\mu m$  channel difference's verification; tables 5.3 and 5.4 for 10.8  $\mu m$  channel verification; tables 5.5 and 5.6 for (6.2 – 10.8)  $\mu m$  channel difference's verification, and tables 5.7 and 5.8 for *trispectral* channel difference's verification.

In tables from 5.1 to 5.8 are presented values of *POD* greater than 0.70 and values of *FAR* less than 0.50 for the first independent verification of 4 *interest fields*. It is estimated that in a future work, our conceptual model's *POD* may increase and the *FAR* may decrease by implementing the first independent verification for more than 2-days of significant lightning activity in the CHUVA-Vale region.

The second independent verification test involved skill determination of all 4 *interest fields* at the same evaluation areas of 30 *km* × 30 *km* within the CHUVA-Vale region selected for the first verification test. For example, if at an evaluation area, our conceptual model indicated *index* 4 in all 4 *interest fields*, or predicted the *CG t3's lightning step*, then the *index sum* will be equal to 16. In other example, if at an evaluation area, our conceptual model indicated *index* 0 in all 4 *interest fields*, or predicted no lightning, then the *index sum* will be equal to 0.

Following the examples above, the *index sum* is the total sum of each *interest field's index*; where each *index* can take values from 4 to 0 and the *index sum* can take values from 16 to 0. See the contingency table 5.9 for the conceptual model's *index sum* of 4 *interest fields* together.

Also in table 5.9 is indicated that our conceptual model has a higher probability of lightning detection for *index sums* between 16 and 12 due to the higher *POD* and lower *FAR*. Additionally, our conceptual model has a lower probability of lightning detection for *index sums* between 8 and 4 because of the lower *POD* and higher *FAR*. The *index sums* from 3 to 0 were discarded because of the not representative values of *POD* and *FAR* obtained.

Moreover, in table 5.10 is presented the contingency table for **intervals** of *index sums*, that is, the **interval** of *index sums* from 16 to 12; the **interval** of *index sums* from 12 to 8, and the **interval** of *index sums* from 8 to 4.

Again the results in table 5.10 indicated that the conceptual model has a higher probability of lightning detection for the **interval** of *index sums* from 16 to 12 because of the higher *POD* and lower *FAR*. Also the results indicated that our conceptual model has a lower probability of lightning detection for the **interval** of *index sums* from 8 to 4 because of the lower *POD* and higher *FAR*. The **interval** from 4 to 0 was discarded because not representative values of *POD* and *FAR*.

Table 5.1 - The  $(6.2 - 7.3) \mu m$  channel difference's verification using lightning data from BrasilDAT network accumulated every 15 *min* and 15 *min*-satellite images during 1-day with significant lightning activity (January 17, 2012) at 41 evaluation areas of  $30 km \times 30 km$  within the CHUVA-Vale region.

Ch05-Ch06: $(6.2 - 7.3) \mu m$ — [15 <i>min</i> ] — 120117								
<b>Time</b>	<b>POD</b>	<b>FAR</b>	<b>TS</b>	<i>a</i>	<i>b</i>	<i>c</i>	<i>d</i>	<i>n</i>
0 : 00	0.92	0.50	0.48	11	11	1	18	41
0 : 15	0.82	0.59	0.38	9	13	2	17	41
0 : 30	0.88	0.70	0.29	7	16	1	17	41
0 : 45	1.00	0.80	0.20	5	20	0	16	41
14 : 00	1.00	0.95	0.05	1	20	0	20	41
14 : 15	0.04	0.00	0.04	1	0	23	17	41
14 : 30	0.50	0.91	0.08	2	21	2	16	41
14 : 45	0.50	0.88	0.11	3	22	3	13	41
15 : 00	0.60	0.74	0.22	6	17	4	14	41
15 : 15	0.87	0.35	0.58	23	13	3	2	41
15 : 30	0.44	0.83	0.14	4	19	5	13	41
15 : 45	0.57	0.62	0.30	8	13	6	14	41
16 : 00	0.43	0.67	0.23	6	12	8	15	41
16 : 15	0.56	0.47	0.38	9	8	8	17	41
16 : 30	0.80	0.37	0.55	12	17	3	19	41
16 : 45	0.90	0.55	0.43	9	11	1	20	41
17 : 00	0.86	0.48	0.48	12	11	2	16	41
17 : 15	0.81	0.46	0.48	13	11	3	14	41
17 : 30	0.86	0.48	0.48	14	13	2	12	41
17 : 45	0.00	1.00	0.00	0	26	6	9	41
18 : 00	0.76	0.45	0.47	16	13	5	7	41
18 : 15	0.70	0.41	0.47	16	11	7	7	41
18 : 30	0.88	0.48	0.48	15	14	2	10	41
18 : 45	0.63	0.57	0.34	12	16	7	6	41
19 : 00	0.82	0.36	0.56	18	10	4	9	41
19 : 15	0.77	0.38	0.53	20	12	6	3	41
19 : 30	0.86	0.42	0.53	19	14	3	5	41
19 : 45	0.71	0.55	0.38	15	18	6	2	41
20 : 00	0.81	0.53	0.43	17	19	4	1	41
20 : 15	0.88	0.36	0.59	23	13	3	2	41
20 : 30	0.89	0.32	0.63	25	12	3	1	41
20 : 45	0.90	0.49	0.49	19	18	2	2	41
<i>Average</i>	<b>0.72</b>	<b>0.55</b>	<b>0.37</b>	-	-	-	-	-

Table 5.2 - The  $(6.2 - 7.3) \mu m$  channel difference's verification using lightning data from BrasilDAT network accumulated every 15 *min* and 15 *min*-satellite images during 1-day with significant lightning activity (March 13, 2012) at 41 evaluation areas of  $30 km \times 30 km$  within the CHUVA-Vale region.

Ch05-Ch06: $(6.2 - 7.3) \mu m$ — [15 <i>min</i> ] — 120313								
<b>Time</b>	<b>POD</b>	<b>FAR</b>	<b>TS</b>	<i>a</i>	<i>b</i>	<i>c</i>	<i>d</i>	<i>n</i>
18 : 00	0.76	0.27	0.59	16	6	5	14	41
18 : 15	0.80	0.33	0.57	16	8	4	13	41
18 : 30	0.81	0.29	0.61	17	7	4	13	41
18 : 45	0.76	0.41	0.50	13	9	4	15	41
19 : 00	0.81	0.41	0.52	13	9	3	16	41
19 : 15	0.92	0.56	0.42	11	14	1	15	41
19 : 30	0.67	0.52	0.38	10	11	5	15	41
19 : 45	0.88	0.38	0.58	15	9	2	15	41
20 : 00	0.73	0.50	0.42	11	11	4	15	41
20 : 15	0.50	0.68	0.24	7	15	7	12	41
20 : 30	0.58	0.71	0.24	7	17	5	12	41
20 : 45	0.58	0.68	0.26	7	15	5	14	41
<i>Average</i>	<b>0.73</b>	<b>0.48</b>	<b>0.45</b>	-	-	-	-	-

Table 5.3 - The  $10.8 \mu m$  channel's verification using lightning data from BrasilDAT network accumulated every 15 *min* and 15 *min*-satellite images during 1-day with significant lightning activity (January 17, 2012) at 41 evaluation areas of  $30 km \times 30 km$  within the CHUVA-Vale region.

Ch09: $10.8 \mu m$ — [15 <i>min</i> ] — 120117								
Time	POD	FAR	TS	<i>a</i>	<i>b</i>	<i>c</i>	<i>d</i>	<i>n</i>
0 : 00	0.67	0.53	0.38	14	16	7	4	41
0 : 15	0.91	0.74	0.25	10	29	1	1	41
0 : 30	0.82	0.82	0.18	7	31	1	2	41
0 : 45	0.60	0.92	0.08	3	35	2	1	41
14 : 00	1.00	0.98	0.02	1	40	0	0	41
14 : 15	1.00	0.98	0.02	1	40	0	0	41
14 : 30	1.00	0.90	0.10	4	37	0	0	41
14 : 45	1.00	0.85	0.15	6	35	0	0	41
15 : 00	1.00	0.76	0.24	10	31	0	0	41
15 : 15	1.00	0.73	0.27	11	30	0	0	41
15 : 30	1.00	0.78	0.22	9	32	0	0	41
15 : 45	1.00	0.66	0.34	14	27	0	0	41
16 : 00	1.00	0.66	0.34	14	27	0	0	41
16 : 15	1.00	0.61	0.39	16	25	0	0	41
16 : 30	0.93	0.65	0.34	14	26	1	0	41
16 : 45	0.50	0.86	0.12	5	31	5	0	41
17 : 00	0.57	0.77	0.20	8	27	6	0	41
17 : 15	0.69	0.69	0.28	11	24	5	1	41
17 : 30	0.44	0.78	0.17	7	25	9	0	41
17 : 45	0.64	0.58	0.34	14	19	8	0	41
18 : 00	0.52	0.65	0.27	11	20	10	0	41
18 : 15	0.57	0.57	0.33	13	17	10	1	41
18 : 30	0.47	0.73	0.21	8	22	9	2	41
18 : 45	0.68	0.55	0.37	13	16	6	6	41
19 : 00	0.50	0.62	0.28	11	18	11	1	41
19 : 15	0.58	0.46	0.38	15	13	11	2	41
19 : 30	0.64	0.50	0.39	14	14	8	5	41
19 : 45	0.71	0.50	0.42	15	15	6	5	41
20 : 00	0.71	0.52	0.41	15	16	6	4	41
20 : 15	0.73	0.39	0.50	19	12	7	3	41
20 : 30	0.75	0.34	0.54	21	11	7	2	41
20 : 45	0.67	0.53	0.38	14	16	7	4	41
<i>Average</i>	<b>0.76</b>	<b>0.68</b>	<b>0.28</b>	-	-	-	-	-

Table 5.4 - The  $10.8 \mu m$  channel's verification using lightning data from BrasilDAT network accumulated every 15 *min* and 15 *min*-satellite images during 1-day with significant lightning activity (March 13, 2012) at 41 evaluation areas of  $30 km \times 30 km$  within the CHUVA-Vale region.

Ch09: $10.8 \mu m$ — [15 <i>min</i> ] — 120117								
<b>Time</b>	<b>POD</b>	<b>FAR</b>	<b>TS</b>	<i>a</i>	<i>b</i>	<i>c</i>	<i>d</i>	<i>n</i>
18 : 00	0.74	0.24	0.14	14	5	10	0	41
18 : 15	0.76	0.20	0.12	13	4	10	1	41
18 : 30	0.67	0.29	0.18	12	6	9	2	41
18 : 45	0.75	0.29	0.16	15	5	6	6	41
19 : 00	0.83	0.19	0.10	15	3	11	1	41
19 : 15	0.94	0.08	0.04	15	1	11	2	41
19 : 30	0.94	0.07	0.03	15	1	8	5	41
19 : 45	0.88	0.12	0.06	14	2	6	5	41
20 : 00	0.76	0.27	0.14	13	4	6	4	41
20 : 15	0.59	0.50	0.29	10	7	7	3	41
20 : 30	0.69	0.42	0.22	11	5	7	2	41
20 : 45	0.79	0.25	0.13	11	3	7	4	41
<i>Average</i>	<b>0.78</b>	<b>0.25</b>	<b>0.13</b>	-	-	-	-	-

Table 5.5 - The  $(6.2 - 10.8) \mu m$  channel difference's verification using lightning data from BrasilDAT network accumulated every 15 *min* and 15 *min*-satellite images during 1-day with significant lightning activity (January 17, 2012) at 41 evaluation areas of  $30 km \times 30 km$  within the CHUVA-Vale region.

Ch05-Ch09: $(6.2 - 10.8) \mu m$ — [15 <i>min</i> ] — 120117								
Time	POD	FAR	TS	<i>a</i>	<i>b</i>	<i>c</i>	<i>d</i>	<i>n</i>
0 : 00	0.92	0.45	0.52	11	9	1	20	41
0 : 15	0.73	0.60	0.35	8	12	3	18	41
0 : 30	0.75	0.70	0.27	6	14	2	19	41
0 : 45	1.00	0.74	0.26	5	14	0	22	41
14 : 00	1.00	0.91	0.09	1	10	0	30	41
14 : 15	1.00	0.93	0.07	1	14	0	26	41
14 : 30	0.50	0.88	0.11	2	14	2	23	41
14 : 45	0.50	0.81	0.16	3	13	3	22	41
15 : 00	0.60	0.65	0.29	6	11	4	20	41
15 : 15	0.72	0.59	0.34	8	12	3	18	41
15 : 30	0.33	0.77	0.16	3	10	6	22	41
15 : 45	0.57	0.53	0.35	8	9	6	18	41
16 : 00	0.43	0.54	0.29	6	7	8	20	41
16 : 15	0.50	0.47	0.35	8	7	8	18	41
16 : 30	0.80	0.37	0.55	12	7	3	19	41
16 : 45	0.80	0.53	0.42	8	9	2	22	41
17 : 00	0.86	0.43	0.52	12	9	2	18	41
17 : 15	0.81	0.41	0.52	13	9	3	16	41
17 : 30	0.88	0.44	0.52	14	11	2	14	41
17 : 45	0.77	0.35	0.55	17	9	5	10	41
18 : 00	0.81	0.39	0.53	17	11	4	9	41
18 : 15	0.70	0.41	0.47	16	11	7	7	41
18 : 30	0.88	0.46	0.50	15	13	2	11	41
18 : 45	0.63	0.57	0.34	12	16	7	6	41
19 : 00	0.86	0.30	0.63	19	8	3	11	41
19 : 15	0.73	0.34	0.53	19	10	7	5	41
19 : 30	0.73	0.47	0.44	16	14	6	5	41
19 : 45	0.76	0.52	0.42	16	17	5	3	41
20 : 00	0.76	0.52	0.42	16	17	5	3	41
20 : 15	0.88	0.34	0.61	23	12	3	3	41
20 : 30	0.89	0.32	0.63	25	12	3	1	41
20 : 45	0.90	0.49	0.49	19	18	2	2	41
<i>Average</i>	<b>0.75</b>	<b>0.54</b>	<b>0.40</b>	-	-	-	-	-

Table 5.6 - The  $(6.2 - 10.8) \mu m$  channel difference's verification using lightning data from BrasilDAT network accumulated every 15 *min* and 15 *min*-satellite images during 1-day with significant lightning activity (March 13, 2012) at 41 evaluation areas of  $30 km \times 30 km$  within the CHUVA-Vale region.

Ch05-Ch09: $(6.2 - 10.8) \mu m$ — [15 <i>min</i> ] — 120313								
<b>Time</b>	<b>POD</b>	<b>FAR</b>	<b>TS</b>	<i>a</i>	<i>b</i>	<i>c</i>	<i>d</i>	<i>n</i>
18 : 00	0.76	0.27	0.59	16	6	5	14	41
18 : 15	0.75	0.38	0.52	15	9	5	12	41
18 : 30	0.32	0.46	0.25	7	6	15	13	41
18 : 45	0.71	0.43	0.46	12	9	5	15	41
19 : 00	0.75	0.43	0.48	12	9	4	16	41
19 : 15	0.67	0.60	0.33	8	12	4	17	41
19 : 30	0.73	0.48	0.44	11	10	4	16	41
19 : 45	0.76	0.38	0.52	13	8	4	16	41
20 : 00	0.64	0.53	0.38	9	10	5	17	41
20 : 15	0.43	0.68	0.22	6	13	8	14	41
20 : 30	0.50	0.67	0.25	6	12	6	17	41
20 : 45	0.67	0.60	0.33	8	12	4	17	41
<i>Average</i>	<b>0.64</b>	<b>0.49</b>	<b>0.40</b>	-	-	-	-	-

Table 5.7 - *Trispectral* channel difference's verification using lightning data from Brasil-DAT network accumulated every 15 *min* and 15 *min*-satellite images during 1-day with significant lightning activity (January 17, 2012) at 41 evaluation areas of 30 *km* × 30 *km* within the CHUVA-Vale region.

(8.7 – 10.8) – (10.8 – 12.0) $\mu m$ — [15 <i>min</i> ] — 120117								
<b>Time</b>	<b>POD</b>	<b>FAR</b>	<b>TS</b>	<i>a</i>	<i>b</i>	<i>c</i>	<i>d</i>	<i>n</i>
0 : 00	0.92	0.42	0.55	11	8	1	21	41
0 : 15	0.73	0.58	0.36	8	11	3	19	41
0 : 30	0.75	0.65	0.32	6	11	2	22	41
0 : 45	1.00	0.72	0.28	5	13	0	23	41
14 : 00	1.00	0.91	0.09	1	10	0	30	41
14 : 15	1.00	0.00	1.00	12	0	0	29	41
14 : 30	0.25	0.92	0.06	1	12	3	25	41
14 : 45	0.50	0.82	0.15	3	14	3	21	41
15 : 00	0.50	0.69	0.24	5	11	5	20	41
15 : 15	0.55	0.65	0.27	6	11	5	19	41
15 : 30	0.33	0.80	0.14	3	12	6	20	41
15 : 45	0.50	0.53	0.32	7	8	7	19	41
16 : 00	0.43	0.60	0.26	6	9	8	18	41
16 : 15	0.63	0.41	0.43	10	7	6	18	41
16 : 30	0.73	0.39	0.50	11	7	4	19	41
16 : 45	0.80	0.56	0.40	8	10	2	21	41
17 : 00	0.92	0.42	0.55	12	9	2	18	41
17 : 15	0.92	0.42	0.55	11	9	5	16	41
17 : 30	0.92	0.42	0.55	15	11	1	14	41
17 : 45	0.92	0.42	0.55	17	10	5	9	41
18 : 00	0.92	0.42	0.55	17	11	4	9	41
18 : 15	0.92	0.42	0.55	16	11	7	7	41
18 : 30	0.92	0.42	0.55	15	13	2	11	41
18 : 45	0.92	0.42	0.55	12	14	7	8	41
19 : 00	0.92	0.42	0.55	18	9	4	10	41
19 : 15	0.92	0.42	0.55	19	10	7	5	41
19 : 30	0.92	0.42	0.55	16	12	6	7	41
19 : 45	0.92	0.42	0.55	15	15	6	5	41
20 : 00	0.92	0.42	0.55	15	17	6	3	41
20 : 15	0.92	0.42	0.55	21	13	5	2	41
20 : 30	0.92	0.42	0.55	23	12	5	1	41
20 : 45	0.92	0.42	0.55	18	17	3	3	41
<i>Average</i>	<b>0.79</b>	<b>0.51</b>	<b>0.44</b>	-	-	-	-	-

Table 5.8 - *Trispectral* channel difference's verification using lightning data from Brasil-DAT network accumulated every 15 *min* and 15 *min*-satellite images during 1-day with significant lightning activity (March 13, 2012) at 41 evaluation areas of 30 *km* × 30 *km* within the CHUVA-Vale region.

(8.7 – 10.8) – (10.8 – 12.0) $\mu m$ — [15 <i>min</i> ] — 120117								
Time	POD	FAR	TS	<i>a</i>	<i>b</i>	<i>c</i>	<i>d</i>	<i>n</i>
18 : 00	0.76	0.24	0.62	16	5	5	15	41
18 : 15	0.75	0.29	0.58	15	6	5	15	41
18 : 30	0.67	0.30	0.52	14	6	7	14	41
18 : 45	0.59	0.47	0.38	10	9	7	15	41
19 : 00	0.63	0.44	0.42	10	8	6	17	41
19 : 15	0.67	0.56	0.36	8	10	4	19	41
19 : 30	0.47	0.53	0.30	7	8	8	18	41
19 : 45	0.71	0.37	0.50	12	7	5	17	41
20 : 00	0.57	0.53	0.35	8	9	6	18	41
20 : 15	0.43	0.63	0.25	6	10	8	17	41
20 : 30	0.42	0.67	0.23	5	10	7	19	41
20 : 45	0.67	0.58	0.35	8	11	4	18	41
<i>Average</i>	<b>0.61</b>	<b>0.41</b>	<b>0.40</b>	-	-	-	-	-

Table 5.9 - Contingency table for the *index sum* of 4 *interest fields*; using the comparison between lightning data occurred and predicted by the conceptual model during 2-days with significant lightning activity at evaluation areas of 30 *km* × 30 *km* within the CHUVA-Vale region. The *index sum* is the total sum (from 16 to 4) of 4 *interest fields* *émph* indices (from 4 to 0). The *occurrences* are the number of evaluation areas that reach the corresponding *index sum*.

4 IF=( <i>Ch05</i> – <i>Ch06</i> ) + <i>Ch09</i> + ( <i>Ch05</i> – <i>Ch09</i> ) + <i>trispectral</i> — 15 <i>min</i>								
<i>Index sum</i>	POD	FAR	TS	<i>a</i>	<i>b</i>	<i>c</i>	<i>d</i>	<i>Occurrences</i>
16	1.00	0.58	0.42	716	1009	0	3	432
15	1.00	0.55	0.45	73	91	0	0	41
14	0.75	0.51	0.42	45	47	15	13	30
13	0.74	0.59	0.36	35	50	12	19	29
12	0.74	0.33	0.54	386	191	138	53	192
11	0.61	0.83	0.16	11	52	7	22	23
10	0.52	0.61	0.29	13	20	12	15	15
9	0.47	0.68	0.24	09	19	10	18	14
8	0.50	0.90	0.09	11	104	11	94	55
7	0.33	0.74	0.17	08	23	16	25	18
6	0.25	0.72	0.15	10	26	30	78	36
5	0.24	0.66	0.16	10	19	32	55	29
4	0.25	0.81	0.12	71	306	215	904	374

Table 5.10 - Contingency table for the **intervals** of *index sum* of 4 *interest fields*; using the comparison between lightning data occurred and predicted by the conceptual model during 2-days with significant lightning activity at evaluation areas of 30 km × 30 km within the CHUVA-Vale region. The *index sum* is the total sum (from 16 to 4) of 4 *interest fields indices* (from 4 to 0). The **interval index sum** are 3 intervals with *index sum* from 16 to 12; 12 to 8 and 8 to 4, respectively. The *occurrences* are the number of evaluation areas that reach the corresponding **interval index sum**.

4 IF=(Ch05 - Ch06) + Ch09 + (Ch05 - Ch09) + trispectral - 15 min								
<b>Interval index sum</b>	<b>POD</b>	<b>FAR</b>	<b>TS</b>	<i>a</i>	<i>b</i>	<i>c</i>	<i>d</i>	<i>Occurrences</i>
16 — 12	0.85	0.51	0.44	1255	1388	165	88	724
12 — 8	0.53	0.75	0.19	44	195	40	149	107
8 — 4	0.27	0.73	0.15	99	374	293	1062	457



## 6 Conclusions

The main objective of this study was to increase the understanding on how cumulus clouds evolve to thunderstorms as means of identifying a representative behavior of compact thunderstorms and its early electrification process in satellite multi-channel observations. This will allow a development of nowcasting tools using data from the Meteosat Second Generation (*MSG*) Satellite at the boundary of tropical and subtropical regions, and also will allow a potential development of nowcasting tools with the perspective of using data from the Geostationary Operational Environmental Satellite-R (*GOES-16*) in future works.

The conclusions about the representative behavior of compact thunderstorms and its early electrification process in satellite multi-channel cloud-top signatures resulting from the study of 40 cases and 4 *IR interest fields* selected to detect *intensification of cloud* and *electrification* processes, are summarized below as *evaluation area*, *model predictors*, *verification* and *improvements*, and future works:

- An *evaluation area* of  $30\text{ km} \times 30\text{ km}$  has satisfied both requirements determined as (i) detection efficiency of the lightning mapping distance and (ii) minimum noise in the *Tb* (*Tbd*) histograms, so it has been selected as the befitting area for thunderstorm detection along with a sequential sample of electrification life cycle cases;
- A subset of 4 *IR interest fields* have been selected as thunderstorm *predictors*: **IF1**; **IF2**, **IF3** and **IF4**. The predictors are capable of demonstrating *differentiation* between 4 lightning time steps in the *Tb* (*Tbd*) histograms. Also these predictors have been selected for detecting the region of *intensification of cloud* and *electrification* processes in the *Tb* (*Tbd*) histograms;
  - **IF1** = Ch05-Ch06:  $(6.2 - 7.3)\ \mu\text{m}$ , or **Predictor 1**. This predictor can give an indication of moisture content at medium levels and depth of the convective clouds. A region inside these *Tbd* histograms to detect significant *differentiation* among the lightning time steps of 40 cases studies, began from  $Tbd \geq -16.0\text{ K}$ . There is an *increasing* trend of the populations in that region, or *increasing* variability from 40.22 to 55.32% of pixels with values of  $Tbd \geq -12.0\text{ K}$  related to an *intensification* of the convective clouds processes among the lightning time steps. Indeed,  $Tbd = -12.0\text{ K}$  is the *Tbd relative cumulative-frequency* curve with greater value of *maxima derivative*

- during the *1IC* (*t2*) lightning time step, and  $Tbd \geq -12.0 K$  is the *threshold* to detect *cloud intensification* using *IF1* histograms;
- **IF2** = Ch09:  $10.8 \mu m$ , or **Predictor 2**. This predictor is related to cloud depth and convective processes. A region inside these *Tbd* histograms to detect significant *differentiation* among the lightning time steps of 40 cases studies, began from  $Tb \leq +223.0 K$ . Also, there is an *increasing* trend of the populations in that region, or *increasing* variability from 7.21 to 14.17% of pixels with values of  $Tb \leq +223.0 K$  related to an *intensification* of the convective processes among the lightning time steps. Actually,  $Tb = +223.0 K$  is the *Tb relative cumulative-frequency* curve with greater value of *maxima derivative* at the *1IC* (*t2*) lightning time step, and  $Tb \leq +223.0 K$  is the *threshold* for detecting *cloud intensification* using *IF2* histograms;
  - **IF3** = Ch05-Ch09:  $(6.2 - 10.8) \mu m$ , or **Predictor 3**. This predictor is related to overshooting tops and to a potential for cloud-to-ground discharge activity. A region inside these *Tbd* histograms to detect high *differentiation* among the lightning time steps of selected cases, began from  $Tbd \geq -14.0 K$ . Also in that region, there is an *increasing* trend of the populations, or *increasing* variability from 28.74 to 38.18% of pixels with values of  $Tbd \geq -14.0 K$  related to an *intensification* of the electrification processes among the lightning time steps. Specifically,  $Tbd = -14.0 K$  is the *Tbd relative cumulative-frequency* curve with greater value of *maxima derivative* at the *1CG* (*t3*) lightning time step, and  $Tbd \geq -14.0 K$  is the *threshold* to detect *intensification* of electrification processes using *IF3* histograms;
  - **IF4** = Trispectral:  $(8.7 - 10.8) - (10.8 - 12.0) \mu m$ , or **Predictor 4**. This predictor is related to glaciation in convective clouds. A region inside these *Tbd* histograms to detect high *differentiation* among the lightning time steps of 40 cases studies selected, began from  $Tbd \geq 0 K$ . Also in that region, there is an *increasing* trend of populations, or *increasing* variability from 30.07 to 42.04% of pixels with values of  $Tbd \geq 0$  related to an *intensification* of the glaciation processes among the lightning time steps. In fact,  $Tbd = 0 K$  is the *Tbd relative cumulative-frequency* curve with greater value of *maxima derivative* at the *1CG* (*t3*) lightning time step, and  $Tbd \geq 0 K$  is the *threshold* to detect *intensification* of glaciation processes using *IF3* histograms;
  - Each one of the 4 *interest fields* cannot be used like a single predictor

of significant *intensification* of the thunderstorms processes, but using all 4 predictors together, or all 4 *Tbd relative cumulative-frequency* curves with greater value of *maxima derivative* ( $Tbd = -12.0 K$  for IF1,  $Tb = +223.0 K$  for IF2,  $Tbd = -14.0 K$  for IF3 and  $Tbd = 0 K$  for IF4) will make the conceptual model of thunderstorm detection more accurate as synthesized by figure 6.1;

- For the *verification* of the conceptual model of thunderstorm detection, 2 independent tests of the 4 *interest fields* were implemented every 15 *min* cycle during 2-days with significant lightning activity at evaluation areas of 30 *km* × 30 *km* within the CHUVA-Vale region:
  - First, throughout the determination of which *interest field* has more and least association between brightness temperature and lighting detection at evaluation areas of 30 *km* × 30 *km* within the CHUVA-Vale region, values of *POD* greater than 0.70 and values of *FAR* less than 0.50 were obtained. In future works, the conceptual model's *POD* may increase and the *FAR* may decrease by implementing this first independent verification test for more than 2-days of significant lightning activity in the CHUVA-Vale region;
  - Second, throughout the skill determination of all 4 *interest fields* at the same evaluation areas of 30 *km* × 30 *km* selected for the first verification test, the conceptual model presented a higher probability of lightning detection for *index sums* between 16 and 12 due to the higher *POD* and lower *FAR* values, or from 1.00 to 0.74 and from 0.55 to 0.33, respectively. Also, the conceptual model presented a lower probability of lightning detection for *index sums* between 8 and 4 because of the lower *POD* and higher *FAR* values, or from 0.61 to 0.24 and from 0.83 to 0.61, respectively;
  - Throughout these 2 independent tests was possible to indicate that the conceptual model of thunderstorm detection is more accurate and has a higher probability of lightning detection for the **interval** of *index sums* from 16 to 12 because of the higher *POD* and lower *FAR* values, or 0.85 and 0.51, respectively;
  - It is estimated that in a future work, the conceptual model's *POD* may increase and the *FAR* may decrease by implementing these independent tests for more than 2-days of significant lightning activity in the CHUVA-Vale region;

- Based on these conclusions, future studies should investigate the impact of non-convective pixels on the results, since it is hypothesized that the evaluation area of the  $Tb$  ( $Tbd$ ) histograms is covered by pixels associated with convective clouds;
- Also based on these conclusions, future studies can advance to gain insight into how a subset of *SEVIRI* visible ( $VIS$ ) and near-infrared ( $NIR$ ) fields, or, an array of the Advanced Baseline Image ( $ABI$ ) spectral bands from the *GOES-16*, may be used to increase understanding on clouds evolution to full thunderstorms;
- Additional knowledge about lightning initiation can be obtained linking satellite multi-channel cloud-top signatures of thunderstorm's early electrification process and total lightning information from the Geostationary Lightning Mapper ( $GLM$ ) on the *GOES-16* satellite along with polarimetric radar data set.

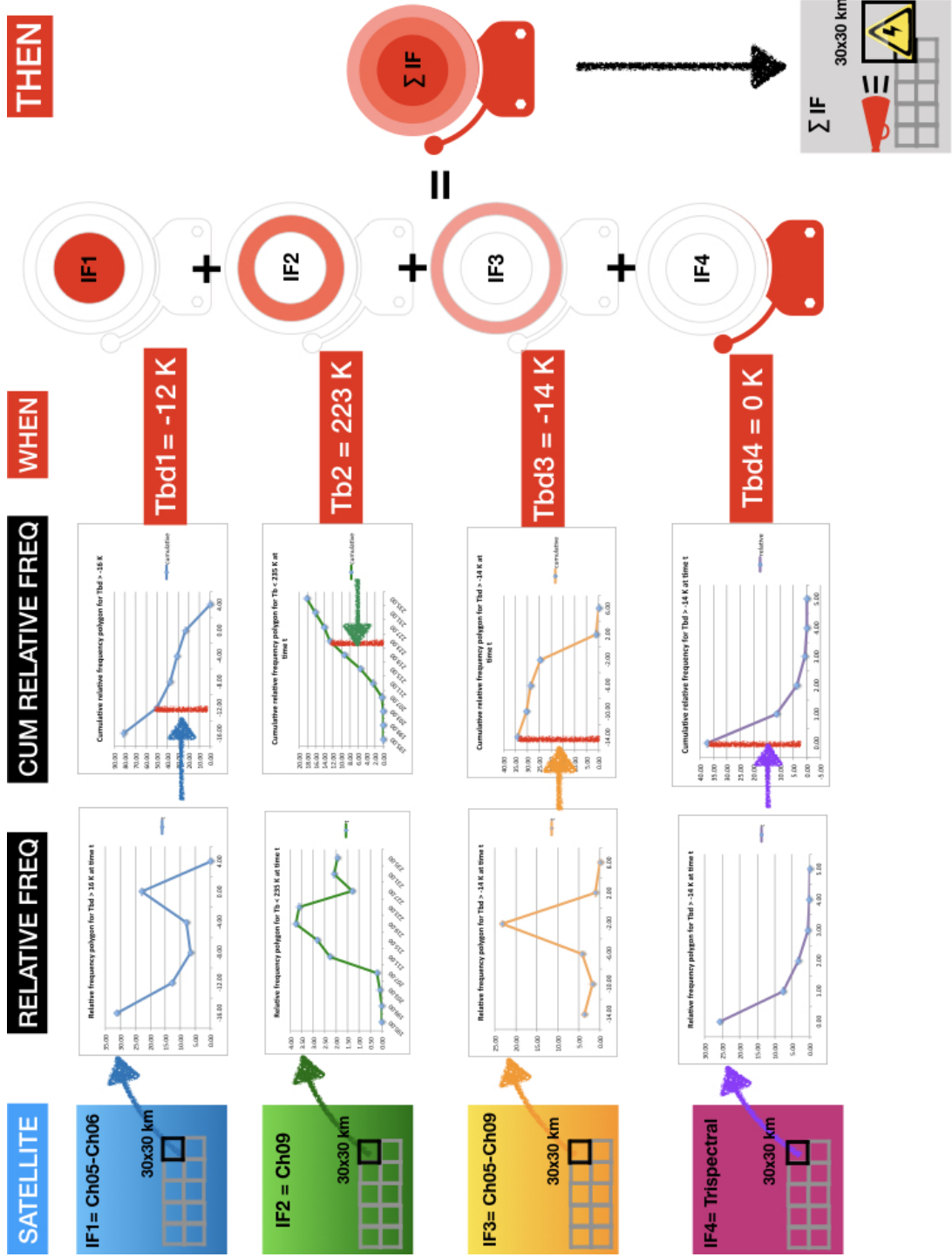


Figure 6.1 - Synthesis of the conceptual model of thunderstorm detection using all 4 predictors thresholds as  $T_{bd} = -12.0 K$  for **IF1** = **Ch05-Ch06**:  $(6.2 - 7.3) \mu m$ ;  $T_b = +223.0 K$  for **IF2** = **Ch09**:  $10.8 \mu m$ ;  $T_{bd} = -14.0 K$  for **IF3** = **Ch05-Ch09**:  $(6.2 - 10.8) \mu m$ , and  $T_{bd} = 0 K$  for **IF4** = **Trispectral**:  $(8.7 - 10.8) - (10.8 - 12.0) \mu m$ .



## REFERENCES

- ACKERMAN, S. Global satellite observations of negative brightness temperature differences between 11 and 6.7  $\mu\text{m}$ . **American Meteorological Society**, v. 53, n. 19, p. 2803–2812, 1996. 10, 41
- ALBRECHT, R. **Anexo I. Projeto CHUVA-Vale. Descrição das atividades CHUVA-GLM Vale do Paraíba relacionadas aos programas de satélite GOER-R e MTG**. Brazil, 2011. 1–41 p. Anexo I. Available from: <<http://chuvaproject.cptec.inpe.br>>. Access in: 2017. 24
- ALBRECHT, R.; MORALES, C.; IWABE, C.; SABA, M.; HOLLER, H. **Using Lightning Mapping Array to evaluate the lightning detection signatures at different technologies**. [S.l.], 06 2014. 23, 25, 28
- BAILEY, J.; BLAKESLEE, R.; CAREY, L.; GOODMAN, S.; RUDLOSKEY, S.; ALBRECHT, R.; MORALES, C.; ANSELMO, E.; NEVES, J.; BUECHLER, D. São paulo lightning mapping array (sp-lma): Network assessment and analyses for intercomparison. 2014. 29
- BERBERY, E.; COLLINI, E. Springtime precipitation and water vapor flux over southeastern south america. **Monthly Weather Review**, v. 128, n. 5, p. 1328–1346, 2000. 16
- BLAKESLEE, R.; BAILEY, J.; CAREY, L.; GOODMAN, S.; RUDLOSKEY, S.; ALBRECHT, R.; MORALES, C.; ANSELMO, E.; NEVES, J. São paulo lightning mapping array (sp-lma): Network assessment and analyses for intercomparison studies and goes-r proxy activities. 2013. 24, 29, 37
- BROWNING, K.; COLLIER, C. Nowcasting of precipitation systems. **Reviews of Geophysics**, Wiley Online Library, v. 27, n. 3, p. 345–370, 1989. 8
- CARDOSO, I.; PINTO, J. O.; PINTO, I.; R., H. Recent advances in classification of observations from dual polarization weather radars. **Atmospheric Research**, v. 135-136, p. 374–379, 2014. 1
- CHMIELEWSKI, V.; BRUNING, E. Lightning mapping array flash detection performance with variable receiver thresholds. **Journal of Geophysical Research: Atmospheres**, v. 121, n. 14, p. 8600–8614, 2016. ISSN 2169-8996. Available from: <<http://dx.doi.org/10.1002/2016JD025159>>. 37

- CHRONIS, T.; CAREY, L.; SCHULTZ, C.; SCHULTZ, E.; CALHOUN, K.; GOODMAN, S. Exploring lightning jump characteristics. **Weather and Forecasting**, v. 30, n. 1, p. 23–37, 2015. 13
- DALOZE, J.; HAEFFELIN, M. Validation of safnwc/msg cloud top height using ground-based lidar and radar measurements. **Visiting Scientist Report, CMS Lannion**, 2005. 21
- DERRIEN, M.; GLÉAU, H.; DALOZE, J.; HAEFFELIN, M. Validation of safnwc/msg cloud products with one year of sevir data. In: . [S.l.: s.n.], 2005. p. 95–103. 21
- DURKEE, J.; MOTE, T. A climatology of warm-season mesoscale convective complexes in subtropical south america. **International Journal of Climatology**, Wiley Online Library, v. 30, n. 3, p. 418–431, 2010. 1
- GATLIN, P.; GOODMAN, S. A total lightning trending algorithm to identify severe thunderstorms. **Journal of Atmospheric and Oceanic Technology**, v. 27, n. 1, p. 3–22, 2010. 13
- HUAMÁN, J. **Potencial dos multicanais na detecção de descargas elétricas: Uso do GOES-16**. Proposta de Dissertação (Mestrado em Meteorologia) — Instituto Nacional de Pesquisas Espaciais (INPE), São José dos Campos, 2017. 34
- JONES, T.; OTKIN, J.; STENSRUD, D.; KNOPFMEIER, K. Forecast evaluation of an observing system simulation experiment assimilating both radar and satellite data. **Monthly Weather Review**, v. 142, n. 1, p. 107–124, 2014. 17
- JONES, T.; STENSRUD, D.; MINNIS, P.; PALIKONDA, R. Evaluation of a forward operator to assimilate cloud water path into wrf-dart. **Monthly Weather Review**, v. 141, n. 7, p. 2272–2289, 2013. 17
- KARAGIANNIDIS, A.; LAGOUVARDOS, K.; KOTRONI, V. The use of lightning data and Meteosat infrared imagery for the nowcasting of lightning activity. **Atmospheric Research**, n. 168, p. 57–69, 2016. 3, 7, 9, 15
- KIDDER, S.; HAAR, T. V. **Satellite Meteorology An Introduction**. USA: Academic Press, 1995. 18, 25
- LÁBÓ, E.; KERÉNYI, J.; PUTSAY, M. The parallax correction of msg images on the basis of the safnwc cloud top height product. **EUMETSAT meteorological satellite conference**, n. May, p. 2–9, 2007. 19, 34

MACHADO, L. **Projeto CHUVA-Vale**. Brazil, 2012. 1–39 p. Anexo V. Available from: <<http://chuvaproject.cptec.inpe.br>>. Access in: 2017. 25

MACHADO, L.; DESBOIS, M.; DUVEL, J.-P. Structural characteristics of deep convective systems over tropical africa and the atlantic ocean. **Monthly Weather Review**, v. 120, n. 3, p. 392–406, 1992. 10

MACHADO, L.; DIAS, M. S.; MORALES, C.; FISCH, G.; VILA, D.; ALBRECHT, R.; GOODMAN, S. J.; CALHEIROS, A. J. P.; BISCARO, T.; KUMMEROW, C.; COHEN, J.; FITZJARRALD, D.; NASCIMENTO, E. L.; SAKAMOTO, M.; CUNNINGHAM, C.; CHABOUREAU, J.; PETERSEN, W.; ADAMS, D.; BALDINI, L.; ANGELIS, C.; SAPUCCI, L.; SALIO, P.; BARBOSA, H.; LANDULFO, E.; SOUZA, R.; BLAKESLEE, R.; BAILEY, J.; FREITAS, S.; LIMA, W.; TOKAY, A. The chuva project: How does convection vary across brazil. **Bulletin of the American Meteorological Society**, v. 95, n. 9, p. 1365–1380, 2014. ISSN 00030007. 8, 23, 24, 25, 26, 27, 28

MACHADO, L.; LIMA, W.; PINTO, O.; MORALES, C. Relationship between cloud-to-ground discharge and penetrative clouds: A multi-channel satellite application. **Atmospheric Research**, Elsevier B.V., v. 93, n. 1-3, p. 304–309, 2009. ISSN 01698095. Available from: <<http://dx.doi.org/10.1016/j.atmosres.2008.10.003>>. 2, 10, 13, 15, 41

MACHADO, L.; ROSSOW, W. B.; GUEDES, R. L.; WALKER, A. W. Life cycle variations of mesoscale convective systems over the americas. **Monthly Weather Review**, n. 126, p. 1630–1654, 1998. Available from: <[http://dx.doi.org/10.1175/1520-0493\(1998\)126<1630:LCVOMC>2.0.CO;2](http://dx.doi.org/10.1175/1520-0493(1998)126<1630:LCVOMC>2.0.CO;2)>. 10

MASS, C.; MASS, C. et al. Nowcasting: The next revolution in weather prediction. **Bulletin of the American Meteorological Society**, 2011. 8

MATTHEE, R.; MECIKALSKI, J. Geostationary infrared methods for detecting lightning-producing cumulonimbus clouds. **Journal of Geophysical Research Atmospheres**, v. 118, n. 12, p. 6580–6592, 2013. ISSN 21698996. 2, 9, 14, 40, 41, 42, 43

MATTOS, E. **Relações entre assinaturas polarimétricas de radar e atividade elétrica das tempestades**. 1-216 p. (sid.inpe.br/mtc-m21b/2015/06.03.14.50-TDI). Tese (Doutorado em Meteorologia) — Instituto Nacional de Pesquisas Espaciais (INPE), São José dos Campos, 2015.

Available from: <<http://urlib.net/8JMKD3MGP3W34P/3JK5HDP>>. Access in: 2016. 30

MATTOS, E.; MACHADO, L. Cloud-to-ground lightning and mesoscale convective systems. **Atmospheric Research**, v. 99, n. 3-4, p. 377–390, 2011. ISSN 01698095. 13

MATTOS, E.; MACHADO, L.; WILLIAMS, E.; ALBRECHT, R. Polarimetric radar characteristics of storms with and without lightning activity. **Journal of Geographic Research: Atmospheres**, v. 121, p. 14,201–14,220, 2016. 14, 15, 26, 27, 30, 37

MATTOS, E.; MACHADO, L.; WILLIAMS, E.; GOODMAN, S.; BLAKESLEE, R.; BAILEY, J. Electrification life cycle of incipient thunderstorms. **Journal of Geophysical Research: Atmospheres**, Wiley Online Library, v. 122, n. 8, p. 4670–4697, 2017. xv, 2, 5, 7, 28, 29

MECIKALSKI, J.; BEDKA, K. Forecasting convective initiation by monitoring the evolution of moving cumulus in daytime goes imagery. **Monthly Weather Review**, v. 134, p. 49–78, 2006. ISSN 0027-0644. 9, 11, 13, 41

MECIKALSKI, J.; BEDKA, K.; PAECH, S.; LITTEN, L. A statistical evaluation of goes cloud-top properties for nowcasting convective initiation. **Monthly Weather Review**, v. 136, p. 4899–4914, 2008. 11, 73

MECIKALSKI, J.; LI, X.; CAREY, L.; MCCAUL, E. W.; COLEMAN, T. Regional comparison of goes cloud-top properties and radar characteristics in advance of first-flash lightning initiation. **Monthly Weather Review**, v. 141, p. 55–74, 2013. ISSN 0027-0644. 3, 14, 15

MECIKALSKI, J.; MACKENZIE, W.; KÖNIG, M.; MULLER, S. Cloud-top properties of growing cumulus prior to convective initiation as measured by meteosat second generation. part ii: Use of visible reflectance. **Journal of Applied Meteorology and Climatology**, v. 49, n. 12, p. 2544–2558, 2010. ISSN 15588424. xxi, xxii, 10, 11, 12, 25, 40, 41, 43, 53, 57, 58, 62, 67

MECIKALSKI, J.; ROSENFELD, D.; MANZATO, A. Evaluation of geostationary satellite observations and the development of a 1-2 h prediction model for future storm intensity. **Journal of Geophysical Research: Atmospheres**, Wiley Online Library, v. 121, n. 11, p. 6374–6392, 2016. 13, 17

MEDINA, B.; MACHADO, L. Dual polarization radar lagrangian parameters: a statistics-based probabilistic nowcasting model. **Natural Hazards**, v. 89, n. 2, p. 705–721, Nov 2017. ISSN 1573-0840. Available from:

<<https://doi.org/10.1007/s11069-017-2988-y>>. 9

MOSIER, R.; SCHUMACHER, C.; ORVILLE, R.; CAREY, L. Radar nowcasting of cloud-to-ground lightning over houston, texas. **Weather and Forecasting**, v. 26, n. 2, p. 199–212, 2011. 3

MULLER, O.; LOVINO, M.; BERBERY, E. Evaluation of wrf model forecasts and their use for hydroclimate monitoring over southern south america. **Weather and Forecasting**, v. 31, n. 3, p. 1001–1017, 2016. 16

NASCIMENTO, E. **Satélites meteorológicos na Meteorologia Sinótica**. Brazil, 2014. 1–86 p. Programa de Posgraduação em Meteorologia. 32, 39, 40, 42

NETO, C.; BARBOSA, H.; BENETI, C. A method for convective storm detection using satellite data. **Universidad Nacional Autónoma de México, Centro de Ciencias de la Atmósfera**, v. 29, p. 343–358, 2016. 9, 10, 16

NIEMAN, S.; SCHMETZ, J.; MENZEL, W. A Comparison of Several Techniques to Assign Height to Cloud Tracers. **American Meteorology Society**, v. 32, p. 1559–1568, 1993. xvi, 20, 21, 33

PETTY, G. **A First Course in Atmospheric Radiation**. USA: Sundog Publishing, 2006. 40, 42

PIERCE, C.; SEED, A.; BALLARD, S.; SIMONIN, D.; LI, Z. Nowcasting. In: **Doppler Radar Observations-Weather Radar, Wind Profiler, Ionospheric Radar, and Other Advanced Applications**. [S.l.]: InTech, 2012. 8

RADOVÁ, M.; SEIDL, J. **Parallax applications when comparing radar and satellite data**. 2008. 1–6 p. Available from:

<[http://www.eumetsat.int/groups/cps/documents/document/pdf\\_{\\_}conf\\_{\\_}p\\_{\\_}s5\\_{\\_}22\\_{\\_}radova\\_{\\_}p.pdf](http://www.eumetsat.int/groups/cps/documents/document/pdf_{_}conf_{_}p_{_}s5_{_}22_{_}radova_{_}p.pdf)>. xv, xvi, 18, 19, 20

RINEHART, R. **Radar for Meteorologists**. USA: Rinehart Publishing, 1997. 8

RISON, W.; THOMAS, R.; KREHBIEL, T.; HAMLIN, T.; HARLIN, J. A gps-based three dimensional lightning mapping system: Initial observations in central new mexico. **Geophysical Research Letters**, v. 26, n. 23, p. 3573–3576, 1999. 29

ROEDER, W. P.; MCNAMARA, T. M. Using temperature layered vil as automated lightning warning guidance. In: **5th Conference on Meteorological Applications of Lightning Data**. [S.l.: s.n.], 2011. p. 23–27. [3](#)

ROESLI, H.; ROSENFELD, D.; KERKMANN, J.; KOENIG, M.; LUTZ, H. Msg/seviri channel 4 short-wave ir channel @ 3.9  $\mu m$  ir 3.9 tutorial. In: . [S.l.]: EUMETSAT - Distant Learning Lecture, 2007. [40](#)

ROSENFELD, D.; WOODLEY, W.; LERNER, A.; KELMAN, G.; LINDSEY, D. Satellite detection of severe convective storms by their retrieved vertical profiles of cloud particle effective radius and thermodynamic phase. **Journal of Geophysical Research**, v. 113, n. D04208, p. 22, 2008. [9](#), [11](#), [13](#), [25](#)

SAKURAGI, J.; BISCARO, T. Determination of zdr offset and their impact in the hydrometeor classification. In: . [S.l.: s.n.], 2012. Paper presented at XVII Brazilian Meteorological Conference of the Brazilian Meteorological Society, Gramado, Brazil. [27](#)

SALIO, P.; NICOLINI, M.; ZIPSER, E. Mesoscale convective systems over southeastern south america and their relationship with the south american low-level jet. **Monthly Weather Review**, v. 135, n. 4, p. 1290–1309, 2007. [1](#)

SÁNCHEZ, E.; SOLMAN, S.; REMEDIO, A.; BERBERY, H.; SAMUELSSON, P.; ROCHA, R. D.; MOURÃO, C.; LI, L.; MARENGO, J.; CASTRO, M. de et al. Regional climate modelling in claris-lpb: a concerted approach towards twentyfirst century projections of regional temperature and precipitation over south america. **Climate dynamics**, Springer, v. 45, n. 7-8, p. 2193–2212, 2015. [16](#)

SCHMETZ, J.; PILI, P.; TJEMKES, S.; JUST, D.; KERKMANN, J.; ROTA, S.; RATIER, A. An introduction to meteosat second generation (msg). **Bulletin of the American Meteorological Society**, v. 83, n. 7, p. 977–992, 2002. [26](#)

SCHMETZ, J.; TJEMKES, S.; GUBE, M.; BERG, L. Van de. Monitoring deep convection and convective overshooting with meteosat. **Advances in Space Research**, Elsevier, v. 19, n. 3, p. 433–441, 1997. [2](#), [9](#), [10](#), [41](#)

SCHNEEBELI, M.; SAKURAGI, J.; BISCARO, T.; ANGELIS, C.; COSTA, I. Carvalho da; MORALES, C.; BALDINI, L.; MACHADO, L. Observations of tropical rain with polarimetric x-band radar: first results from chuva campaign. **Atmospheric Measurement Techniques Discussions**, Copernicus Publications, n. 5, p. 1717–1761, 2012. [27](#)

- SELUCHI, M.; CHOU, S. Evaluation of two eta model versions for weather forecast over south america. **Geofísica Internacional**, Universidad Nacional Autónoma de México, v. 40, n. 3, p. 219–237, 2001. 16
- SENF, F.; DIETZSCH, F.; HUNERBEIN, A.; DENEKE, H. Characterization of initiation and growth of selected severe convective storms over central europe with msg-seviri. **Journal of Applied Meteorology and Climatology**, v. 54, n. 1, p. 207–224, 2015. ISSN 15588432. 13
- SETVÁK, M.; DOSWELL, C. I. The avhrr channel 3 cloud top reflectivity of convective storms. **Monthly Weather Review**, v. 119, n. 3, p. 841–847, 1991. 10
- SETVÁK, M.; LINDSEY, D.; RABIN, R.; WANG, P.; DEMETEROVÁ, A. Indication of water vapor transport into the lower stratosphere above midlatitude convective storms: Meteosat second generation satellite observations and radiative transfer model simulations. **Atmospheric Research**, n. 89, p. 170–180, 2008. 10
- SNYDER, C.; ZHANG, F. Assimilation of simulated doppler radar observations with an ensemble kalman filter. **Monthly Weather Review**, Lancaster, Pa., etc., v. 131, n. 8, p. 1663–1677, 2003. 17
- SPIEGEL, M.; STEPHENS, L. **Theory and problems of Statistics**. USA: McGraw-Hill, 2007. 36–57 p. 43, 46
- STOLZ, D.; RUTLEDGE, S.; PIERCE, J.; HEEVER, S. V. D. A global lightning parameterization based on statistical relationships among environmental factors, aerosols, and convective clouds in the trmm climatology. **Journal of Geophysical Research: Atmospheres**, v. 122, n. 14, p. 7461–7492, 2017. ISSN 2169-8996. 2016JD026220. Available from: <<http://dx.doi.org/10.1002/2016JD026220>>. 16
- STRABALA, K.; ACKERMAN, S. Cloud properties inferred from 8-12  $\mu m$ . **Journal of Applied Meteorology**, v. 33, p. 212–229, 1994. 10, 42
- STULL, R. **Practical Meteorology: An Algebra-based Survey of Atmospheric Science**. CANADA: University of British Columbia, 2015. 1
- SZEJWACH, G. Determination of semi-transparent cirrus cloud temperature from infrared radiances: Application to meteosat. **Journal of Applied Meteorology**, v. 21, n. 3, p. 384–393, 1982. 20, 33

VILA, D. **Sistemas convectivos precipitantes de mesoscala sobre sudamérica: ciclos de vida y circulación en gran escala asociada.** 1-142 p. Digital@bl.fcen.uba.ar. Tesis Doctoral — Facultad de Ciencias Exactas y Naturales de la Universidad de Buenos Aires, Buenos Aires, 2004. Available from: <[www.digital.bl.fcen.uba.ar](http://www.digital.bl.fcen.uba.ar)>. Access in: 2017. 41

VILA, D.; MACHADO, L.; LAURENT, H.; VELASCO, I. Forecast and tracking the evolution of cloud clusters (fortracc) using satellite infrared imagery: Methodology and validation. **Weather and Forecasting**, v. 23, n. 2, p. 233–245, 2008. 10

WAGNER, F. L.; MACHADO, L. Cloud reflectivity profile classification using msg/seviri infrared multichannel and trmm data. **International Journal of Remote Sensing**, n. 12, p. 4384–4405, 2013. Available from: <<http://dx.doi.org/10.1080/01431161.2013.776720>>. 2

WALLACE, J.; HOBBS, P. **Atmospheric Science. An Introductory Survey.** USA: University of Washington, 2006. xv, 6, 7

WEYGANDT, S.; SHAPIRO A.AND DROEGEMEIER, K. Retrieval of model initial fields from single-doppler observations of a supercell thunderstorm. part ii: Thermodynamic retrieval and numerical prediction. **Monthly Weather Review**, v. 130, n. 3, p. 454–476, 2002. 17

WILKS, D. **Statistical methods in the atmospheric sciences.** 525 B Street, Suite 1900, San Diego, California. USA: Academic Press, 1995. 21–63,233–281 p. 43, 46, 73

WILLIAMS, E.; B., B.; A., M.; M., W.; S., H.; D., S.; S., G.; R., R.; D., B. The behavior of total lightning activity in severe florida thunderstorms. In: . [S.l.: s.n.], 1998. p. 01–34. Submitted to the Special Issue of Atmospheric Research in honor of Bernard Vonnegut. 13

WILLIAMS, E.; BOLDI, B.; MATLIN, A.; WEBER, M.; HODANISH, S.; SHARP, D.; GOODMAN, S.; RAGHAVAN, R.; BUECHLER, D. The behavior of total lightning activity in severe florida thunderstorms. **Atmospheric Research**, v. 51, n. 3, p. 245–265, 1999. ISSN 0169-8095. Available from: <<http://www.sciencedirect.com/science/article/pii/S0169809599000113>>. 13

WILLIAMS, E.; MATTOS, E.; MACHADO, L. Stroke multiplicity and horizontal scale of negative charge regions in thunderclouds. **Geophysical Research Letters**, 2016. 15, 16, 27, 30

WILSON, J. Thunderstorm nowcasting: past, present and future. In: **Preprints, 31st Conf. on Radar Meteorology, Seattle, WA, Amer. Meteor. Soc., J13–J19**. [S.l.: s.n.], 2003. 8

WILSON, J.; CROOK, N.; MUELLER, C.; SUN, J.; DIXON, M. Nowcasting thunderstorms: A status report. **Bulletin of the American Meteorological Society**, n. May, p. 2079–2099, 1998. 8

WILSON, J.; MUELLER, C. Nowcasts of thunderstorm initiation and evolution. **American Meteorological Society**, v. 8, p. 113–131, 1993. 8

WOLF, P. Anticipating the initiation, cessation, and frequency of cloud-to-ground lightning, utilizing wsr-88d reflectivity data. **NWA Electronic Journal of Operational Meteorology**, 2006. 3

WOODARD, C.; CAREY, L.; PETERSEN, W.; ROEDER, W. P. Operational utility of dual-polarization variables in lightning initiation forecasting. **Electronic J. Operational Meteor.**, v. 13, n. 6, p. 79–102, 2012. 3, 9

ZIPSER, E.; CECIL, D.; LIU, C.; NESBITT, S.; YORTY, D. Where are the most: Intense thunderstorms on Earth? **Bulletin of the American Meteorological Society**, v. 87, n. 8, p. 1057–1071, 2006. ISSN 00030007. 1, 16